Winter 12-3-2021

Novel Approaches for Enhancing Cell Survival and Function in Vivo

Ou Wang
University of Nebraska-Lincoln, wang.ou@huskers.unl.edu

NOVEL APPROACHES FOR ENHANCING CELL SURVIVAL AND FUNCTION IN VIVO

by

Ou Wang

A DISSERTATION

Presented to the Faculty of

The Graduate College at the University of Nebraska

In Partial Fulfillment of Requirements

For the degree of Doctor of Philosophy

Major: Engineering

(Biomedical Engineering)

Under the Supervision of Professors Yuguo Lei & William H. Velander

Lincoln, Nebraska

December 2021

NOVEL APPROACHES TO ENHANCE CELL SURVIVAL AND FUNCTION IN VIVO

Ou Wang, Ph.D.

University of Nebraska, 2021

Advisors: Yuguo Lei &William H. Velander

FDA has approved several cell-based therapeutics and hundreds of cell therapy clinical trials are ongoing. Cells will be a significant type of medicine after small molecule and protein drugs. However, several obstacles need to be addressed to achieve the widespread use of cellular therapeutics. The first challenge is the low efficacy of cell transplantation due to low retention, survival, integration, and function of cells *in vivo*. The second challenge is producing a massive number of cells for clinical treatment with cost-effectively and reproducibly technologies.

In this thesis, we proposed and investigated two approaches to address these challenges. To begin with, we engineered two novel biomaterials to deliver cells to enhance their *in vivo* retention and function. The first biomaterial is a recombinant fibrin matrix which significantly improved cell delivery efficiency and safety. The second biomaterial is a novel γγ'F1:pFN complex fibrin matrix, which enhanced cell culture and improved wound healing. In the second approach, we engineered injectable, microscale, 3D tissues to address the challenges. Brown adipose microtissues were prepared and injected to alleviate obesity and associated type 2 diabetes mellitus(T2DM). In addition, we showed a novel, scalable and cell-friendly cell culture technology (AlgTubes) for scalable

microtissue manufacturing. Animal cells were used for preliminary study and can be used for food science to produce cultured meat. This technology has the potential to produce any cell therapy-related cell types in the future. Finally, we also systematically proposed engineering a physiologically relevant microenvironment for large-scale therapeutic cell and microtissue production.

DEDICATION

I dedicate my work to my beloved family members, my husband, my daughter, my parents, and my parents-in-law for their unconditional love and support along the way.

ACKNOWLEDGEMENTS

I would like to express my sincere gratitude towards my advisor, Dr. Yuguo Lei, for his patient guidance and useful critiques. His advice guided me through all the stages of my Ph.D. study. He not only taught me scientific experiments but also gave me a lot of valuable suggestions in career development.

I would also like to thank my advisor Dr. Velander for his assistance and advice during my Ph.D. His expert suggestions guided me in the area of biomaterial and biochemistry. He always assists and encourages me when I have difficulties.

I would like to thank my committee members, Dr. Srivatsan Kidambi and Dr. Ruizhi Zhang, for their helpful comments and suggestions on my dissertation.

I would like to thank my lab members, Dr. Haishuang Lin, Dr. Qiang Li, Dr. Li Han, and Jack Rauch, for their generous assistant and support.

I would also express my appreciation to all the faculty and staff in Chemical and Biomolecular Engineering. I appreciate Leonard Akert for making all the devices and helping repair everything in our lab. I would like to thank Nicole Church, Raquel O'Grady, and Ethan Kreifels for ordering items and helping me solve problems.

Finally, I would like to give my special thanks to my beloved family members. Thanks to my husband, Shuyang Zhang, for his continuous encouragement and emotional support during my life. He is always there by my side. His encouragement and care supported me overcome the challenging and stressful time over these years. Thank my

daughter Mumu, my parents, and my parents-in-law for their support and bringing enjoyable and treasurable moments for my Ph.D. study.

DESSERTATION DECLARATION

Chapter 2 was published in *Journal of Biomedical Materials Research Part A*. (Wang, O., Ismail, A., Fabian, F.M., Lin, H., Li, Q., Elowsky, C., Carlson, M.A., Burgess, W., Velander, W.H., Kidambi, S. and Lei, Y., 2018. A totally recombinant fibrin matrix for mesenchymal stem cell culture and delivery. Journal of Biomedical Materials Research Part A, 106(12), pp.3135-3142.).

Some of the content discussed in Chapter 3 was published in *Bioactive Materials*. (Jara, C.P., Wang, O., do Prado, T.P., Ismail, A., Fabian, F.M., Li, H., Velloso, L.A., Carlson, M.A., Burgess, W., Lei, Y. and Velander, W.H., 2020. Novel fibrin-fibronectin matrix accelerates mice skin wound healing. *Bioactive Materials*, 5(4), pp.949-962.)

Chapter 6 was published in *Cell & Gene Therapy insights*. (Wang, O. and Lei, Y. 2019. Creating a cell-friendly microenvironment to enhance cell culture efficiency. *Cell and Gene Therapy Insights*, 5(3), pp. 341–350.)

Table of Contents

LIST OF FIGURES

LIST OF TABLES

CHAPTER 1. INTRODUCTION

Overview

FDA has approved several cell-based therapeutics and hundreds of cell therapy clinical trials are on-going[1–4]. The clinical outcome for treating many diseases are exciting[5–8]. There is no doubt that cells will be a significant type of medicine after small molecule and protein drugs[9]. However, several obstacles need to be addressed to achieve the widespread use of cellular therapeutics [4,10]. **The first challenge** is the low retention, survival, integration, and function of cells *in vivo* following transplantation. For instance, only ~6% of transplanted dopaminergic (DA) neurons and ~1% of injected cardiomyocytes survived in rodent models several months after transplantation[11,12]. Only a portion of cells stays at the injection or lesion site. The lesion sites, which typically contain a high concentration of inflammatory cells and factors and a low concentration of O_2, nutrients, and growth factors due to the absence of vascular structures, are very hostile to the transplanted cells. The disruption of cell signaling, cell-cell, and cell-matrix interactions during cell preparation[13] before transplantation (termed anoikis) and acute cell apoptosis during the injection[14] also contribute to the low survival rate.

The second challenge is to produce a large number of cells[15]. For example, ~10^5 surviving DA neurons, ~10^9 cardiomyocytes, or ~10^9 β-cells are required to treat a patient with Parkinson's disease (PD), myocardial infarction (MI), or type I diabetes, respectively[15]. Likewise, ~10^{10} hepatocytes or cardiomyocytes would be required for an artificial human liver or heart, respectively[16]; a similar number of cells are needed to screen

a library of a million compounds at once[17,18]. Considering the low survival of transplanted cells *in vivo*, the large patient populations with degenerative diseases (over 1 million people with PD, 1-2.5 million with type I diabetes, and ~8 million with MI in the US alone[19]), a massive number of cells are needed.

In this thesis, we proposed and investigated two approaches to address these challenges. **The first approach** used novel biomaterials to deliver cells to enhance their *in vivo* retention and function. Research has shown that a biomaterial scaffold can significantly improve the retention of cells, maintain high viability, keep cell phenotype and provide cells a 3D microenvironment to grow and interact[10,20]. In this thesis, we investigated two novel biomaterials for cell delivery and disease treatment. The first biomaterial is a recombinant fibrin matrix which significantly improved cell delivery efficiency and safety. The results are presented in chapter 2. The second biomaterial is a novel γγ'F1:pFN complex fibrin matrix, which enhanced cell culture and improved wound healing. The results are shown in chapter 3.

The second approach to address the challenges is using injectable, microscale, 3D tissues. Microtissues contain not only cells but also their native ECMs, cell-cell contacts, cell-matrix interactions, 3D and vascular structures that can prevent cells from anoikis and acute apoptosis during the transplantation[21], promoting cell survival, integration, maturation, and function *in vivo*[22,23]. Besides these advantages over stem cells, microtissues also have advantages over large tissues made via the conventional tissue engineering approaches. They are injectable, so open surgery is not required for the transplantation, which is extremely important for treating diseases in organs with sophisticated structures (e.g., the brain). In addition, they can be produced on a large scale

via GMP compliant bioreactors, giving them the potential for treating large populations of patients. In chapter 4, we prepared and showed that brown adipose microtissues could alleviate obesity and its associated type 2 diabetes mellitus(T2DM). In chapter 5, a novel, scalable and cell-friendly technology (AlgTubes) anchored with RGD for microtissue manufacturing was developed. Animal cells were used for preliminary study and can be used for food science to produce cultured meat. This technology has the potential to produce any cell therapy-related cell types in the future. In the last chapter (chapter 6), we systematically proposed engineering a physiologically relevant microenvironment for large-scale therapeutic cell and microtissue production.

Summaries of Chapters

Chapter 2: A recombinant fibrin matrix made with recombinant human fibrinogen, recombinant human thrombin, and recombinant human factor XIII was used to culture and deliver mesenchymal stem cells (MSCs). The fibrin matrix could significantly enhance the retention of the delivered hMSCs. These recombinant proteins considerably reduce the cost and risk of human pathogen transmission compared to the current plasma-derived fibrin matrix.

Chapter 3: We synthesized a novel fibrin matrix exclusively from a 1:1 (molar ratio) complex of γγ'F1 and pFN in the presence of highly active thrombin and recombinant Factor XIII (rFXIIIa). In this matrix, the fibrin nanofibers were decorated with pFN nanoclusters (termed γγ'F1:pFN fibrin). The γγ'F1:pFN fibrin enhanced the adhesion and proliferation of primary human umbilical vein endothelium cells (HUVECs). HUVECs in

the 3D γγ'F1:pFN fibrin exhibited a starkly enhanced vascular morphogenesis. Mouse dermal wounds sealed by γγ'F1:pFN fibrin showed accelerated and improved healing, suggesting that a 3D pFN presentation on a fibrin matrix promotes wound healing.

Chapter 4: We Engineered 3D brown adipose microtissues as anti-obesity (OB)/type 2 diabetes (T2DM) therapeutics. They have considerable advantages over dissociated brown adipocytes (BAs) for future clinical applications in product scalability, storage, purity, quality, and in vivo safety, dosage, survival, integration, and efficacy. 3D BA microtissues could be fabricated at large scales, cryopreserved for the long term, and delivered via injection. BAs in the microtissues had higher purity and higher UCP-1 protein expression than BAs prepared via 2D culture. In addition, 3D BA microtissues had good in vivo survival and tissue integration and had no uncontrolled tissue overgrowth. Furthermore, they showed good efficacy in preventing OB and T2DM with a very low dosage compared to literature studies.

Chapter 5: We engineered an alginate hydrogel tube cell culture system to provide adhesion for large-scale microtissue fabrication. We showed both mouse and quail myoblasts could be efficiently expanded and differentiated in the system. The yields were between 1x to $2x10^8$ cells/mL hydrogel tubes. Myotubes were aligned along the hydrogel tubes. When the hydrogel shell is dissolved with EDTA, these cell micro-fibers could be used as building blocks to fabricate large volume meat.

Chapter 6: Cells will be a significant type of medicine. To achieve the full potential of cellular therapeutics, we must be able to cost-effectively and reproducibly manufacture

cells at large scales and with high quality. Currently, the robust and cost-effective culture of high-quality allogeneic or autologous cells on large scales is still very challenging. Academia and industry focus on developing modular, disposable, and closed bioreactors, automating the cell culture, integrating process analysis and control, and artificial intelligence. We propose that the cell culture microenvironment impacts the cell culture outcome and the critical need of creating a cell-friendly microenvironment during cell manufacturing.

Future Research:

Based on the technologies and results from this dissertation, the following research questions/topics can be conducted in the future:

1) The long-term effect of the recombinant fibrin matrix on cell survival, integration, and function should be investigated. It will also be valuable to use clinic-relevant disease models such as myocardial infarction and stroke to test the capability of the matrix to retain the cells at the injection sites. The system should also be tested on other therapeutic cell types such as stem cell-derived cardiomyocytes and neurons.

2) Novel γγ'F1:pFN complex should be tested to deliver cells and proteins. Can it improve cell retention and survival in vivo? And is it better than the recombinant fibrin matrix considering its sophistic nanostructure?

3) Can we incorporate endothelial cells to make vascularized BA microtissues? Can we use human pluripotent stem cells as the source to make BA microtissue?

4) Can we produce the BA microtissue at a large scale using the AlgTube cell culture system?

References

1. Schwartz, S. D. *et al.* Embryonic stem cell trials for macular degeneration: A preliminary report. *Lancet* **379**, (2012).

2. Trounson, A. & McDonald, C. Stem Cell Therapies in Clinical Trials: Progress and Challenges. *Cell Stem Cell* vol. 17 (2015).

3. Mandai, M. *et al.* Autologous Induced Stem-Cell–Derived Retinal Cells for Macular Degeneration. *N. Engl. J. Med.* **376**, 1038–1046 (2017).

4. Mount, N. M., Ward, S. J., Kefalas, P. & Hyllner, J. Cell-based therapy technology classifications and translational challenges. *Philosophical Transactions of the Royal Society B: Biological Sciences* vol. 370 (2015).

5. Huang, H. *et al.* Clinical Cell Therapy Guidelines for Neurorestoration (IANR/CANR 2017). *Cell Transplant.* **27**, (2018).

6. Fisher, S. A., Doree, C., Mathur, A., Taggart, D. P. & Martin-Rendon, E. Stem cell therapy for chronic ischaemic heart disease and congestive heart failure. *Cochrane Database of Systematic Reviews* vol. 2016 (2016).

7. Fernández-Ruiz, I. Stem cells: Cell therapy improves outcomes in heart failure. *Nature Reviews Cardiology* vol. 13 (2016).

8. Wei, X. *et al.* Mesenchymal stem cells: A new trend for cell therapy. *Acta Pharmacologica Sinica* vol. 34 (2013).

9. Fischbach, M. A., Bluestone, J. A. & Lim, W. A. Cell-based therapeutics: The next pillar of medicine. *Science Translational Medicine* vol. 5 (2013).

10. Tong, Z. *et al.* Application of biomaterials to advance induced pluripotent stem cell research and therapy. *EMBO J.* **34**, 987–1008 (2015).

11. Kriks, S. *et al.* Dopamine neurons derived from human ES cells efficiently engraft in animal models of Parkinson's disease. *Nature* **480**, 547–51 (2011).

12. Laflamme, M. a & Murry, C. E. Regenerating the heart. *Nat. Biotechnol.* **23**, 845–56 (2005).

13. Grossmann, J. Molecular mechanisms of 'detachment-induced apoptosis--Anoikis'. *Apoptosis* **7**, 247–60 (2002).

14. Aguado, B. A. *et al.* Improving Viability of Stem Cells During Syringe Needle Flow Through the Design of Hydrogel Cell Carriers. *Tissue Eng Part A* **18**, 806–815 (2012).

15. Serra, M., Brito, C., Correia, C. & Alves, P. M. Process engineering of human pluripotent stem cells for clinical application. *Trends Biotechnol.* **30**, 350–358 (2012).

16. Badylak, S. F., Taylor, D. & Uygun, K. Whole-organ tissue engineering: decellularization and recellularization of three-dimensional matrix scaffolds. *Annu. Rev. Biomed. Eng.* **13**, 27–53 (2011).

17. McNeish, J. Embryonic stem cells in drug discovery. *Nat. Rev. Drug Discov.* **3**,

70–80 (2004).

18. Desbordes, S. C. & Studer, L. Adapting human pluripotent stem cells to high-throughput and high-content screening. *Nat. Protoc.* **8**, 111–130 (2012).

19. Roger, V. L. *et al.* Heart disease and stroke statistics--2012 update: a report from the American Heart Association. *Circulation* **125**, e2–e220 (2012).

20. Hassan, W., Dong, Y. & Wang, W. Encapsulation and 3D culture of human adipose-derived stem cells in an in-situ crosslinked hybrid hydrogel composed of PEG-based hyperbranched copolymer and hyaluronic acid. *Stem Cell Res. Ther.* **4**, 32 (2013).

21. Takebe, T. *et al.* Vascularized and functional human liver from an iPSC-derived organ bud transplant. *Nature* **499**, 481–484 (2013).

22. Woodford, C. & Zandstra, P. W. Tissue engineering 2.0: guiding self-organization during pluripotent stem cell differentiation. *Curr. Opin. Biotechnol.* **23**, 810–9 (2012).

23. Sasai, Y. Perspective Next-Generation Regenerative Medicine : Organogenesis from Stem Cells in 3D Culture. *Stem Cell* **12**, 520–530 (2013).

CHAPTER 2. A TOTALLY RECOMBINANT FIBRIN MATRIX FOR MESENCHYMAL STEM CELL CULTURE AND DELIVERY

Introduction

Human mesenchymal stem cells (MSCs) can be differentiated into a variety of cells[1–3] such as myoblasts[4], osteoblasts[5,6], chondroblasts[7], and adipocytes[8]. They also secrete a panel of factors that can modulate many biological processes including inflammation and angiogenesis[9]. Consequently, they have been widely studied for engineering tissues[10,11] and treating diseases both in laboratories[12,13], clinical trials[14,15], and clinics[16,17] with encouraging results. For instance, transplanting MSCs enhanced bone tissue repair[18,19], promoted angiogenesis in the myocardial ischemic area[20,21], improved cardiac performance after myocardial infarction[16,20,22], and reduced inflammation and improved brain functions in a variety of neurological diseases[23–25].

A significant challenge with using MSCs to treat diseases is that only a small numbers of the systematically injected cells can home to the diseased sites[21,26,27]. A solution to this challenge is to locally inject cells to the diseased sites. However, the percentage of the injected cells that can stay at the injection site is still low. Researches have shown injecting the cells with a biomaterial matrix can significantly enhance the retention of cells at the injection site[28–31]. Both natural and synthetic biomaterial such as collagen, hyaluronic acid, and polyethylene glycol hydrogels have been investigated for this purpose[28–31]. Among the many biomaterials, fibrin is of particular interest due to its biocompatibility and biodegradation[32–34]. In addition, it has been used in the clinic as a

hemostatic material for a long time[35]. Fibrinogen (FI) is a linear, hexameric, 340 kDa glycoprotein having 2 alpha, 2 beta and 2 gamma chains. Activated thrombin (FIIa) rapidly polymerizes fibrinogen to form an insoluble hydrogel that is held together by electrostatic and other noncovalent forces. Activated factor XIII (FXIIIa) can further crosslink this hydrogel matrix using covalent bonds to make it more stable[36]. Fibrin matrices have been widely used for culturing[37,38] and delivering MSCs[34,39].

The currently used fibrinogen is purified from human plasma. The shortcomings of plasma derived fibrinogen include the high cost and potential of human pathogen transmission[40,41]. To address the problem, we previously made transgenic cows to produce recombinant human fibrinogen (rFI) in milk[42]. We have shown recombinant human fibrinogen and plasma fibrinogen have comparable clotting speed, strength and function in a swine liver trauma model[43]. In these studies, we also used activated recombinant human factor XIII (rFXIIIa) and recombinant human thrombin (rFII) to polymerize the fibrinogen, resulting in fibrin matrices made with entirely recombinant proteins[43]. These recombinant proteins significantly reduce the cost and risk of human pathogen transmission. In this study, we aim to explore if these totally recombinant fibrin matrices can be used to culture and deliver MSCs. We first systematically studied the relationship between the matrix formulation, the nanostructure and the behaviors of cells in the matrix. We then used an optimized matrix to deliver MSCs to NOD-SCID mice. We found the matrix could significantly enhance the retention of the delivered hMSCs.

Materials and methods

Materials

Recombinant fibrinogen (rFI) was produced, characterized and purified as previously described[42,43]. Briefly, the DNA sequences of human α, β, γ chains of fibrinogen were inserted into the cow genome by the method of nuclear transfer. The fibrinogen was produced in the milk of transgenic cows and purified through multiple precipitations and chromatography[42,43]. Activated recombinant human factor XIII (rFXIIIa) was produced in *Pichia pastoris* using published protocols[42,44]. Recombinant human thrombin (rFIIa) was purchased from ZymoGenetics (Seattle, WA).

Cell culture

Mouse bone marrow mesenchymal stem cells (D1 cells, CRL12424) were purchased from ATCC and cultured in DMEM supplemented with 10% fetal bovine serum and 1% penicillin/streptomycin at 37 °C and 5% CO_2. Primary human bone marrow mesenchymal stem cells were purchased from Lonza and culture in MesenCult™ MSC Basal Medium (Human) supplemented with MesenCult™ MSC Stimulatory Supplement (Human) and 1% penicillin/streptomycin. Cells were passaged every 5 days with 0.25% trypsin.

Fibrin matrix preparation

Recombinant fibrin matrices were prepared in Ringer's solution (155 mM NaCl, 5 mM KCl, 2 mM $CaCl_2$ and 1 mM $MgCl_2$, pH=7.4) with different final concentrations of

rFI, rFXIIIa, and rFII as described in the text. The protein mixtures were incubated at 37 °C for 15 minutes in a cell culture incubator to form the fibrin matrices.

3D cell culture

100 µl fibrin matrix with 3 x 10^4 cells was made in one well of the 96-well plate. 200 µl cell culture medium was added on the top of the fibrin matrix in each well. At various time points, cell morphologies were imaged with the phase-contrast microscope. On day 2 and 4, the medium was removed and 100 µl fresh medium and 10 µl Alamar blue reagent were added and incubated for 3 hours. 100 µl medium from each well was collected to measure the fluorescence, which was calibrated to a standard curve to calculate the numbers of live cells within each well. The viability of cells within the gel was assessed with Live/Dead cell assay kit (Invitrogen) according to the Manufacturer's instruction.

Scanning Electron Microscopy (SEM)

Fibrin matrices were fixed with 2.5% glutaraldehyde in 100 mM phosphate buffer (PH 7.0) at room temperature for 1 hour. Samples were rinsed with phosphate buffer twice with 10 minutes each. Matrices were sequentially dehydrated using 30%, 50%, 70%, 95% (twice), 100% (twice) ethanol with 5 minutes for each treatment. Samples were then sequentially treated using 33%, 66%, 100% (twice) hexamethyldisilane with 2 minutes for each treatment. Samples were air-dried overnight before sputter-coated with gold-palladium and imaged with a scanning electron microscope (Hitachi S4700 Field-Emission SEM, Hitachi, Tokyo, Japan).

Animal experiment

The animal protocol was approved by the Institutional Animal Care and Use Committee of the University of Nebraska-Lincoln. The experimental procedure was performed in accordance with the guidelines of the Institutional Animal Care and Use Committee of the University of Nebraska-Lincoln. Human MSCs were stained with Vybrant DiI dye (V-22885, Molecular probe), and injected subcutaneously to the back of the neck of NOD-SCID mice (Charles River Laboratory). 6 mice were used for the study. For each mouse, 8 x 10^5 cells in 200 μl Ringer's solution were injected to the left side of the neck, and 8 x 10^5 cells with a fibrin matrix were injected to the right side of the neck using a Tisseel-Duploject dual-syringe. Within the Tisseel-Duploject dual-syringe, one syringe had 100 μl Ringer's solution contained 10 mg/ml rFI and 4 x 10^5 MSCs, the other syringe had 100 μl Ringer's solution contained 0.16 mg/ml rFXIIIa, 20 U/ml rFIIa, and 10 mM $CaCl_2$. The injected site was marked. After 24 hours, mice were euthanized. The skin and connective tissue at and surrounding the injected site were harvested for analysis. The harvested tissues were fixed with 4% PFA followed by soaking in 30% sucrose for 4 days. Tissues were embedded in OCT and cryosectioned (vertical to the skin surface) with 40 μm thickness for each section. Tissue sections were imaged with a Zeiss Axio Observer fluorescent microscopy. The total fluorescence intensity in the section that crosses the needle track was quantified with Image J. software and used to evaluate the retention of the injected MSCs at the injection site in each mouse.

Statistical analyses

The data are presented as the mean ± S.D.. We used an unpaired t-test to compare two groups and one-way ANOVA to compare more than two groups (GraphPad Software, La Jolla, CA). $P < 0.05$ was considered statistically significant.

Results

Using mouse mesenchymal stem cells (D1 cells) to study the matrix composition-matrix structure-cell behavior relationship

Effect of recombinant the thrombin (rFIIa) concentration

To study the effect of rFIIa concentration, the recombinant fibrinogen (rFI) and activated recombinant factor thirteen (rFXIIIa) was fixed at 5 mg/ml and 0.04 mg/ml respectively. The rFIIa concentration was varied from 1 U/ml to 15 U/ml (**Figure 2.1**). Scanning electron microscope (SEM) images showed the fibrin fiber diameter, fiber branching, fiber density and matrix pore size were similar between matrices made with different rFIIa concentrations (**Figure 2.1A**). Cells exhibited a characteristic, spindle-like morphology in all matrices after 2 days (**Figure 2.1B**). Live and dead staining on day 1 showed no obvious cell death in all matrices (**Figure 2.1C**). The total numbers of live cells in the four matrices were similar on day 2 and day 4 (**Figure 2.1D**). These results showed that the rFIIa concentration at the tested range had no significant influence on the matrix structure and cell behaviors including cell morphology, viability, and the final live cell numbers.

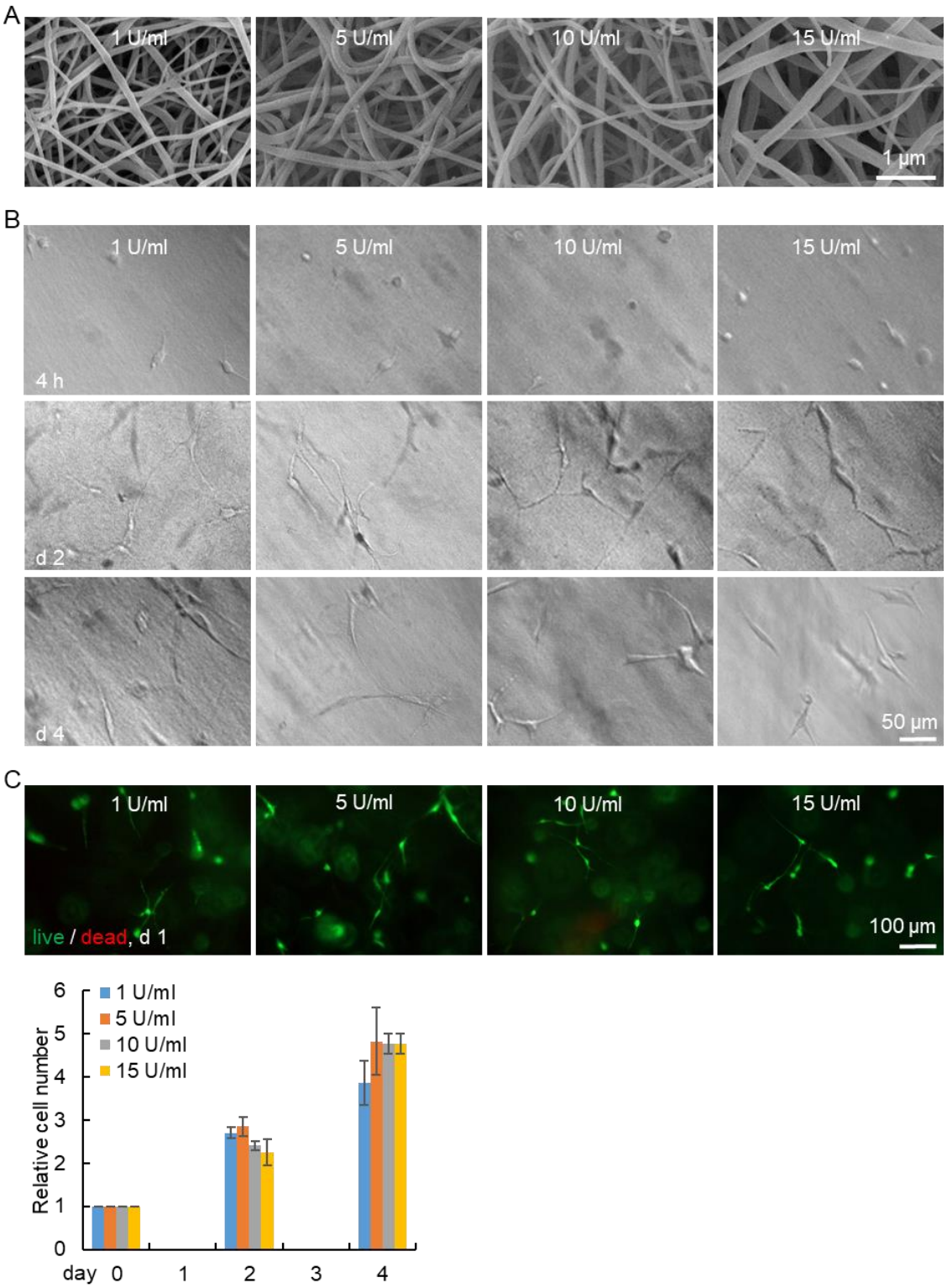

Figure 2.1. Culturing D1 cells in 3D recombinant fibrin matrices made with different recothrombin (rFIIa) concentrations (1 U/ml, 5 U/ml, 10 U/ml, 15 U/ml). Recombinant fibrinogen (rFI) = 5 mg/ml; recombinant factor thirteen (rFXIIIa) = 0.04 mg/ml; (A) Scanning electron microscope (SEM) images; (B) Phase images at 4 h, day 2 and day 4; (C) Live dead cell staining of day 1 cells; (D) Cells in 100 µl fibrin matrix on day 2 and day 4 were quantified by alamar blue assay. Cell numbers were related to initial seeded cells.

Effect of the rFXIIIa concentration

FXIIIa covalently crosslinks the fibrin matrix and enhances the stability of the matrix. The yeast-produced activated recombinant FXIIIa has dimeric catalytic subunits and has been under clinical studies[45]. To assess the effect of the rFXIIIa concentration, the rFI and rFIIa was fixed at 5 mg/ml and 10 U/ml respectively. The rFXIIIa concentration was varied from 0 mg/ml to 0.15 mg/ml (**Figure 2.2**). SEM images showed the fibrin fiber diameter, fiber branching, fiber density and matrix pore size were very similar between matrices made with different rFXIIIa concentrations (**Figure 2.2A**). Cells showed spindle-like morphology in all samples on day 2. However, the fibrin matrix without rFXIIIa had significant degradation and shrank on day 4 (**Figure 2.2B**). Live and dead staining on day 1 did not detect evident cell death in all samples (**Figure 2.2C**). The alamar blue assay showed a significantly higher cell number in the matrix without rFXIIIa on day 4, but there was no significant difference between the other 3 matrices (**Figure 2.2D**). In summary, rFXIIIa was required to form a fibrin matrix that could last 4 days in the presence of MSCs. However, its concentration at the range from 0.04 mg/ml to 0.15 mg/ml had no significant influence on the matrix structure and cell behaviors.

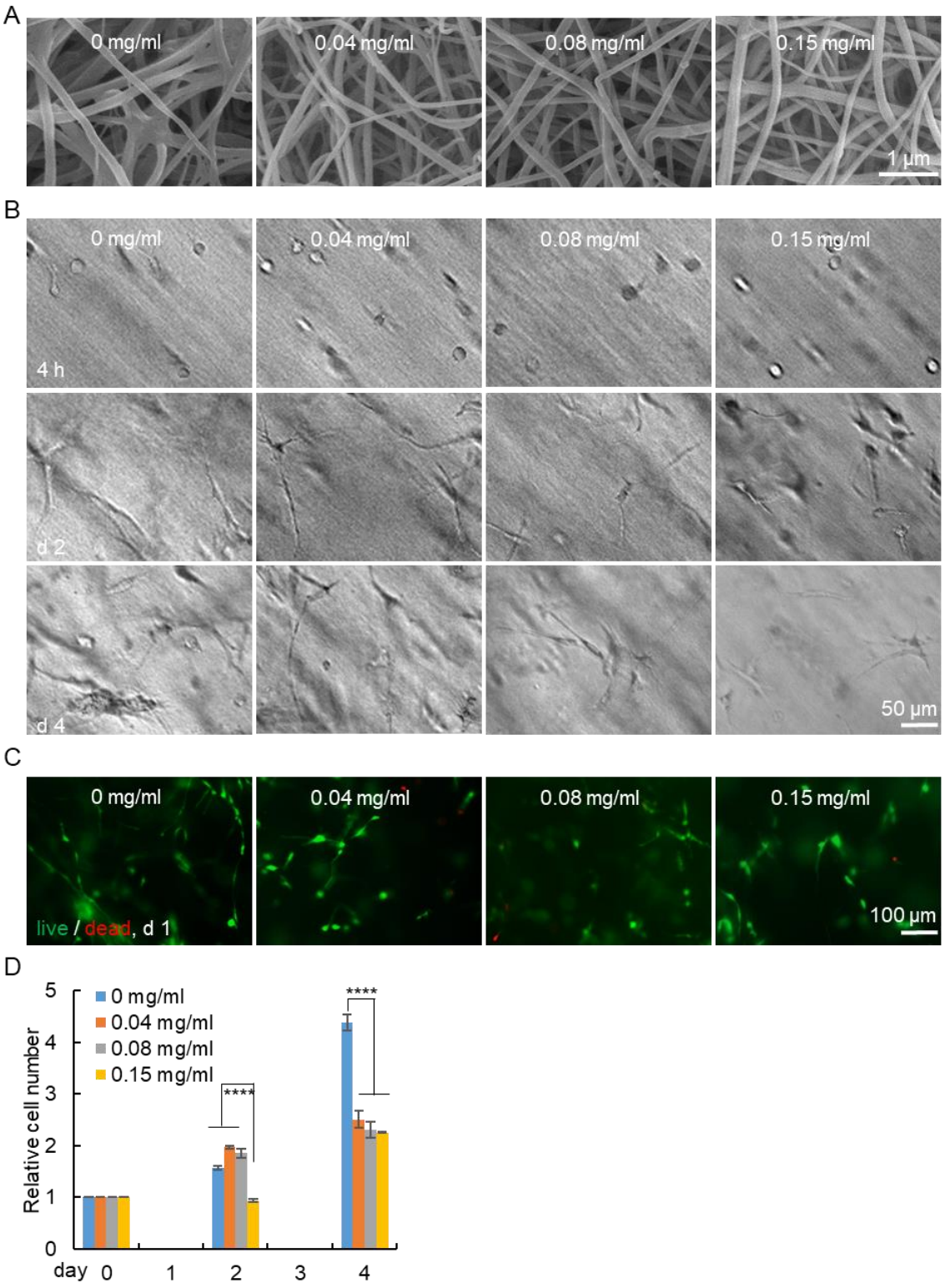

Figure 2.2. Culturing D1 cells in fibrin matrices made with different recombinant factor thirteen (rFXIIIa) concentrations (0 mg/ml, 0.04 mg/ml, 0.08 mg/ml, 0.15 mg/ml). rFI = 5 mg/ml, rFIIa = 10 U/ml. (A) SEM images; (B) Phase images at 4 h, day 2 and day 4; (C) Live/dead cell staining of day 1 cells; (D) Cells in 100 µl fibrin matrix on day 2 and day 4 were quantified by alamar blue assay. Cell numbers were related to initial seeded cells. ****: $p<0.0001$.

Effect of the rFI concentration

To study the effect of the rFI concentration, the rFIIa and rFXIIIa was fixed at 10 U/ml and 0.08 mg/ml respectively. The rFI concentration was varied from 5 mg/ml to 20 mg/ml (**Figure 2.3**). The SEM revealed that the fibrin matrix with higher rFI concentration had more condensed and larger (in diameter) fibers (**Figure 2.3A**). Cells had spindle-like morphology only in the fibrin matrix with 5 mg/ml rFI. Cells had round morphology in fibrin matrices with 10, 15 and 20 mg/ml rFI (**Figure 2.3B**). Significant cell deaths were observed in matrices with 10, 15 and 20 mg/ml rFI using live and dead staining on day 1 (**Figure 2.3C**). During the 4 day culture, the cell number increased in the matrix made with 5 mg/ml rFI, while they decreased in other groups, especially in matrices with 15 and 20 mg/ml rFI (**Figure 2.3D**). These results showed that, unlike rFIIa and rFXIIIa, the concentration of rFI had a significant effect on the matrix structure, cell morphology, survival and/or growth.

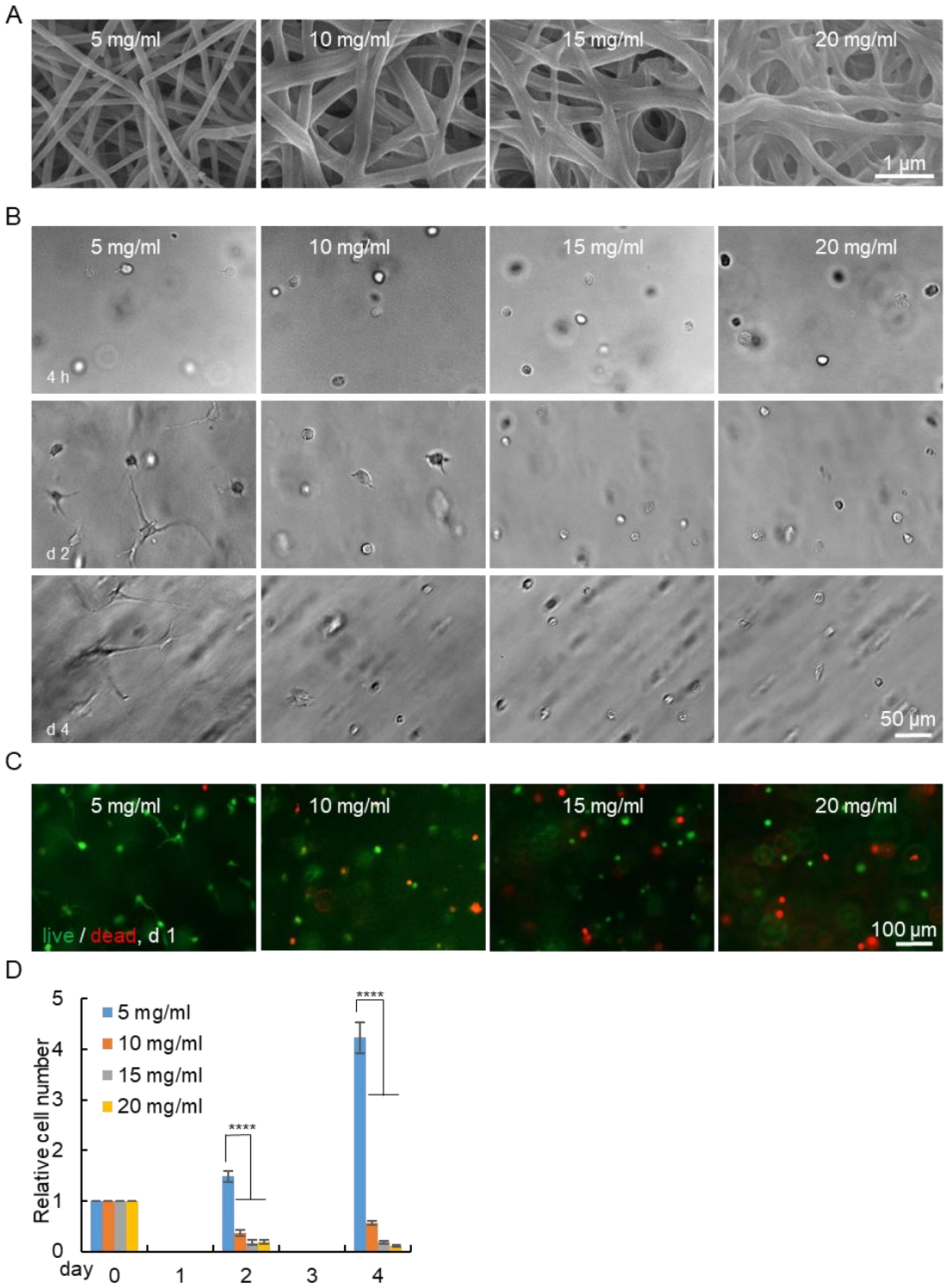

Figure 2.3. Culturing D1 cells in fibrin matrices made with different recombinant fibrinogen (rFI) concentrations (5 mg/ml, 10 mg/ml, 15 mg/ml, 20 mg/ml). rFIIa = 10 U/ml, rFXIIIa = 0.08 mg/ml. (A) SEM images; (B) Phase images at 4 h, day 2 and day 4; (C) Live dead cell staining of day 1 cells; (D) Cells in 100 µl fibrin matrix on day 2 and day 4 were quantified by alamar blue assay. Cell numbers were related to initial seeded cells. ****: $p<0.0001$.

Validate the findings with human MSCs (hMSCs)

To study if the above findings with mouse MSCs can be translated to hMSCs, we selected 5 representative formulations for culturing human bone marrow MSCs (**Figure 4**). In the matrix made with 5 mg/ml rFI, 0.08 mg/ml rFXIIIa and 10 U/ml rFIIa, (labeled as (5, 0.08, 10) or the control group), hMSCs had spindle-like morphology after 2 days and no significant cell death was observed by live and dead staining (**Figure 2.4A and 2.4B**). When the rFI concentration was increased to 10 mg/ml (labeled as (10, 0.08, 10)), cells showed no spreading even after 4 days. The Live and dead staining detected significant dead cells (**Figure 2.4A and 2.4B**). There was significantly less cells in this matrix on both day 2 and 4 (**Figure 2.4C**). When the rFIIa concentration was decreased to 5 U/ml (5, 0.08, 5), the cell morphology, viability and numbers were very similar to these of the control group. There was much more cells in the matrix without rFXIIIa (5, 0, 10) than other groups. We observed significant matrix degradation for this condition on day 1 (**Figure 2.4D**). hMSCs in the matrix made with 0.15 mg/ml rFXIIIa (5, 0.15, 10) were very similar to cells in the control matrix. In short, the recombinant fibrin matrix compositions had similar effects on mouse and human mesenchymal stem cells. Fibrin matrices made with rFI higher than 5 mg/ml were inappropriate for hMSC culture.

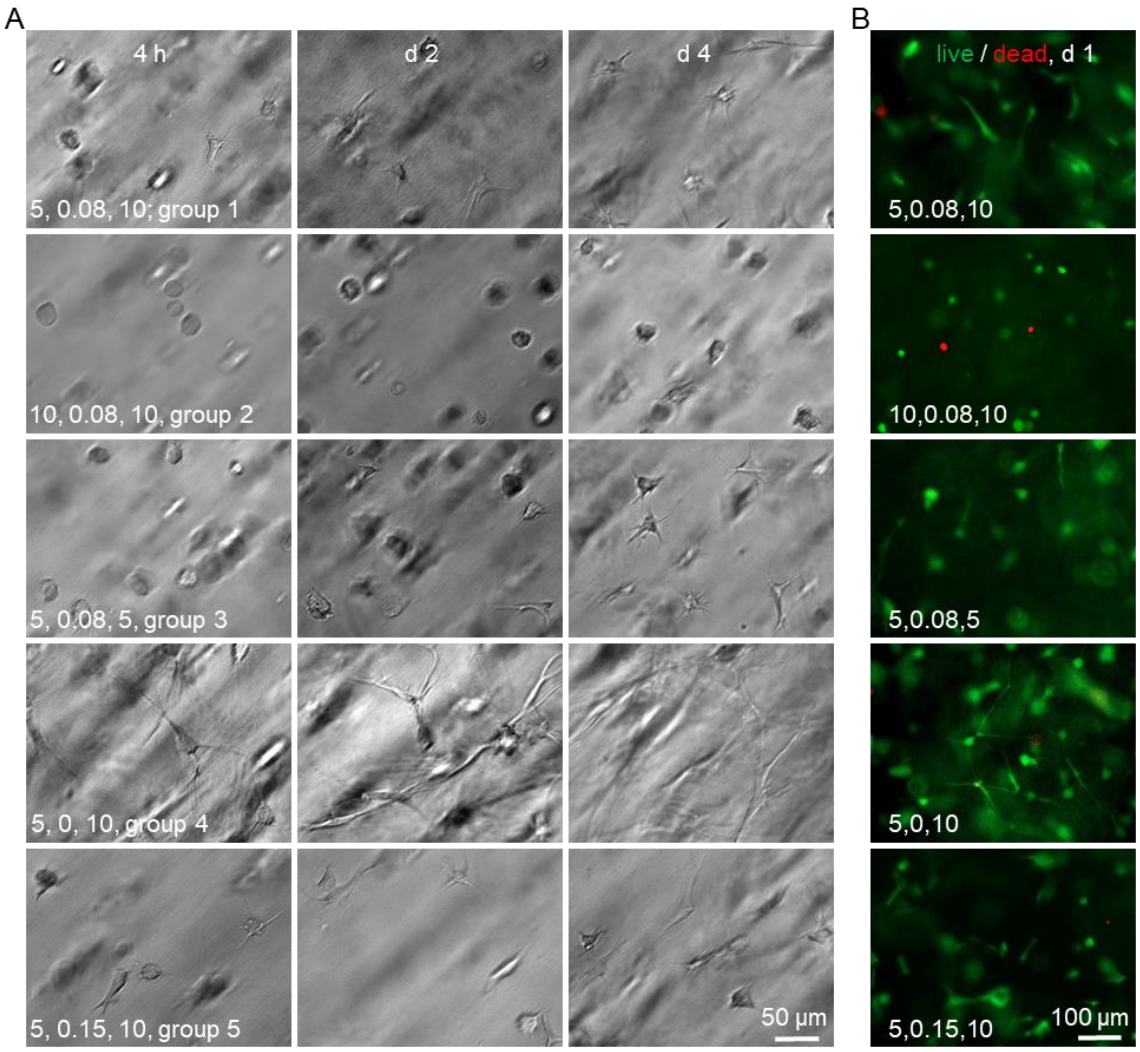
A
4 h
d 2
d 4
5, 0.08, 10; group 1
10, 0.08, 10, group 2
5, 0.08, 5, group 3
5, 0, 10, group 4
5, 0.15, 10, group 5
50 µm
B
live / dead, d 1
5,0.08,10
10,0.08,10
5,0.08,5
5,0,10
5,0.15,10
100 µm
C
Relative cell number
day
5,0.08,10
10,0.08,10
5,0.08,5
5,0,10
5,0.15,10
****
***
*
D
5, 0, 10, group 4
200 µm

Figure 2.4. Culturing human MSC cells in fibrin matrices made with different rFI, rFXIIIa, and rFIIa concentrations. Group 1: rFI = 5 mg/ml, rFXIIIa = 0.08 mg/ml, rFIIa = 10 U/ml; Group 2: rFI = 10 mg/ml, rFXIIIa = 0.08 mg/ml, rFIIa = 10 U/ml; Group 3: rFI = 5 mg/ml, rFXIIIa = 0.08 mg/ml, rFIIa = 5 U/ml; Group 4: rFI = 5 mg/ml, rFXIIIa = 0 mg/ml, rFIIa = 10 U/ml; Group 5: rFI = 5 mg/ml, rFXIIIa = 0.15 mg/ml, rFIIa = 10 U/ml. (A) Phase images at 4 h, day 2 and day 4; (B) Live/ dead cell staining of day 1 cells; (C) Cells in 100 µl fibrin matrix on day 2 and day 4 were quantified by alamar blue assay. Cell numbers were related to initial seeded cells; (D) The fibrin matrix without rFXIII had significant degradation on day 1. The white cycles indicate areas with significant degradation. ****: $p<0.0001$, ***: $p<0.001$, *: $p<0.05$.

Deliver hMSCs with fibrin matrix

Lastly, we studied if the recombinant matrix could be used to deliver hMSCs and enhanced their retention at the injection site. The fibrin matrix with 5 mg/ml rFI, 0.08 mg/ml rFXIIIa and 10 U/ml rFIIa was used because the *in vitro* cell culture experiment found it was stable for at least 4 days, supported high cell viability and reasonable cell growth (**Figure 2.4C**). hMSCs were labeled with fluorescent Dil dyes and injected subcutaneously to NOD-SCID mice. Using the fibrin matrix, significantly higher numbers (two-fold) of cells were retained at the injection site (**Figure 2.5**).

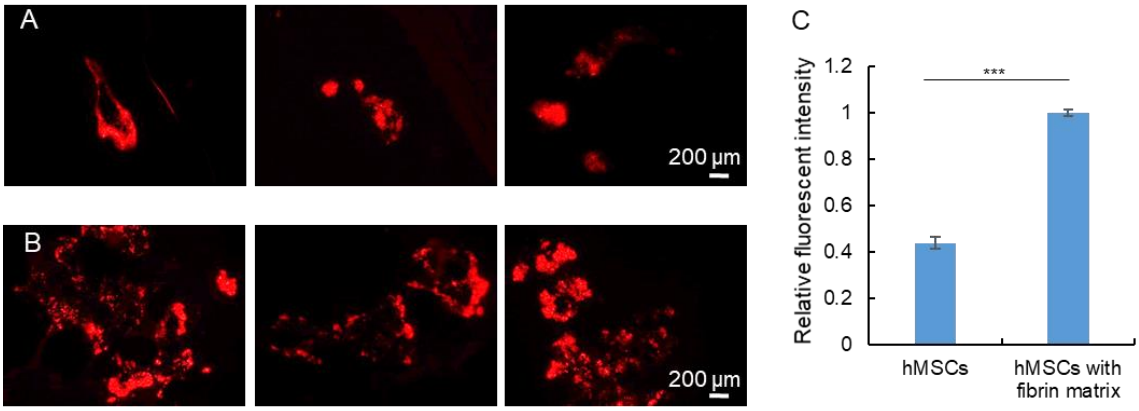

Figure 2.5. Deliver hMSCs with recombinant fibrin matrices. hMSCs were labeled with Dil dyes and injected subcutaneously into NOD-SCID mice without (A) and with the fibrin matrix (B) (rFI = 5 mg/ml, rFXIIIa = 0.08 mg/ml, rFIIa = 10 U/ml). Representative fluorescent images of the labeled MSCs at the injection sites from three mice were shown. (C) The relative fluorescent intensities at the injection sites of the two transplantation groups. 6 mice were used for the analysis. ***: $p<0.001$.

Conclusion

Recombinant fibrin matrices, which have lower cost and risk of the human pathogen transmission, are very attractive for MSCs culture and delivery[42,43]. For the first time, our studies found fibrin matrices made with entirely recombinant proteins were suitable for culturing and delivering MSCs. We found the protein formulation affected both the matrix structure and the cell behaviors. Increasing the rFI concentration led to larger fiber diameter and denser matrix, and in turn, significantly reduced the cell viability, inhibited cell spreading and growth. Our studies showed fibrin matrices with rFI concentration above 5 mg/ml could not support efficient cell survival (Fig. 3 and 4). Both rFIIa and rFXIIIa were required to form stable fibrin matrices. However, their concentrations at the tested range had a minor influence on the matrix structure and cell behaviors (Fig. 1, 2 and 4). The totally recombinant fibrin matrix could be used to deliver MSCs and enhanced their retention at the injection site. Future research should investigate the long-term effect of the fibrin matrix on cell survival, integration, and function. It will also be valuable to use clinic-relevant disease models such as myocardial infarction and stroke to test the capability of the matrix to retain the cells at the injection sites.

Reference

1. Pittenger, M. F. *et al.* Multilineage potential of adult human mesenchymal stem cells. *Science (80-.).* **284**, 143–147 (1999).

2. Jiang, Y. *et al.* Pluripotency of mesenchymal stem cells derived from adult marrow. *Nature* **418**, 41–49 (2002).

3. Chamberlain, G., Fox, J., Ashton, B. & Middleton, J. Mesenchymal stem cells: their phenotype, differentiation capacity, immunological features, and potential for homing. *Stem Cells* **25**, 2739–2749 (2007).

4. Gang, E. J. *et al.* Skeletal myogenic differentiation of mesenchymal stem cells isolated from human umbilical cord blood. *Stem Cells* **22**, 617–624 (2004).

5. Kulterer, B. *et al.* Gene expression profiling of human mesenchymal stem cells derived from bone marrow during expansion and osteoblast differentiation. *BMC Genomics* **8**, 70 (2007).

6. Park, K. S., Lee, Y. S. & Kang, K. S. In vitro neuronal and osteogenic differentiation of mesenchymal stem cells from human umbilical cord blood. *J. Vet. Sci.* **7**, 343–8 (2006).

7. Hashimoto, J., Kariya, Y. & Miyazaki, K. Regulation of proliferation and chondrogenic differentiation of human mesenchymal stem cells by laminin-5 (laminin-332). *Stem Cells* **24**, 2346–2354 (2006).

8. Gemmis, P. D. E. *et al.* A real-time PCR approach to evaluate adipogenic potential of amniotic fluid-derived human mesenchymal stem cells. *Stem Cells Dev.* **728**, 719–728 (2006).

9. Ma, S. *et al.* Immunobiology of mesenchymal stem cells. *Cell Death Differ.* **21**, 216–225 (2014).

10. Caplan, A. I. Adult mesenchymal stem cells for tissue engineering versus regenerative medicine. *J. Cell. Physiol.* **213**, 341–347 (2007).

11. Tuan, R. S., Boland, G. & Tuli, R. Adult mesenchymal stem cells and cell-based tissue engineering. *Arthritis Res. Ther.* **5**, 32–45 (2003).

12. Banas, A. *et al.* In vivo therapeutic potential of human adipose tissue mesenchymal stem cells after transplantation into mice with liver injury. *Stem Cells* **26**, 2705–2712 (2008).

13. Lee, R. H. *et al.* Multipotent stromal cells from human marrow home to and promote repair of pancreatic islets and renal glomeruli in diabetic NOD/scid mice. *Proc. Natl. Acad. Sci.* **103**, 17438–17443 (2006).

14. Bang, O. Y., Lee, J. S., Lee, P. H. & Lee, G. Autologous mesenchymal stem cell transplantation in stroke patients. *Ann. Neurol.* **57**, 874–882 (2005).

15. Eriksson, M., Taskinen, M. & Leppä, S. From the laboratory bench to the patient's bedside: an update on clinical trials with mesenchymal stem cells. *J. Cell. Physiol.* **207**, 12–22 (2006).

16. Orlic, D. *et al.* Bone marrow cells regenerate infarcted myocardium. *Nature* **410**, 701–705 (2001).

17. Steinberg, G. K. *et al.* Clinical outcomes of transplanted modified bone marrow-derived mesenchymal stem cells in stroke: A phase 1/2a study. *Stroke* **47**, 1817–1824 (2016).

18. Phinney, D. G. & Prockop, D. J. Mesenchymal stem/multipotent stromal cells: the state of transdifferentiation and modes of tissue repair-current views. *Stem Cells* **25**, 2896–2902 (2007).

19. Bruder, S. P., Fink, D. J. & Caplan, A. I. Mesenchymal stem cells in bone development, bone repair, and skeletal regenaration therapy. *J. Cell. Biochem.* **56**, 283–294 (1994).

20. Nagaya, N. *et al.* Intravenous administration of mesenchymal stem cells improves cardiac function in rats with acute myocardial infarction through angiogenesis and myogenesis. *Am J Physiol Hear. Circ Physiol.* **287**, 5–7 (2004).

21. Russo, V., Young, S., Hamilton, A., Amsden, B. G. & Flynn, L. E. Mesenchymal stem cell delivery strategies to promote cardiac regeneration following ischemic injury. *Biomaterials* **35**, 3956–3974 (2014).

22. Shake, J. G. *et al.* Mesenchymal stem cell implantation in a swine myocardial infarct model: engraftment and functional effects. *Ann. Thorac. Surg.* **73**, 1919–1926 (2002).

23. Chen, J. *et al.* Intravenous administration of human umbilical cord blood reduces behavioral deficits after stroke in rats. *Stroke* **32**, 2682–2688 (2001).

24. Lee, J. K. *et al.* Intracerebral transplantation of bone marrow-derived mesenchymal stem cells reduces amyloid-beta deposition and rescues memory deficits in Alzheimer's disease mice by modulation of immune responses. *Stem Cells* **28**, 329–343 (2010).

25. Gutiérrez-Fernández, M. *et al.* Effects of intravenous administration of allogenic bone marrow- and adipose tissue-derived mesenchymal stem cells on functional recovery and brain repair markers in experimental ischemic stroke. *Stem Cell Res. Ther.* **4**, 11 (2013).

26. Hassan, W., Dong, Y. & Wang, W. Encapsulation and 3D culture of human adipose-derived stem cells in an in-situ crosslinked hybrid hydrogel composed of PEG-based hyperbranched copolymer and hyaluronic acid. *Stem Cell Res. Ther.* **4**, 32 (2013).

27. Wu, K. H., Mo, X. M., Han, Z. C. & Zhou, B. Stem cell engraftment and survival in the ischemic heart. *Ann. Thorac. Surg.* **92**, 1917–1925 (2011).

28. Baksh, D., Song, L. & Tuan, R. S. Adult mesenchymal stem cells: characterization, differentiation, and application in cell and gene therapy. *J. Cell. Mol. Med.* **8**, 301–316 (2004).

29. Donzelli, E. *et al.* Mesenchymal stem cells cultured on a collagen scaffold: in vitro

osteogenic differentiation. *Arch. Oral Biol.* **52**, 64–73 (2007).

30. Lei, Y., Gojgini, S., Lam, J. & Segura, T. The spreading, migration and proliferation of mouse mesenchymal stem cells cultured inside hyaluronic acid hydrogels. *Biomaterials* **32**, 39–47 (2011).

31. Lei, Y. & Segura, T. DNA delivery from matrix metalloproteinase degradable poly(ethylene glycol) hydrogels to mouse cloned mesenchymal stem cells. *Biomaterials* **30**, 254–265 (2009).

32. Breen, A., O'Brien, T. & Pandit, A. Fibrin as a delivery system for therapeutic drugs and biomolecules. *Tissue Eng. Part B. Rev.* **15**, 201–214 (2009).

33. Linnes, M. P., Ratner, B. D. & Giachelli, C. M. A fibrinogen-based precision microporous scaffold for tissue engineering. *Biomaterials* **28**, 5298–5306 (2007).

34. Bensaïd, W. *et al.* A biodegradable fibrin scaffold for mesenchymal stem cell transplantation. *Biomaterials* **24**, 2497–2502 (2003).

35. Spotnitz, W. D. Fibrin sealant: the only approved hemostat, sealant, and adhesive-a laboratory and clinical perspective. *ISRN Surg.* **2014**, 1–28 (2014).

36. De Willige, S. U., Standeven, K. F., Philippou, H. & Ariëns, R. A. S. The pleiotropic role of the fibrinogen γ′ chain in hemostasis. *Blood* **114**, 3994–4001 (2009).

37. Gasparotto, V. P. O. *et al.* A new fibrin sealant as a three-dimensional scaffold

candidate for mesenchymal stem cells. *Stem Cell Res. Ther.* **5**, 78 (2014).

38. Cox, S., Cole, M. & Tawil, B. Behavior of human dermal fibroblasts in three-dimensional fibrin clots: dependence on fibrinogen and thrombin concentration. *Tissue Eng.* **10**, 942–954 (2004).

39. Ren, J., Wu, X. & Li, J. Fibrin glue as the cell-delivery vehicle for mesenchymal stromal cells in regenerative medicine. *Cytotherapy* **14**, 555–562 (2012).

40. Horowitz, B. & Busch, M. Estimating the pathogen safety of manufactured human plasma products: Application to fibrin sealants and to thrombin. *Transfusion* **48**, 1739–1753 (2008).

41. Burnouf, T. & Padilla, A. Current strategies to prevent transmission of prions by human plasma derivatives. *Transfus. Clin. Biol.* **13**, 320–328 (2006).

42. Calcaterra, J. *et al.* Recombinant human fibrinogen that produces thick fibrin fibers with increased wound adhesion and clot density. *Biomacromolecules* **14**, 169–178 (2013).

43. Carlson, M. A. *et al.* A totally recombinant human fibrin sealant. *J. Surg. Res.* **187**, 334–342 (2014).

44. Park, D. S., Kim, J. H., Lee, S. W. & Jeong, J. M. Secretory expression of the alpha-subunit of human coagulation factor XIII in the yeast Pichia pastoris. *Biotechnol Lett* **24**, 97–101 (2002).

45. Lovejoy, A. E. *et al.* Safety and pharmacokinetics of recombinant factor XIII-A2 administration in patients with congenital factor XIII deficiency. *Blood* **108**, 57–61 (2006).

CHAPTER 3. THE SYNTHESIS OF A RECOMBINANT FACTOR XIII CROSS-LINKED γγ'-FIBRIN MATRIX HAVING PERIODIC FIBRONECTIN NANOBANDS THAT ACCELERATE WOUND CLOSURE

Introduction

Plasma fibrinogen (F1) consists of two bio-monomer sub-populations when integrated with plasma fibronectin (pFN) form fibrin polymer that is both a hemostatic barrier[1–5] and a provisional matrix needed to initiate wound healing[6–10]. Purified fibrinogen formulations used to form fibrin for culturing cells associated with healing have long been reconstituted to the same mass ratio of 1 fibrinogen to 10 pFN as found in plasma to help optimize colonization of human fibrin in vitro[11]. F1 is linear fibrin precursor that is a hexameric, 340 kDa glycoprotein that includes 2 gamma chains[1,2,12,13] while is pFN is a 2-chain globular, 440 kDa protein. Importantly, about 90% of F1 occurs in circulation as a homodimeric pairing of γ-chains (γγF1)[14] with the remaining occurring as a heterodimeric pairing of γ with a slightly larger, more acidic γ'-chain (γγ'F1) that is associated with a pleotropic biology of vascular health[15,16]. Furthermore, pFN and γγ'F1 coincidentally both occur at about the same concentration in plasma of about 300 μg/ml[16–19].

The formation of the fibrin:pFN polymer begins with thrombin mediated activation of γγF1,γγ'F1 and Factor XIII (pFXIII). The activated fibrinogens produce a semi-soluble, viscoelastic fibrin aggregate[1–3] containing pFN entrained from plasma. The pFXIII is inherently present within the polymerizing fibrin aggregate as a complex with 1 out of every 100 γγ'F1 molecules[15] which disassociates upon formation of activated pFXIII

(pFXIIIa) so as enable efficient intra-fibrin cross-linking activity. This results both in the insoluble pFN:fibrin matrix[4,11,20–22] and its simultaneously cross-linked to the wound surface over the course of about 3 minutes[15,23].

The wound anchored pFN:fibrin also catalyzes healing by the dual colonization of fibroblasts and endothelial cells (ECs) which forms a provisional vascularized tissue called 'granulation tissue[24,25]. It does this through different mechanisms for fibroblasts than for endothelial cells where the colonization by ECs is more tenuously dependent on pFN[4,11,26]. For example, fibroblasts have cellular receptors that recognize R-G-D residues that are presented by pFN after conformational changes induced by FXIII-crosslinking[11,27–30]. In contrast, the predominant interaction of endothelial cells (EC)[31,32] with fibrin is by VE-Cadherin cellular receptors which bind to the β-chain of cross-linked fibrin. Furthermore, the presence of vascular endothelial growth factor (VGEF) and fibroblast growth factor 2 (FGF-2) in cell culture media has been shown to be necessary for catalyzing the EC colonization of fibrin in vitro[31–33]. Thus, far the influence on EC colonization at the length scale of the 3-D fiber presented by the pFN:fibrin matrix has not been well detailed.

The general fiber structure and biological activity of fibrin made from purified γγ'F1 or γγF1 but without discernable levels of pFN has been recently studied[7,15,23]. While there were subtle differences in fiber structure, fibrins made from either γγ'F1 or γγF1 induced similar levels of angiogenesis by ECs in wound healing studied in a normal mouse model[7]. We here describe the synthesis of a viscoelastically strong, 1:1 γγ'F1:pFN fibrin having fibers periodically wrapped with a pFN nanostructure. We report on the ability of

this matrix to enhance EC colonization in vitro and wound closure in a normal mouse model.

Materials and Methods

Materials

All reagents were obtained from Sigma Chemical Company (St. Louis MO) unless otherwise noted. Human source plasma was provided by the U.S. Army Materials Command (Fort Detrick, MD.). Recombinant human thrombin was purchased from ZymoGenetics (Seattle, WA). DEAE Sepharose fast flow, Superose 6 and Gelatin Sepharose were purchased from GE Healthcare (Uppsala, Sweden). 4-12% NuPage Bis-Tris SDS polyacrylamide gels, Colloidal Blue stain and See Blue molecular weight markers were from Invitrogen (Carlsbad, CA). Polyclonal antibody (GMA-034) for human fibrinogen (1:100) was purchased from Green Mountain Antibodies (Burlington, VT). Antibody (ab2413) for human fibronectin (1:200) was from Santa Cruz Biotechnology. Antibodies were reconstituted according to manufacturer's instruction.

Recombinant Factor XIII

Recombinant Factor XIII (rFXIII) was made in *Pichia pastoris* according the methods of Park[34,35]. Briefly, the rFXIII was purified from cell lysates using Ni-IMAC from GE Healthcare. The activity was determined using Pefakit (Pentapharm, Norwalk, CT). The final specific activity of the >95% purity preparations was typically 154 ± 19 Plasma FXIII Equivalent Units/mg (PEU/mg) where the specific activity of pFXIII was 25 u/mg using a peptide incorporation cross-linking assay.

Preparation of fibrinogen and fibronectin from human plasma

Three units of human plasma that had been stored at -80 ºC were thawed at 4 ºC. The plasma was centrifuged at 4000 rpm for 20 min. The supernatant was re-frozen and stored for subsequent purification of fibronectin and other plasma-derived proteins. The cryoprecipitate was re-suspended in 45 mM sodium citrate, 100 mM 6-aminocaproic acid, pH 7.0 at 37 ºC. The solution was then centrifuged for 25 min at 4000 rpm. The pellet was discarded, and the supernatant was treated with a solvent detergent viral inactivation step by addition of 0.15% TnBP, 0.5% Triton X-100 and stirred at room temperature for 60 min. The solvent-detergent treated supernatant was adjusted to 1 M ammonium sulfate by addition of a 4 M stock. The sample was stirred at room temperature for 30 min, and then centrifuged at 2000 rpm for 15 min at room temperature. The pellet was re-suspended in 20 mM sodium citrate, 100 mM NaCl. The sample was dialyzed overnight at room temperature against the same buffer. The dialyzed sample was centrifuged at 2000 rpm for 15 min at room temperature. Any resulting pellet was discarded.

The supernatant was fractionated further to isolate γγF1, γγ'F1 and pFN as described by Siebenlist et al[36] using DEAE Sepharose Fast Flow chromatography at room temperature. The sample was applied to a DEAE column then washed with 10 column volumes of 20 mM sodium citrate, 100 mM NaCl, pH 7.4. The unabsorbed fraction was γγF1. Bound protein was eluted with a linear gradient of 0.1 M to 1.0 M NaCl. The pooled eluate from the DEAE resin produced an approximately equimolar mixture of γγ'F1 and pFN that was dialyzed against 20 mM citrate buffer, 20 mM NaCl at pH 6.8. The dialyzed

mixture was concentrated using a 10 kDa centrifugal ultrafiltration device at 4000 g for 30 min.

Pure pFN and γγ'F1 were produced by application of the DEAE eluate pool to gelatin-Sepharose. Briefly, a 10 ml γγ'F1:pFN mixture was applied to a 3 ml analytical gelatin-Sepharose column. The column was washed with 10 volumes of the dialysis buffer then eluted with the same buffer containing 6 M urea. Samples were analyzed by SDS-PAGE. pFN was eluted by urea while the γγ'F1 fell through the column.

2D adhesion assay

Human foreskin fibroblasts were isolated and cultured in DMEM with 10% FBS[10,37]. The use of primary human fibroblasts from anonymous donors (no subject identifiers and no informed consent) without the use of informed consent was approved by the Institutional Review Board at the University of Nebraska Medical Center and by the Research and Development Committee at the Omaha VA Medical Center. Passage 4 to 6 cells were used. HUEVCs were purchased from Lonza and cultured in EGM2 medium. Passage 3 and 4 cells were used for the experiments. 100 µl fibrin matrix was made in one well of the 96-well plate. $1x10^4$ cells were placed in each well with 200 µl medium. 3 hours after plating, medium and unattached cells were removed. Cells were washed with 200 µl PBS once. Attached cells were recorded with phase-contrast microscope. Alternatively, the cells were fixed with 4% PFA and stained with DAPI. The nuclei were recorded with fluorescence microscope. 100 µl fresh medium with 10 µl alamar blue reagent were added and incubated for 3 hour. 100 µl medium was collected for measuring the fluorescence that

was calibrated to a standard curve to calculate the numbers of attached cells within each well.

3D cell culture within fibrin matrix

100 µl fibrin matrix with $2x10^4$ cells were made in individual wells of a 96-well format plate. 200 µl medium was added to each well. At varied time points after plating, cell morphologies were recorded by phase-contrast microscopy. The medium was removed and 100 µl fresh medium with 10 µl alamar blue reagent were added and incubated for 3 hour. 100 µl medium was collected for measuring the fluorescence that was calibrated to a standard curve to calculate the numbers of cells in each matrix. The viability of cells within the gel was accessed with Live/Dead cell assay kit (Invitrogen) according to the Manufacturer's instruction.

Fibrin formulation

To make the fibrin matrix for the above cell culture experiment, the following fibrin formation components were mixed to the final concentration of the respective fibrinogen (γγF1, γγ'F1) of 2.5 mg/ml total protein; thrombin at 1 U/ml; factor XIIIa at 15.4 U/ml; and 3.3 mg/ml pFN. The mixtures were incubated at 37 ºC for 15 min to form the fibrin matrix.

SEM and confocal microscopy

Fibrin matrices were made according to the formulation above. For SEM, samples were fixed with 2.5% glutaraldehyde in 100 mM phosphate buffer (PH 7.0) at room

temperature for 1 hour, then at 4 ºC overnight. Samples were rinsed with phosphate buffer twice, 10 minutes each. Ethanol dehydration series were performed: 30%, 50%, 70%, 2 x 95%, 2 x 100%, 5 minutes for each procedure. Then samples were treated with hexamethyldisilazane (HMDS) as following: 33% HMDS, 66% HMDS, 2 x 100% HMDS, 2 minutes for each procedure. Samples were left in 100% HMDS to air-dry at least overnight. before sputter-coated with gold-palladium and imaged with the scanning electron microscope (Hitachi S4700 Field-Emission SEM, Hitachi, Tokyo, Japan) at 10 kV and a magnification of 30000. For confocal microscopy, samples were fixed with 4% paraformaldehyde (PFA) at 4 ºC overnight, washed with PBS for 3 times, permeabilized with 0.25% Triton X-100 for 15 minutes, and blocked with 5% goat serum for 1 hour before incubating with primary antibodies at 4 ºC overnight. After extensive washing, secondary antibodies were added and incubated for 2 hours at room temperature and. Samples were then washed with PBS before imaged with confocal microscope (Nikon A1-R confocal system on a Nikon Eclipse 90i upright fluorescence microscope).

Animal research

All animal protocols were approved by the Institutional Animal Care and Use Committee of the University of Nebraska-Lincoln. All experimental procedures involving animals were performed in accordance with the guidelines of the Institutional Animal Care and Use Committee of the University of Nebraska-Lincoln. The mouse excisional wound splinting model was descripted previously[38]. Briefly, donut-like splints with 5-mm diameter of the center hole and 15-mm diameter of the disc were created. The splints were sterilized in 70% ethanol before experiment. Mice were anesthetized. Two symmetrical 5-

mm full-thickness excisional wounds were created on the back of each mouse. The splint was carefully placed around the wound and secured to the skin with eight interrupted sutures. The left wound was sealed with 50 μl γγ'F1:pFN fibrin matrix, while the right wound was added with 50 μl γγF1:pFN fibrin matrix. The total protein concentration are 2.5 mg/ml fibrinogen and 3.3 mg/ml fibronectin; 15.4U/ml rFXIII, 0.2 μg/ml VEGF, and 1 U/ml recombinant thrombin were used to form the fibrin matrix. The wounds were covered with sterile transparent dressing. On days 2, 4, 6, and 9, additional 20 μl of the fibrin matrix were added to the wounds.

Frozen section and Hematoxylin and Eosin (H&E) staining

Mice were sacrificed on day 15. The wound tissues were carefully harvest. The wound area was calculated before dissecting each wound across the center into two equal pieces. The wound tissues were fixed in cold 4% (wt/vol) paraformaldehyde in PBS at 4 ℃ overnight and submerge into 30% sucrose in PBS at 4 ℃ until the sinks. Tissues were embedded in OCT compound and freeze in - 70 ℃. 40-μm thick cryostat sections were cut. The sections were wash with PBS subsequently stained with hematoxylin (RICCA, Arlington, TX) and eosin. Images were taken by EVOS® FL Auto Cell Imaging System.

Statistical analyses

The data are presented as the mean ± S.D.. We used an unpaired t-test to compare two groups and one-way ANOVA to compare more than two groups. $P < 0.05$ was considered statistically significant.

Results

The naturally occurring mass ratio of pFN within the total F1 population in human plasma is about 1:10 and which naturally coincides with about a 1:1 molar ratio of pFN with the γγ'F1 subpopulation. Our experimental focus reported here is the study *in vitro* and *in vivo* of novel cross-linked fibrin matrices using recombinant Factor XIII (rFXIII) made from each of the fibrinogen sub-populations and with or without pFN.

Fibrin formulation and material characteristics

The biological function related to the naturally occurring plasma ratios of pFXIII, pFN, and F1 have been established in the context of normal hemostasis and wound healing *in vivo*. Here we have focused on enhancing this function by making a unique cross-linking of pFN into fibrin made either from γγF1 or from γγ'F1. We do this in the context of the natural 1:1 ratio that γγ'F1 occurs with pFN while using much higher levels of cross-linking activity supplied by rFXIII. We made high purity γγF1, γγ'F1 and pFN from human plasma as shown by Coomassie blue stained SDS-PAGE under reducing conditions (**Figure 3.1A)**. As part of that processing and due to their similar degrees of acidity, we were able to purify a fraction which contained an approximately 1:1 γγ'F1 and pFN (here designated γγ'F1:pFN). The rFXIIIa used here had a novel specific cross-linking activity was 154 U/mg which was about 6-fold higher than plasma-derived FXIII (**Figure 3.1B**). We used a commercially available, biotherapeutic grade recombinant thrombin and our rFXIIIa to make fibrin matrices from based upon the naturally occurring stoichiometric plasma molarity of γγ'F1 and pFN (**Figure 3.1C-F**). Fibrins made at the same fibrinogen

concentrations were evaluated when made from γγF1 alone, γγ'F1 alone, and the 1:1 γγ'F1:pFN obtained from the DEAE eluate fraction and a 1:1 mixture of γγF1 and pFN (designated here as γγF1:pFN).

We characterized both the kinetics of the formation of the fibrins and the resulting viscoelastic strengths of the fibrins made at different levels of rFXIII using TEG (**Figure 3.1C-F**) where the data range bars are small or almost imperceptible. The highest strength obtained at the lowest F1 concentration which the TEG could reliably measure occurred at about a 5:1 molar ratio of F1 to rFXIII (**Figure 3.1C-F**). This rFXIIIa activity level was estimated to be about 20-fold or higher (2 units/nmol F1) than the trace amounts of FXIII activity that typically associates with the γ' chain of γγ'F1 (estimated to be 0.08 units/nmol F1) and which typically co-purifies with biotherapeutic grade plasma F1 products. All treatment groups of different rFXIII levels respectively possessed a similar time course polymerization pattern and an equivalent viscoelastic strength. Interestingly, the presence of a 1:1 total F1 to pFN molar ratio (**Figure 3.1D, 3.1F**) further lowered the viscoelastic strength of both fibrins made from γγF1 or γγ'F1 showing the impact of pFN in the fibrin:pFN polymerization process.

Our studies chose the fibrin formulation with the lowest level of 2.5 mg/ml F1 while at a level of rFXIII activity as to produce a fibrin facile for wound application in the studies presented below. All of these fibrins made with or without pFN yielded a sufficiently stable tissue sealant with rapid wound adhesion as applied in our mouse model studies. In summary, for *in vitro* cell culture analysis and *in vivo* wound applications, we chose a level

of 15.5 U/ml rFXIIIa to sufficiently stabilize the fibrin by cross-linking the fibrins at the low level of 2.5 mg/ml of γγ'F1 or γγF1.

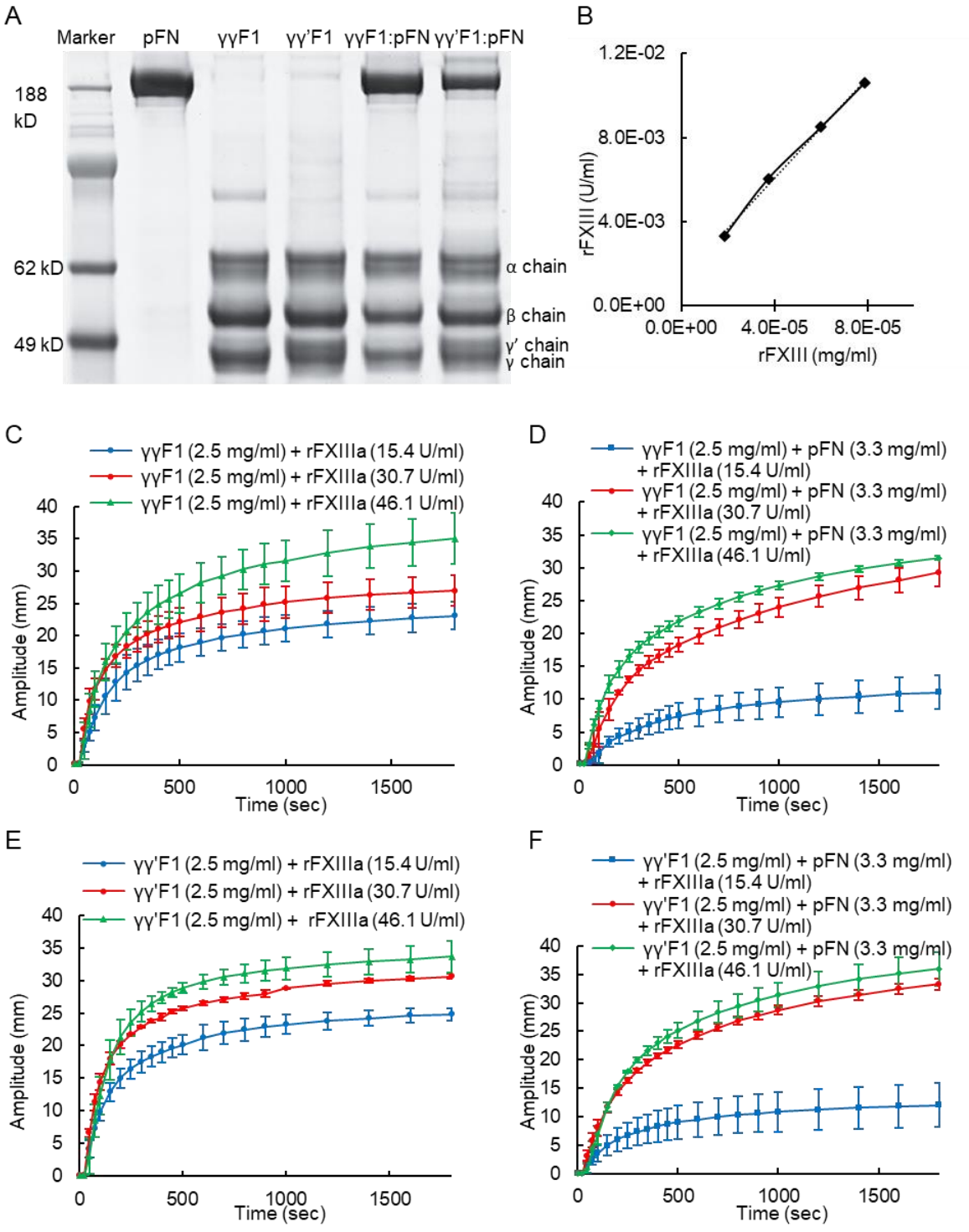

Figure 3.1. Material characteristics. (A) Reducing SDS-PAGE gel. (B) rFXIIIA1 activity (153.5 ± 19 U/mg) was estimated by the 5-(biotinamido) pentylamine incorporation assay. The effect of rFXIIIa on the viscoelastic and clotting kinetics of γγF1 (C), γγF1 and pFN (D), γγ'F1 (E), and γγ'F1 and pFN (F) were evaluated by TEG assay.

Our in vitro studies of the fibrins focused primarily on culture behavior most relevant to the wound healing phenomena associated with fibroblasts and ECs[8,27]. **Figure 3.2A** shows the fiber networks we observed by SEM for the four fibrin formulations. All matrices showed a similar frequency of branch points and the similar range of fiber diameters ranging primarily from about 250 to 350 nm. Generally, F1 reactive immunostaining to either γγF1 or γγ'F1 and confocal microscopy was used to study the distribution of pFN within the fibrin matrices (**Figure 3.2B, 3.2C**). A sporadic appearance of irregularly sized pFN aggregates was observable within the fibrin matrix made from γγF1:pFN. In contrast, the fibrin made from the γγ'F1:pFN mixture presented pFN aggregates as a regularly occurring banded structure that was wrapped around the fibers with an axial dimension of about 300-400 nm that was displayed throughout the matrix (**Figure 3.2B, 3.2C**).

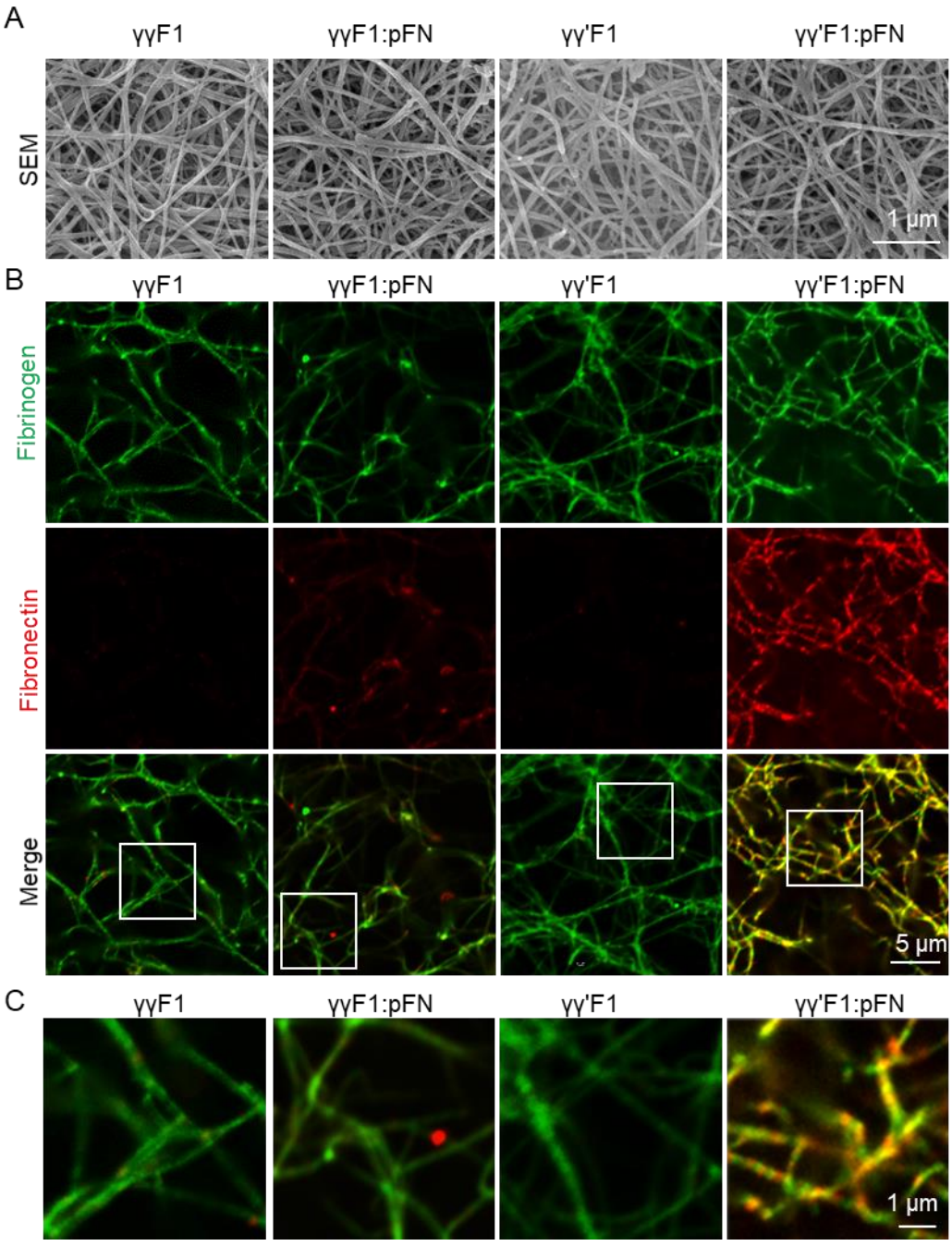

Figure 3.2. Scanning electron microscopy (A) and confocal microscopy (B) images of fibrin matrices made from γγF1, γγ'F1, a 1:1 mixture of γγF1 and pFN, or a 1:1 mixture of γγ'F1 and pFN. (C) Zoom-in images of squared areas in (B).

In vitro evaluation of fibrin biological activity for fibroblasts

Fibroblasts have been previously shown to grow robustly on fibrin in the presence of pFN made from a ratio of 10 F1 to 1 pFN[7,27–30]. The adhesion of fibroblasts to the surface of our fibrin matrices was measured on 2-D format for 3 hours which is a time established to be sufficient for cellular adhesion (**Figure 3.3A**). The nuclei of attached fibroblasts were stained by DAPI. Adhered cells were also quantified with alarmar blue assay (**Figure 3.3D**). These 2-D culture results showed nearly 100% of the plated fibroblasts adhered to all four of these matrices. We observed fibroblasts after embedding within each of the 4 fibrin matrices (**Figure 3.3B, 3.3C**). After 48 hours of this 3-D culturing a normal and healthy progression to an extended morphology occurred within all matrice types. Good viability was also indicated by live/dead cell staining. In particular, the fibroblasts had expanded about 6-fold within γγ'F1:pFN matrix and about 4-fold in each of the other three fibrin formulations. Thus, all of the fibrin materials induced fibroblast viability which was similar to that reported in the literature for fibrin with or without pFN[7,27–30].

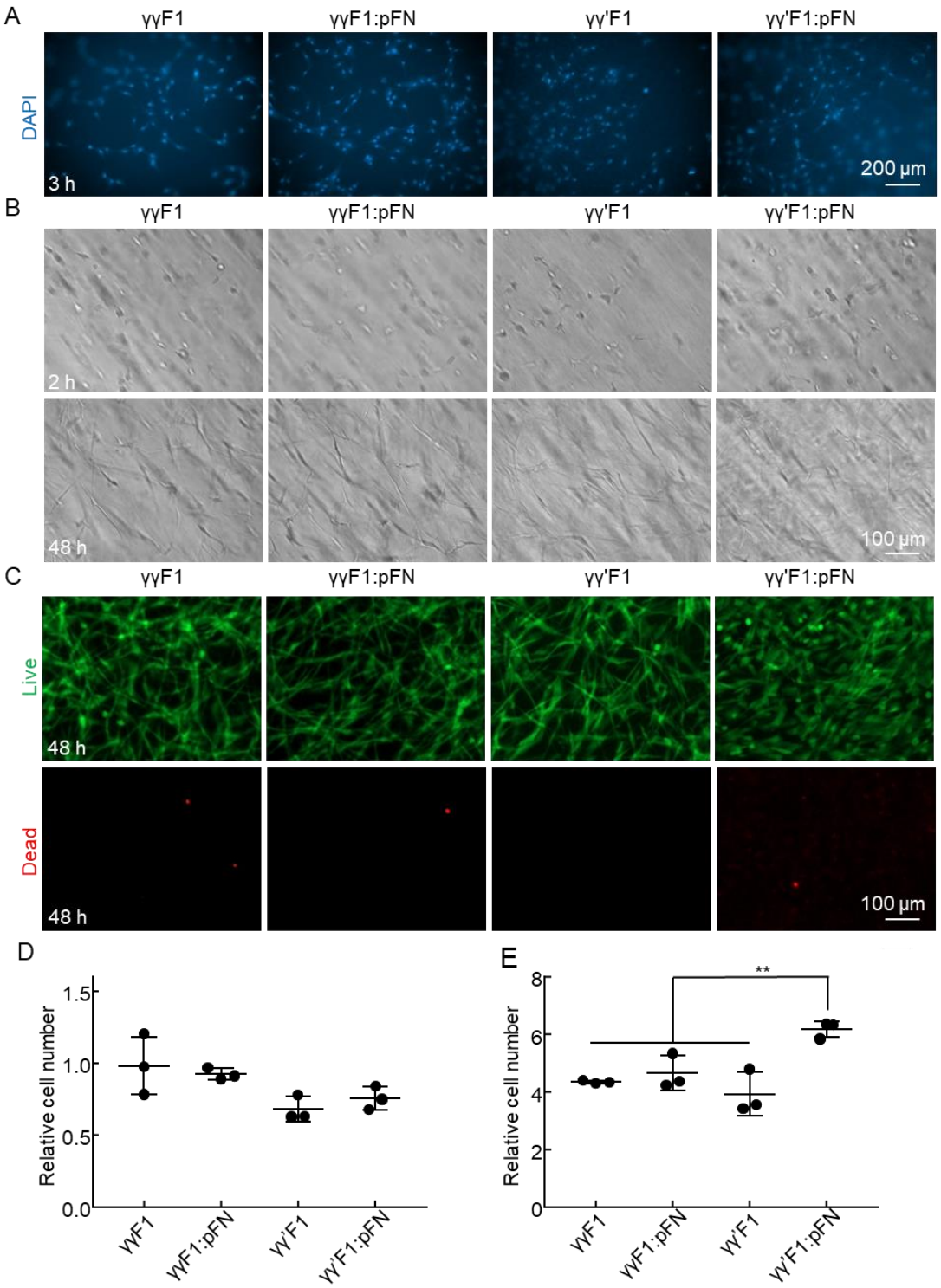

Figure 3.3. Culturing primary human fibroblasts on top of (A,D) and within 3D fibrin matrices (B,C,E). (A) The nuclei of cells attached to fibrin matrices at 3 hr. (B) Fibroblasts in 3D fibrin matrices at 2 h and 48 h. (C) Live and dead cells at 48 h. (D) Cells attached to the fibrin matrices were quantified with alamar blue assay. (E) Cells in 100 µl fibrin matrices at 48 h were quantified with alamar blue assay. Cell numbers are related to the initial seeded cells. **: $p<0.01$.

In vitro evaluation of fibrin biological activity for ECS

Recent studies have shown that culture of ECs on γγF1 or γγ'F1 fibrin is greatly more tenuous than the culture of fibroblasts using preparations which showed no visible pFN content by SDS-PAGE. Our studies showed that HUVECs cultured in 2-D exhibited some degree of adherence after 3 hours to all fibrin matrices studied here (**Figure 3.4A**). However, quantification showed that nearly 100% of HUVECs attached to the 2-D γγ'F1:pFN matrix, while only about 50% of HUVECs attached to the other three fibrin matrices (**Figure 3.4D**). We then used 3-D culture of HUVECs within the fibrin matrices: after 48 hours on γγF1, γγ'F1, and 1:1 γγF1:pFN fibrin matrices showed spherical morphology, indicating a poor adhesion that is characteristic of apoptosis (**Figure 3.4B, 3.4C**). This apoptotic profile was confirmed by live/dead cell staining (**Figure 3.4C**). In contrast, HUVECs cultured within γγ'F1:pFN showed no evidence of apoptosis while having a high level of morphologically healthy sprouting. Quantification clearly showed a 3-fold expansion of these ECs within the γγ'F1:pFN matrix relative to the low level of expansion observed for the other fibrins (**Figure 3.4E**).

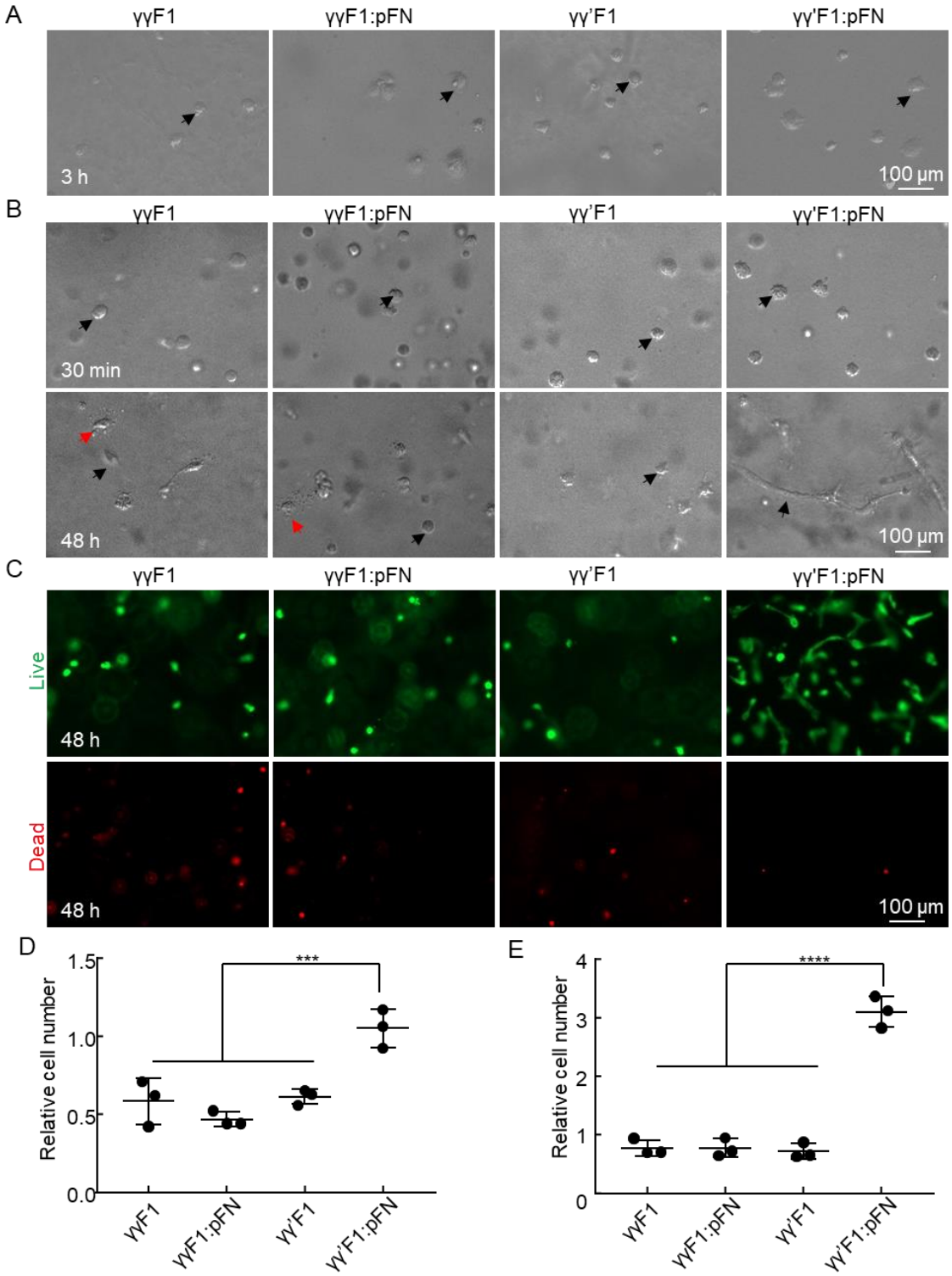

Figure 3.4. Culturing primary human umbilical vein endothelial cells (HUVECs) on top of (A,D) and within 3D fibrin matrices (B,C,E). (A) HUVECs attached to fibrin matrices at 3 h. (B) HUVECs in 3D fibrin matrices at 30 min and 48 h. Red and black arrows point to apoptotic and live cells, respectively. (C) Live and dead cells at 48 h. (D) Cells attached to the fibrin matrices were quantified with alamar blue assay. (E) Cells in 100 µl fibrin matrices at 48 h were quantified with alamar blue assay. Cell numbers are related to the initial seeded cells. ***: $p<0.001$ and ****: $p<0.0001$.

In vivo wound mouse dermal wound closure model

We studied healing in wounds sealed by γγ'F1:pFN fibrin using paired, dermal wound model in normal mice. We paired the 1:1 γγF1:pFN mixture as the wound control treatment group because it did not form a banded pFN fibrin nanostructure. Successive wound sealing applications were done on day 0, 2, 4, 6 and 9 for each of the two treatments that were juxta-positioned within each given mouse. After 15 days, we observed that the open area of the wounds sealed with fibrin made from γγ'F1:pFN were smaller relative to that treated with fibrin made from γγF1:pFN (**Figure 3.5A, 3.5D**). Histology showed a native granulation tissue profile across the remaining, not fully closed wound surface (typical histological cross-section shown in **Figure 3.5B**), where open wounds treated with fibrin made from γγF1:pFN were markedly less advanced towards closure (zoomed in view **Figure 3.5C**).

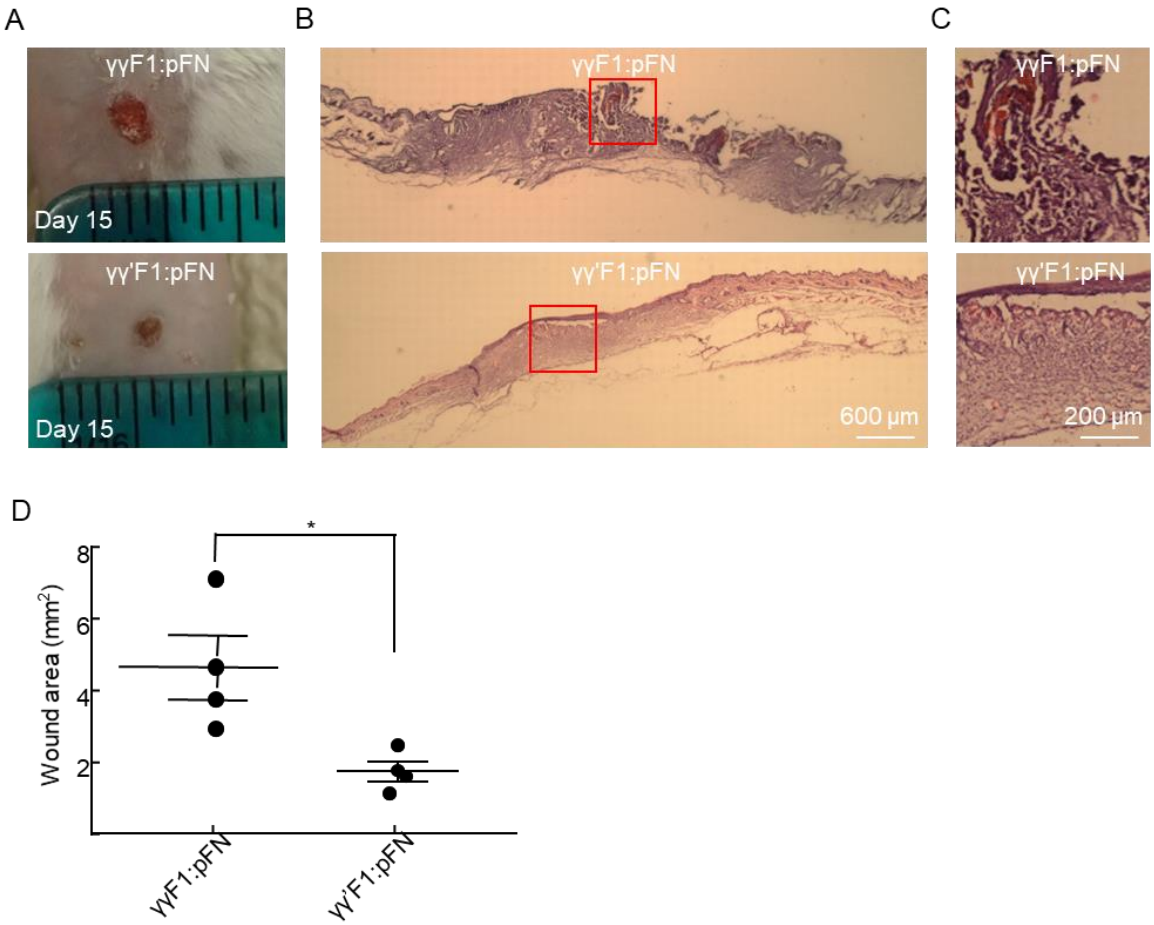

Figure 3.5. Mouse skin wounds treated with fibrin matrices. (A) Wounds treated with γγF1:pFN or γγ'F1:pFN matrix on day 15. (B) H&E staining.(C) Zoom-in images of squared areas in (B). (D) Wound areas on day 15. *: $p<0.05$.

Discussion and conclusion

Our fibrin engineering is based upon the pleotropic biological activities of γγ'F1 with respect to vascular physiology[15] and the known catalytic properties of pFN for wound healing. Fibronectin also plays a mechanical role in augmenting fibrin strength. Furthermore, both γγ'F1 and pFN occur at nearly a 1:1 molar ratio in normal human plasma[16,18,19,29]. This is consistent with the 1:10 ratio of pFN to F1 typically present in fibrinogen preparations that is considered an optimal composition for fibrin based cell culture of fibroblasts[11]. Fibronectin also plays a mechanical role in augmenting fibrin strength[5,25]. We were able to produce a mixture containing a 1:1 ratio of pFN and γγ'F1 using anion exchange chromatography of fibrinogen-pFN concentrates obtained by classical precipitation. This procedure exploited the similar acidity of pFN and γγ'F1 and also enabled isolation of γγF1. We further isolated pFN from the γγ'F1 DEAE eluate mixture using collagen affinity chromatography. The fibrins respectively made here from the core γγ'F1 and γγF1 and were similar in formation kinetics as measured by TEG, range of fibrin diameters and branch points. The γγ'F1:pFN and γγF1:pFN fibrins were stronger than respective γγ'F1 and γγF1 formulations confirming that the presence of pFN strengthens fibrin.

The cross-linking activity needed for the formation of an effective hemostatic fibrin barrier and integration of pFN is normally supplied by a complex of pFXIII with γγ'F1[17,23]. Here we augmented this activity by >20-fold using rFXIII to produce a strong fibrin matrix when formed over a range of 2.5-4.5 mg/ml F1. In general, we observed that decreasing the F1 levels resulted in fibrin mechanical properties that provided more dexterous mouse

wound application were effectively made at the F1 levels which normally occur in human plasma. However, a facile kinetic balance between rapid polymerization and wound adhesion of the fibrin during wound surface application was possible due to the high levels of rFXIII activity.

Importantly, the elevated cross-linking activity here also induced the formation of pFN aggregates. Relative to the other fibrins studied, the γγ'F1:pFN fibrin was unique in its high efficiency for both fibroblast and EC colonization *in vitro* as well as normal wound closure and healing. Because of the similarities in core fiber matrix structure among all fibrins studied here, the enhanced interaction of ECs with γγ'F1:pFN fibrin was likely due to its unique presence of the pFN aggregate fiber wrappings. An enhanced ability of ECs to engage with the γγ'F1:pFN fibrin was observed with both 2-D and 3-D culture experiments: the 2-D culturing of ECs showed a rapid establishment of cell adhesion points which initiated cell elongation while the 3-D culture showed robust survival, proliferation and vascular morphogenesis. In contrast, the other fibrins were associated with a greater extent of apoptosis in 3-D culture. To our knowledge, this is the first report of enhanced EC colonization and healing using a γγ'F1:pFN fibrin matrix.

The initiation of cellular engagement by fibroblasts with fibrin containing pFN is well known to be provided by FXIII cross-linking that converts pFN to a conformationally active form[11]. However, this activity has not been specifically associated with EC recruitment by pFN so as to result vascularization of granulation tissue[24,31]. Our study supports an rFXIII induced activation of pFN conformation within the aggregate wrappings that are periodically presented throughout the γγ'F1:pFN fibrin matrix. In contrast, the

sporadically occurring and irregular aggregates of pFN formed within the γγF1 fibrin did not enhance EC colonization. It is noted that VEGF and FGF-2 are known to promote the initial colonization of either γγ'F1 or γγF1 fibrin by EC[32,33] but not the entire sequence leading to vascular morphogenesis.

In summary, our wound healing results reinforce the enhanced colonization of both EC and fibroblasts on γγ'F1:pFN fibrin that were observed *in vitro*. Fibroblasts cultured in 3-D have been shown to be stimulated on collagen that axially presented aggregates of about 90 pFN molecules that were dispersed along the matrix fibers. [37,39] In the future, we will continue our *in vitro* study of the EC colonization and potential integrin-pFN activity with the pFN wrapped γγ'F1 fibers and its impact on the vascularization phenomena associated with wound healing

Reference

1. McKee, P. A., Mattock, P. & Hill, R. L. Subunit structure of human fibrinogen, soluble fibrin, and cross-linked insoluble fibrin. *Proc. Natl. Acad. Sci. U. S. A.* **66**, 738–744 (1970).

2. Chen, R. & Doolittle, R. F. Identification of the polypeptide chains involved in the cross-linking of fibrin. *Proc. Natl. Acad. Sci. U. S. A.* **63**, 420–427 (1969).

3. Mosesson, M. W. Fibrin polymerization and its role in regulating hemostasis. in *New Trends in Haemostasis* vol. 116 27–43 (1990).

4. Mosher, D. F. & Johnson, R. B. Specificity of fibronectin-fibrin cross-linking. *Ann. N. Y. Acad. Sci.* **408**, 583–594 (1983).

5. Wang, Y. *et al.* Plasma fibronectin supports hemostasis and regulates thrombosis. *J. Clin. Invest.* **124**, 4281–4293 (2014).

6. Sierra, D. H. Fibrin sealant adhesive systems: a review of their chemistry, material properties and clinical applications. *J. Biomater. Appl.* **7**, 309–352 (1993).

7. Cheung, E. Y. L. *et al.* Specific effects of fibrinogen and the γA and γ'-chain fibrinogen variants on angiogenesis and wound healing. *Tissue Eng. Part A* **21**, 106–14 (2015).

8. Mendez, J. J. *et al.* Mesenchymal stromal cells form vascular tubes when placed in fibrin sealant and accelerate wound healing in vivo. *Biomaterials* **40**, 61–71

(2015).

9. ROSTAGNO, A. A., SCHWARZBAUER, J. E. & GOLD, L. I. Comparison of the fibrin-binding activities in the N- and C-termini of fibronectin. *Biochem. J.* **338**, 375–386 (1999).

10. Spotnitz, W. D. Fibrin sealant: the only approved hemostat, sealant, and adhesive-a laboratory and clinical perspective. *ISRN Surg.* **2014**, 1–28 (2014).

11. Corbett, S. A., Wilson, C. L. & Schwarzbauer, J. E. Changes in cell spreading and cytoskeletal organization are induced by adhesion to a fibronectin-fibrin matrix. *Blood* **88**, 158–166 (1996).

12. Weisel, J. W. & Medved, L. Fibrinogen and Fibrin. *Adv. Protein Chem.* **70**, 247–299 (2005).

13. Spraggon, G., Everse, S. J. & Doollttle, R. F. Crystal structures of fragment D from human fibrinogen and its crosslinked counterpart from fibrin. *Nature* **389**, 455–462 (1997).

14. Tennent, G. A. *et al.* Human plasma fibrinogen is synthesized in the liver. *Blood* **109**, 1971–1974 (2007).

15. De Willige, S. U., Standeven, K. F., Philippou, H. & Ariëns, R. A. S. The pleiotropic role of the fibrinogen γ′ chain in hemostasis. *Blood* **114**, 3994–4001 (2009).

16. Chung, D. W. & Davie, E. W. gamma and gamma' chains of human fibrinogen are produced by alternative mRNA processing. *Biochemistry* **23**, 4232–4236 (1984).

17. Ariens, R. A. S. Role of factor XIII in fibrin clot formation and effects of genetic polymorphisms. *Blood* **100**, 743–754 (2002).

18. Hynes, R. O. & Yamada, K. M. Fibronectins: Multifunctional modular glycoproteins. *J. Cell Biol.* **95**, 369–377 (1982).

19. Mosher, D. F. Physiology of fibronectin. *Annu. Rev. Med.* **35**, 561–575 (1984).

20. Mosher, D. F. Cross-linking of cold-insoluble globulin by fibrin-stabilizing factor. *J. Biol. Chem.* **250**, 6614–6621 (1975).

21. Takagi, T. & Doolittle, R. F. Amino acid sequence studies on factor XIII and the peptide released during its activation by thrombin. *Biochemistry* **13**, 750–756 (1974).

22. Makogonenko, E., Tsurupa, G., Ingham, K. & Medved, L. Interaction of fibrin(ogen) with fibronectin: Further characterization and localization of the fibronectin-binding site. *Biochemistry* **41**, 7907–7913 (2002).

23. Siebenlist, K. R. *et al.* Studies on the basis for the properties of fibrin produced from fibrinogen-containing γ′ chains. *Blood* **106**, 2730–2736 (2005).

24. McClain, S. a *et al.* Mesenchymal cell activation is the rate-limiting step of granulation tissue induction. *Am. J. Pathol.* **149**, 1257–1270 (1996).

25. Kamykowski, G. W., Mosher, D. F., Lorand, L. & Ferry, J. D. Modification of shear modulus and creep compliance of fibrin clots by fibronectin. *Biophys. Chem.* **13**, 25–28 (1981).

26. Ugarova, T. P. *et al.* Conformational transitions in the cell binding domain of fibronectin. *Biochemistry* **34**, 4457–4466 (1995).

27. Grinnell, F., Feld, M. & Minter, D. Fibroblast adhesion to fibrinogen and fibrin substrata: Requirement for cold-insoluble globulin (plasma fibronectin). *Cell* **19**, 517–525 (1980).

28. Greiling, D. & Clark, R. A. Fibronectin provides a conduit for fibroblast transmigration from collagenous stroma into fibrin clot provisional matrix. *J. Cell Sci.* **110**, 861 LP – 870 (1997).

29. Knox, P., Crooks, S. & Rimmer, C. S. Role of fibronectin in the migration of fibroblasts into plasma clots. *J. Cell Biol.* **102**, 2318–2323 (1986).

30. Clark, R. A. F., An, J. Q., Greiling, D., Khan, A. & Schwarzbauer, J. E. Fibroblast migration on fibronectin requires three distinct functional domains. *J. Invest. Dermatol.* **121**, 695–705 (2003).

31. Cheresh, D. A. Human endothelial cells synthesize and express an Arg-Gly-Asp-directed adhesion receptor involved in attachment to fibrinogen and von Willebrand factor. *Proc. Natl. Acad. Sci.* **84**, 6471–6475 (1987).

32. Sahni, A., Francis, C. W. & Dc, W. Vascular endothelial growth factor binds to

fibrinogen and fibrin and stimulates endothelial cell proliferation Vascular endothelial growth factor binds to fibrinogen and fibrin and stimulates endothelial cell proliferation. *Blood* **96**, 3772–3778 (2014).

33. Sahni, A., Sporn, L. A. & Francis, C. W. Potentiation of endothelial cell proliferation by fibrin(ogen)-bound fibroblast growth factor-2. *J. Biol. Chem.* **274**, 14936–14941 (1999).

34. Carlson, M. A. *et al.* A totally recombinant human fibrin sealant. *J. Surg. Res.* **187**, 334–342 (2014).

35. Park, D. S., Kim, J. H., Lee, S. W. & Jeong, J. M. Secretory expression of the alpha-subunit of human coagulation factor XIII in the yeast Pichia pastoris. *Biotechnol Lett* **24**, 97–101 (2002).

36. Siebenlist, K. R., Meh, D. A. & Mosesson, M. W. Plasma factor XIII binds specifically to fibrinogen molecules containing γ' chains. *Biochemistry* **35**, 10448–10453 (1996).

37. Carlson, M. A., Smith, L. M., Cordes, C. M., Chao, J. & Eudy, J. D. Attachment-regulated signaling networks in the fibroblast-populated 3D collagen matrix. *Sci. Rep.* **3**, 1880 (2013).

38. Wang, X., Ge, J., Tredget, E. E. & Wu, Y. The mouse excisional wound splinting model, including applications for stem cell transplantation. *Nat. Protoc.* **8**, 302–309 (2013).

39. Sevilla, C. A., Dalecki, D. & Hocking, D. C. Regional fibronectin and collagen fibril co-assembly directs cell proliferation and microtissue morphology. *PLoS One* **8**, e77316 (2013).

CHAPTER 4. ENGINEERED HUMAN BROWN ADIPOCYTE MICROTISSUES IMPROVED GLUCOSE AND INSULIN HOMEOSTASIS IN HIGH FAT DIET-INDUCED OBESE AND DIABETIC MICE

Introduction

According to World Health Organization data, about 10% of adults have obesity (OB), and the population with OB-associated T2DM will reach 300 million by 2025[1]. There are currently no safe and long-lasting approaches to prevent/treat OB and T2DM[2]. Healthy humans have a substantial amount of BAT, a tissue that augments the whole-body energy expenditure. Large clinical data shows BAT activity inversely correlates to body mass index, plasma glucose, and triglycerides levels, and insulin resistance, and BAT activity is a negative predictor of T2DM, dyslipidemia, coronary artery disease, cerebrovascular disease, congestive heart failure, and hypertension[3–5]. Furthermore, the beneficial effects of BAT are more pronounced in obese individuals, suggesting the importance of this tissue for the obese population[3–5].

Clinical studies have shown that augmenting BAT activities using pharmaceuticals (e.g., mirabegron[6], glucocorticoids[7], BIBO3304[8]), or cold stimulation[9–12] enhances the whole-body energy expenditure, glucose tolerance, and insulin sensitivity[13–15]. These findings suggest that BAT is a promising therapeutic target. However, these BAT-activating approaches require sustained treatments, have significant side effects[16], and may not work long-term. Additionally, they may work poorly on patients with a low abundance

of BATs, such as obese and senior individuals (a population mostly affected by OB and its associated diseases).

An alternative approach to overcome these problems is to augment BAT mass and activity via tissue transplantation. Several groups transplanted BAT (0.1-0.2 g) from healthy mouse donors to diet-induced or genetically obese mice[17–20]. The transplantation significantly reduced plasma glucose, triglyceride, lipid levels, body weight gain, fat composition, and hepatic steatosis[19,20] while increasing the body energy expenditure, oxygen consumption rate (OCR), glucose homeostasis, and insulin sensitivity[21,22]. Transplanted BAT could directly burn fatty acids and glucose and dissipate the energy as heat via non-shivering thermogenesis (e.g., act as an energy sink)[15,16]. They also secreted soluble factors and exosomes that enhanced glucose uptake and energy expenditure in the heart, muscle, and WAT (e.g., act as an endocrine organ)[13,23–27]. Although few studies have used T2DM mice as recipients, research found that transplanting mouse BAT into streptozotocin (STZ)-induced diabetic mice prevented and reversed type 1 diabetes mellitus (T1DM)[21,28].

To date, most transplantation studies used mouse BATs, and it is uncertain whether these therapeutic effects, cellular and molecular mechanisms would be applied to human BAT since human and mouse BATs have distinct differences[29]. However, human BAT is located at deep organs, e.g., the supraclavicular, perirenal/adrenal, and paravertebral regions, and isolating sufficient human BAT for transplantation and research is challenging[30]. The Tseng group recently isolated and immortalized human brown adipocyte progenitors (BAPs) and found that these BAPs, when transplanted with Matrigel,

could prevent/reverse diet-induced OB and metabolic disorders[31]. Interestingly, they also showed that human white preadipocytes activated to express endogenous UCP-1 had similar effects, indicating the importance of UCP-1 protein[32]. The study transplanted a large number (1.5-2x10^7 cells per animal) of proliferating BAPs, which have potential tissue overgrowth risk. It also used Matrigel, an extracellular matrix (ECM) extracted from mouse tumors that contain hundreds of undefined components. Matrigel is not compatible with clinical applications.

To address these limitations, we explored if transplanting a low dose of mature BAs (differentiated from the above BAPs) in the absence of Matrigel could alleviate HFD-induced OB, metabolic symptoms, and T2DM in mice. When harvesting the fully differentiated BAs cultured in the conventional two-dimensional (2D) cell culture dishes, the trypsin-based dissociation killed a large percentage of cells. Additionally, the remaining BAs had a very low survival rate after transplantation. We thus proposed to prepare injectable 3D BA microtissues to overcome these problems. Here, we report the BA microtissue fabrication method, their survival, safety, and capability to improve glucose and insulin homeostasis and manage body weight gain in HFD-induced OB and diabetic mice.

Materials and Methods

2D cell culture and differentiation

Immortalized BAPs are gifts from Dr. Tseng at Harvard University(Xue et al>, 2015). We followed published methods to culture BAPs[34,35]. Briefly, BAPs were cultured

in Dulbecco's Modified Eagle Medium (DMEM, HyClone, #SH30003.03) supplemented with 10% FBS (Atlanta biologicals, #S11150). When cells reached 80% confluence, they were passaged (1:3) with 0.25% trypsin-EDTA (Giboco, #25200056). To induce differentiation, BAPs were seeded at $0.5x10^4$ cells/cm^2 and maintained in the growth medium to reach confluence. Then cells were cultured in differentiation medium I consisting EBM-2 (Lonza, #CC-3156), 0.1% FBS, 5 μM SB431542 (Selleckchem, #S1067), 25.5 μg/ml ascorbic acid (Sigma, #A89605G), 4 μg/ml hydrocortisone (Sigma, #H0396), 10 ng/ml Epidermal Growth Factor (Peprotech, # 100-15), 0.2 nM 3,3′,5-Triiodo-L-thyronine (T3, Sigma, #T2877), 170 nM insulin (Sigma, #I9287-5ML), 1 μM rosiglitazone (Sigma, #R2408), 0.5 mM 3-Isobutyl-1-methylxanthine (IBMX, Sigma, #I5879) and 0.25 μM dexamethasone (Sigma, #D4902) for 3 days, then in differentiation medium II (differentiation medium I without IBMX and dexamethasone) with medium change once a week. Mature BAs could be obtained 20–30 days after induction.

Fabricating 3D BA microtissues in microwells

Aggrewells (Stemcell Technologies #34815, #34425) were pre-treated with anti-adherence rinsing solution (Stemcell Technologies, #07010) following the manufacturer's instruction. Single BAPs were seeded into Aggrewells with differentiation medium I. Differentiation medium II was used after three days and refreshed once a week. Differentiated BA microtissues were collected by centrifugation at 100 g for 3 min.

Fabricating 3D BA microtissues in shaking plates

Single BAPs were suspended in differentiation medium I in a low adhesion 6-well plate (Corning, #3471) shaking at 75 rpm. Detailed methods of culturing cells in shaking plates can be found in our previous publications[36–40]. Differentiation medium II was used after three days and refreshed once a week. The plate was tilted and placed in static for 5 min to settle down the microtissues to change medium. 90% of the exhausted medium was replaced with fresh medium. BA microtissues were collected by pipetting the medium up and down to suspend the microtissues and spinning at 100 g for 3 min.

Fabricating 3D BA microtissues in thermoreversible hydrogels

Single BAPs were suspended in growth medium I in low adhesion 6-well plate shaking at 75 rpm overnight to form BAP spheres. The spheres were then mixed with 10% ice-cold PNIPAAm-PEG (Cosmo Bio, #MBG-PMW20-5005) solution dissolved in DMEM medium. The mixture was then cast on a tissue culture plate and incubated at 37 °C for 10 min to form a hydrogel before adding the pre-warmed differentiation medium I. Differentiation medium II was used after three days and refreshed once a week. To harvest BA microtissues, the medium was removed, and ice-cold DPBS (Life Technologies, #21600044) was added to dissolve the hydrogel for 5 min. Finally, BA microtissues were collected by spinning at 100 g for 3 min. Detailed methods of encapsulating cells in this thermoreversible hydrogel can be found in our previous publications[36,40–44].

3D microtissues transplantation

The animal experiments were conducted following the protocols approved by the University of Nebraska–Lincoln Animal Care and Use Committee. 6 mice were used for each study group. 6-week-old male B6.129S7-Rag1tm1Mom/J or Rag1 knock-out mice ($Rag1^{-/-}$) were purchased from Jackson. Mice were transplanted with 1.25 million cells suspended in DPBS. DPBS was used as a sham control. Briefly, 3D microtissues were collected and transferred into a sample loading tip bent to have a U-shape. The tips were connected to a PE50 tube (BD Diagnostics system, #427516), and microtissues were slowly pushed into the center of the tube using a pipetman. The PE50 tube with microtissues was then bent into U-shape and placed into a microcentrifuge tube with both the PE50 tube ends kinked and facing up. The EP tube was centrifuged at 1000 rpm for 10 seconds to pack the microtissues tightly so that the medium was located to the two ends. The PE50 tube was connected to a loading tip again. Microtissues were slowly pushed to one end of the PE50 tube using a pipetman. This operation was to remove the medium so that no medium was injected into the kidney capsule. Otherwise, the medium would wash out the injected microtissues from the kidney capsule. The right kidney of an anesthetized mouse was exposed. A small scratch on the flank of the kidney was made by a syringe 25-gauge needle, creating a nick in the kidney capsule. Saline was applied with a cotton swab to keep the kidney wet. The PE50 tube was inserted into the capsule to make a small pocket under the capsule. Microtissues were slowly pushed into the pocket. The PE50 tube was carefully retracted, and the nick was cauterized with low heat. After stopping bleeding, saline was applied, and the kidney was placed back. Details can be found in previous

publications (Szot, Koudria and Bluestone, 2007; Jofra et al>, 2018). After 18 days of transplantation surgery, $Rag1^{-/-}$ mice without BA transplantation were fed with NCD (Research diets, #D12450Ji) or HFD (Research diets, #D12492i) and labeled as $Rag1^{-/-}$ NCD and $Rag1^{-/-}$ HFD, respectively. $Rag1^{-/-}$ mice transplanted with BA microtissues were fed with HFD and labeled $Rag1^{-/-}$ HFD+BA. Wild-type (WT) mice without BA transplantation were fed with NCD or HFD and labeled as WT NCD and WT HFD.

Immunocytochemistry

Cells cultured on 2D were fixed with 4% paraformaldehyde (PFA) at room temperature for 15 min, permeabilized with 0.25% Triton X-100 for 10 min and blocked with 5% donkey serum for 1 h before incubating with primary antibodies (Table S1) in DPBS + 0.25% Triton X-100 + 5% donkey serum at 4 °C overnight. After washing, secondary antibodies (Table S1) were added and incubated at room temperature for 2 h followed by incubating with 10 mM 4',6-Diamidino-2-Phenylindole, Dihydrochloride (DAPI) for 10 min. Cells were washed with DPBS three times before imaging with a Fluorescent Microscopy (Zeiss, Germany). For 3D microtissues immunostaining, microtissues were fixed with 4% PFA at 4 °C overnight. 40 μm thick tissue sections were obtained via cryosection. The sections were washed with DPBS three times and stained as the 2D cell cultures.

For in vivo studies, mouse tissues were harvested and fixed with 4% PFA at 4 °C overnight. 5 μm thick sections were obtained via paraffin-embedding and section. The sections were deparaffined with xylene three times and rehydrated sequentially in 100%,

95%, 70%, 50% ethanol, and distilled water. For hematoxylin and eosin (H&E) staining, rehydrated sections were stained in Mayers Hematoxylin (Ricca Chemical Company, #3530-16) for 1 min, washed in distill water for 5 times, in DPBS once, and in distilled water 3 times with 1 min for each wash and stained in Eosin (Fisher, #SE23-500D) for 1 min. The sections were then dehydrated in 95% ethanol (3 times), 100% ethanol (2 times), and xylene (3 times) with 1 min for each wash before being mounted with coverslips. For immunostaining, heat-induced epitope retrieval was done on rehydrated tissue sections using the antigen retrieval buffer (Abcam, #ab93680) following the manufacturer's instruction. The sections were stained as the 2D cell cultures.

Flow Cytometry

Cell culture or microtissues were dissociated into single cells with 0.25% trypsin-EDTA. Single cells were fixed with 4% PFA and stained with primary antibodies at 4 °C overnight. After washing (three times) with 1% BSA in DPBS, secondary antibodies were added and incubated at room temperature for 2 h. Finally, cells were washed with 1% BSA in DPBS and analyzed using CytoFLEX LX (Beckman Coulter, USA). Isotype controls served for negative gating.

Serum preparation

Blood samples were collected from the mouse tail. Cells were removed via centrifugation at 3000 g for 10 min at 4 ºC. The supernatant was transferred into a new tube and centrifuged at 3000 g for 5 min at 4 ºC to collect the serum.

Mouse adipokine array and human obesity array

Mice were sacrificed. Blood was collected, and serum was isolated as described above. 100 μL serum was applied to the mouse adipokine array (R&D systems, #ARY-013) following the manufacturer's instruction. 70 μL serum was applied to the human obesity array (RayBiotech, #QAH-ADI-3-2) following the manufacturer's instructions.

Glucose tolerance test (GTT)

Mice were fasted from the morning for 16 h. Glucose (0.75 g/kg body weight) was administrated via intraperitoneal injection. Blood samples were collected to measure the glucose level at 0 (baseline), 30, 60, 90, and 120 min after injection.

Insulin tolerance test (ITT)

Mice were fasted overnight for 8 h. Insulin (Sigma, # I9278-5ML, 0.75 U/kg body weight) was administered via intraperitoneal injection. Blood samples were collected to measure the glucose level at 0 (baseline), 30, 60, and 90 min after injection.

Body composition

Mouse fat and lean mass were analyzed by Minispec LF50 (Bruker, USA).

Statistical Analysis

The data are presented as the mean ± SEM. Unpaired t-test and one-way analysis of variance (ANOVA) were used to compare two and more than two groups, respectively.

Two-way ANOVA was used to compare mice metabolic curves and arrays. $P < 0.05$ was considered statistically significant.

Results

Fabricating 3D BA microtissues.

The brown adipose progenitors (BAPs) used in this study were isolated from the superficial neck fat of a human subject and have been well characterized and documented[33]. Like the 2D differentiation, we cultured the microtissues in differentiation medium I for 3 days and then in differentiation medium II with a medium refresh every 7 days (**Figure 4.1A**). To prepare 3D BA microtissues, single BAPs were placed in microwells (Aggrewells) in the growth medium. Cells interacted, gradually contracted, and formed compact spheroids after 24 h (**Figure 4.1B**). Microtissues grew in size significantly during the differentiation (**Figure 4.1B**). For instance, microtissues with an initial diameter of 100 μm became 200 μm on day 17 (**Figure 4.1B**). The microtissue size growth can result from the cell number increase due to cell proliferation or the cell size increase, or both. Cell proliferation and size growth were observed during the differentiation of BAPs to BAs in 2D culture[34]. When the day 17 microtissues were placed in a conventional tissue culture plate, they adhered to the surface, and individual cells migrated out (**Figure 4.1C, 4.1D**). Immunostaining showed that most of the cells in the microtissues expressed the UCP-1 protein, a biomarker of mature and functional BAs (**Figure 4.2A**). The attached microtissues also expressed high level UCP-1 (**Figure 4.2B**). UCP-1 is a mitochondria

membrane protein that is critical for non-shivering thermogenesis. BAT dissipates energy in the form of heat via the UCP-1 activity[47,48].

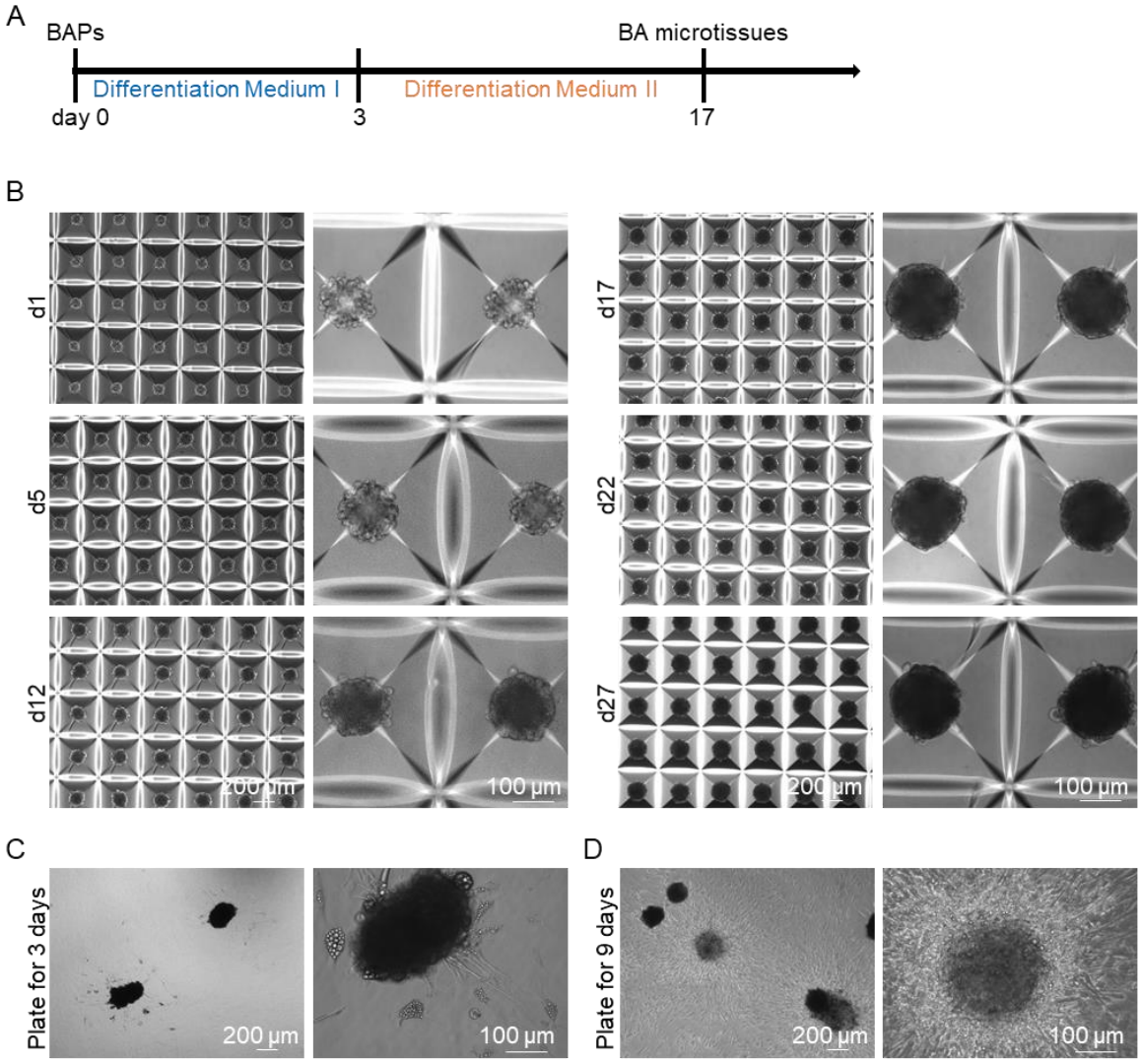

Figure 4.1. Fabricating BA microtissues. (A) BA differentiation protocol. (B) Preparing BA microtissues in microwells. Phase images day-27 BA microtissues after plating on 2D surface for 3 days (C) and 9 days (D).

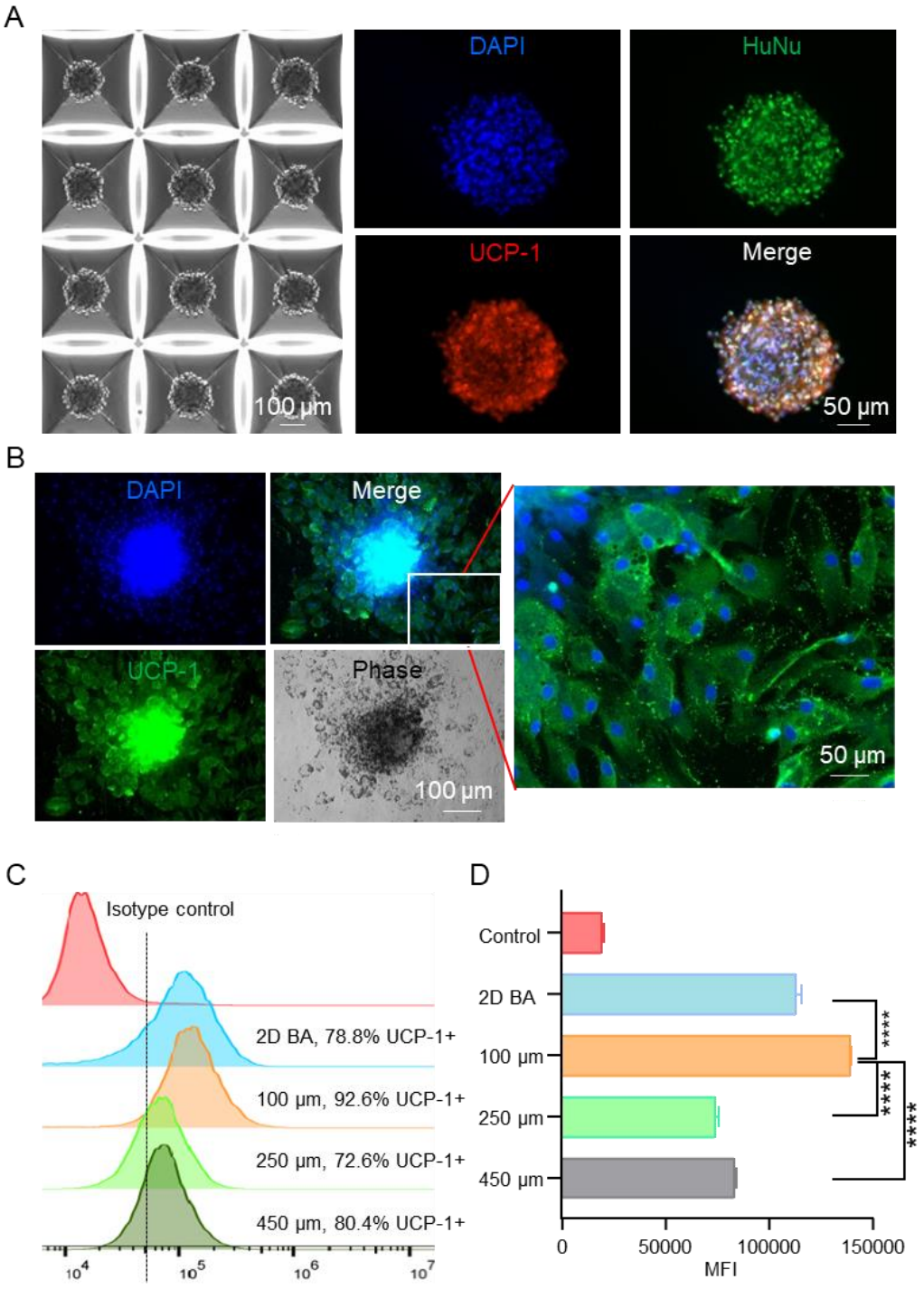

Figure 4.2. 3D culture enhanced BA differentiation. (A) 3D BA microtissues in microwells on day 17 and their immunostaining. HuNu: human nuclear antigen. (B) The day 17 BA microtissues were plated on 2D surface for 6 days and stained for UCP-1 expression. (C) Flow cytometry analysis of UCP-1 expression on day 17 for BAs prepared in 2D culture and 3D culture with varied aggregate sizes. (D) The mean fluorescent intensity (MFI) of UCP-1 as measured with flow cytometry in (C). Data are represented as mean ± SEM (n=3). ****$p < 0.0001$.

To study if the microtissue size influences the differentiation efficiency, we prepared microtissues with a diameter of 100, 250, and 450 μm (initial diameter) and differentiated them. All microtissues grew in size significantly (**Figure 4.3**). While the 100 and 250 μm microtissues maintained spherical, the 450 μm microtissues gradually became non-spherical (**Figure 4.3D**). Cell death (**Figure 4.3D**, red arrows) and fusion between microtissues (**Figure 4.3D**, blue arrows) were observed only in the 450 μm microtissues. On day 17, flow cytometry analysis showed 92.6%, 72.6%, and 80.4% of the cells in the 100, 250, and 450 μm microtissues were UCP-1 positive. For comparison, 2D culture resulted in 78.8% UCP-1 positive cells (**Figure 4.2C**). The mean fluorescent intensity (MFI) of UCP-1 intensity in 100 μm microtissues is significantly higher than in other groups (**Figure 4.2D**). The results show that a 3D microenvironment promoted brown adipogenesis and UCP-1 expression. However, a small microtissue size should be used to maximize the benefits. We used 100 μm microtissues for the rest of the study.

The cells migrated from microtissues had the classical BA characteristics (**Figure 4.4**). They expressed a high level of UCP-1 protein (**Figure 4.2A-C, 4.4D**) and had multiple small oil droplets (**Figure 4.1C, 4.4A-C**) and a high mitochondrial content (**Figure 4.4C**). In addition, they expressed the typical BA marker genes at high levels (**Figure 4.4E**).

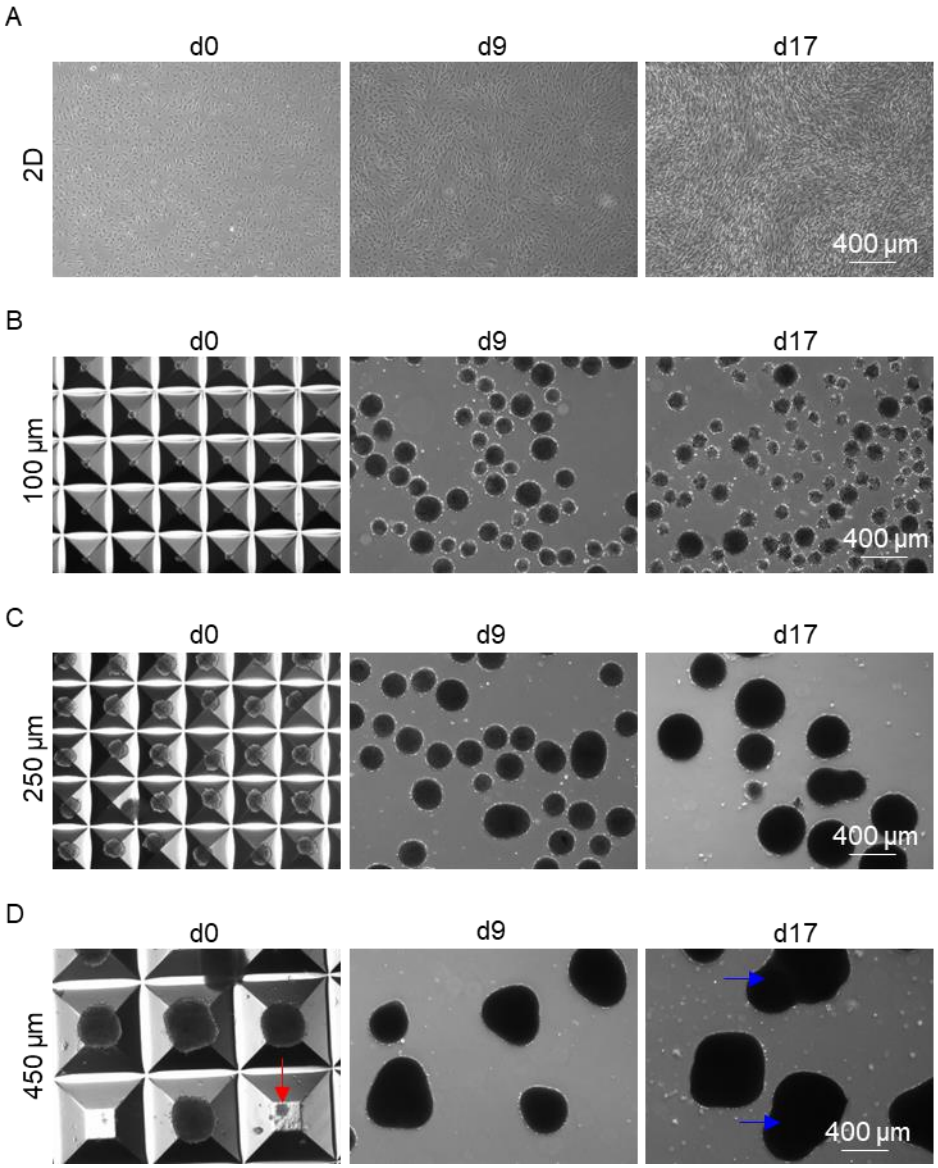

Figure 4.3. Preparing BAs in 2D culture (A) or microwells with varied aggregate sizes (B, C, D). Day 9 and Day 17 microtissues were released from microwells before imaging.

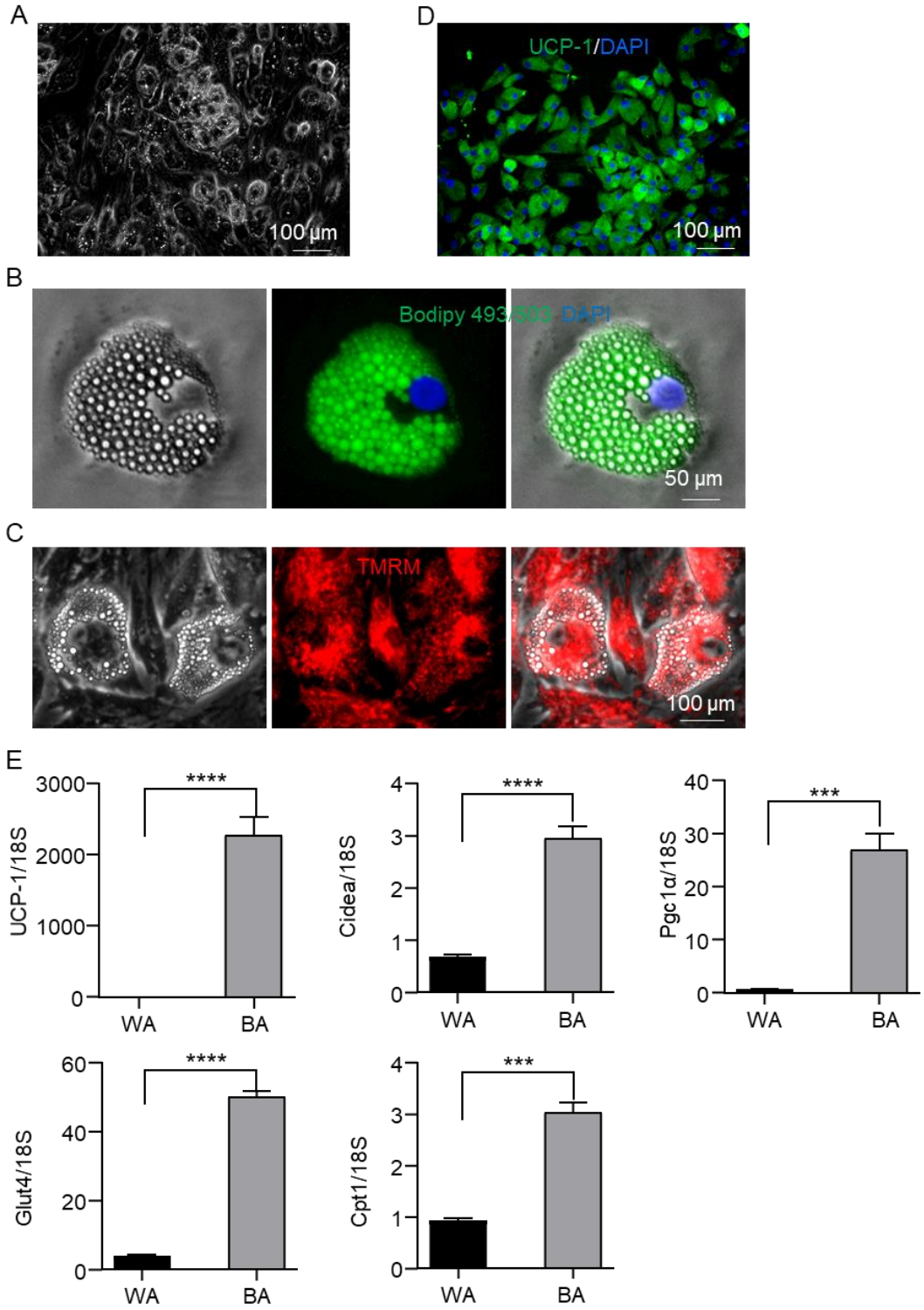

Figure 4.4. Characterization of BA microtissues. BAs prepared in 3D had typical BA phenotypes such as large numbers of small lipid droplets (A, B), abundant mitochondria (C) and UCP-1 proteins (D). They expressed BA-specific genes at high level (E). WA and BA: adipocytes differentiated from human WAPs and BAPs in microwells. TMRM: Tetramethylrhodamine, methyl ester (mitochondrial probe). Data are represented as mean ± SEM (n=3). ***p < 0.001, ****p < 0.0001 ***p < 0.001

BA microtissues survived in vivo with angiogenesis and innervation.

As said, very few BAT transplantation studies used T2DM mice. To fill the gap, we used high fat diet (HFD)-induced OB and T2DM mouse model to test the engineered BA microtissues. We selected the immune-deficient $Rag1^{-/-}$ mice as recipients since they tolerate xenogeneic and allogeneic tissues and have HFD-induced OB and metabolic disorders[49,50]. In addition, they developed diabetes when given STZ[51]. $Rag1^{-/-}$ mice fed with normal chow diet (NCD) and HFD with no microtissue transplantation were used as positive and negative controls to evaluate the microtissue efficacy. Wild type (WT) mice fed with NCD and HFD were also included to assess the difference of response to HFD between WT and $Rag1^{-/-}$ mice. HFD was initiated 18 days post-transplantation (**Figure 4.5A**). A significant number of adipose tissues was found in the kidney capsule 1 month and 5 months after transplantation (**Figure 4.5B**). H&E staining showed the dense kidney tissue and the adjacent adipose tissue with large amounts of oil droplets (**Figure 4.5B**). The oil droplets were bigger in the 5 month sample. No tumor or non-adipose tissues were found in the transplants, indicating safety of fully differentiated BAs in vivo.

The oil droplets were much bigger than those of the endogenous BAT (endoBAT) of NCD fed mice, but comparable to the endoBAT of HFD fed mice (**Figure 4.7A**), which indicates whitening of the transplanted BAs. However, a high level of UCP-1 protein was observed (**Figure 4.5C**), showing the BA function was maintained for at least 5 months. Host blood vessels grew into the transplants (**Figure 4.5D**). The vessel density was lower than the endoBAT of NCD mice but comparable to the endoBAT of HFD mice (**Figure 4.7D**). Innervation is critical for BA function. Tyrosine hydroxylase (TH+) nerves were

found in the transplants (**Figure 4.5E**), and their density was lower than this of the NCD mouse endoBAT but comparable to the density in the HFD mouse endoBAT **(Figure 4.7E**).

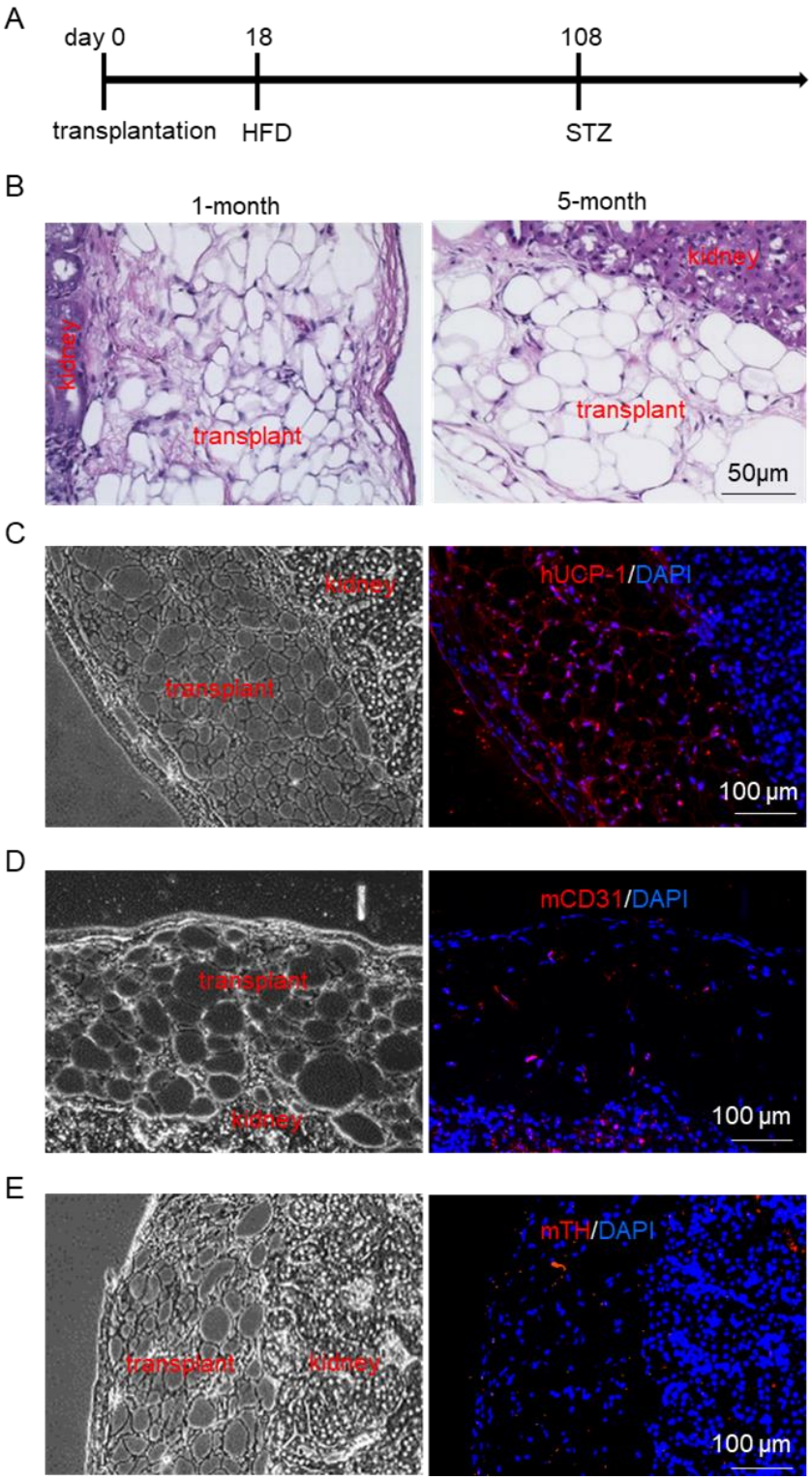

Figure 4.5. BA microtissues survived in vivo with angiogenesis and innervation. (A) The transplantation protocol. (B) H&E staining of 1-month and 5-month transplant. The transplant and adjacent kidney tissue are labelled. Immunostaining of the 5-month transplant and adjacent kidney tissue with human UCP1 (hUCP1) (C), mouse CD31 (mCD31) (D) , and mouse tyrosine hydroxylase (mTH) (E) .

BA microtissues alleviated obesity and diabetes.

We regularly measured the body weight, fat and lean mass, plasma glucose level, glucose tolerance, and insulin sensitivity (**Figure 4.6**). To mimic the β cell dysfunction of T2DM, we injected low-dose STZ (90 mg/kg) after 3-month HFD. The bodyweight drops and the fasting glucose level rise after the STZ injection indicated the progression of T2DM (**Figure 4.6A, 4.6D**). There was no significant difference in total diet intake between the HFD groups. Under HFD, both WT and $Rag1^{-/-}$ mice developed OB (**Figure 4.6A**) and grew large fat masses (**Figure 4.6B, 4.6C**). We found $Rag1^{-/-}$ mice were slightly more prone to HFD-induced OB and metabolic disorders but were suitable for our studies. The transplant significantly reduced the body weight gain, fat content, and fasting glucose level while increasing insulin sensitivity and glucose tolerance (**Figure 4.6**).

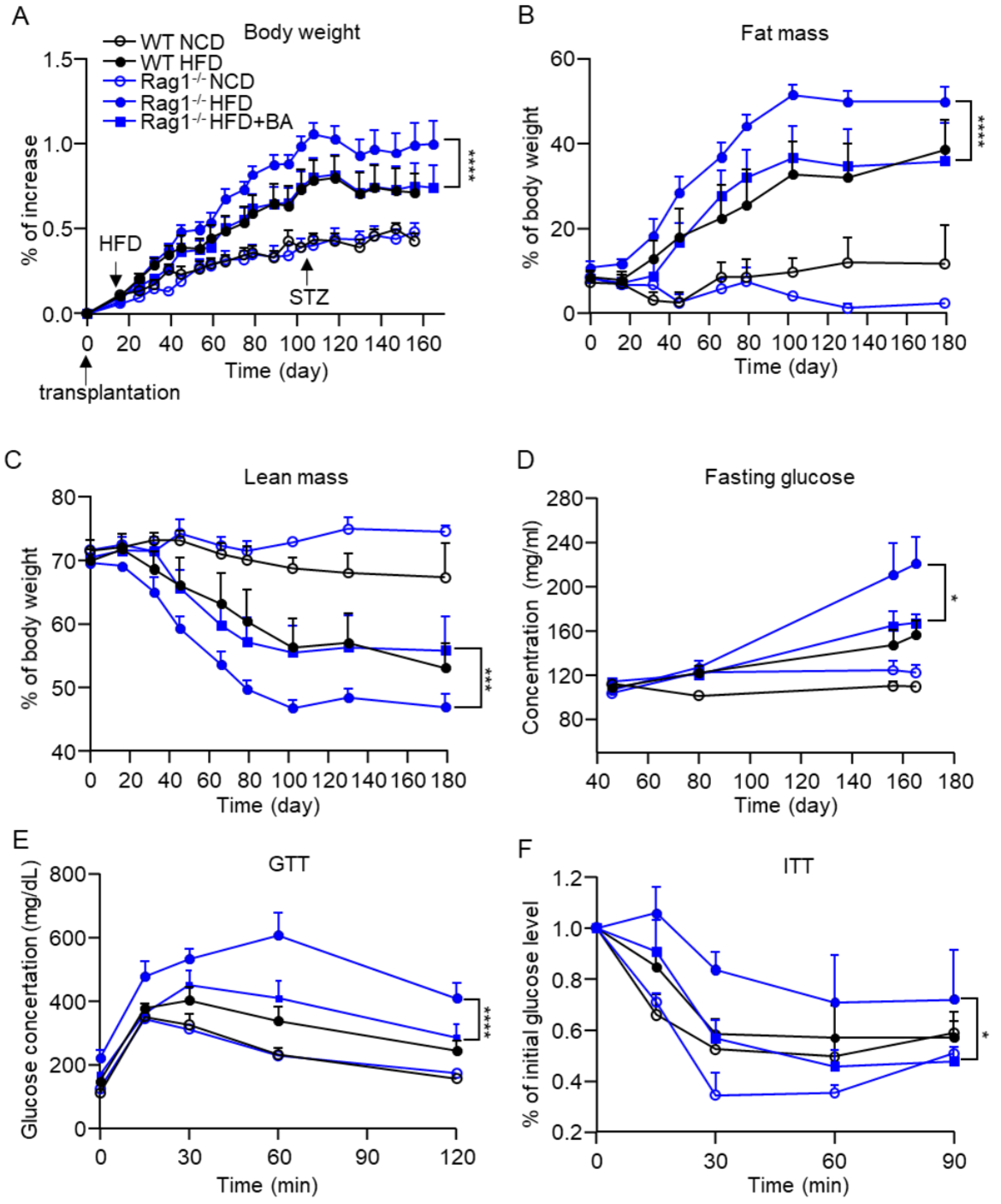

Figure 4.6. BA microtissues alleviated obesity and diabetes. (A) Body weight gain, (B) % fat mass, (C) % lean mass, (D) fasting glucose level, (E) GTT (day 150), and (F) ITT (day 170). WT: wild type mouse; Rag1$^{-/-}$: Rag1 knock-out mice; NCD: normal chow diet; HFD: high fat diet. Data are represented as mean ± SEM (n=6). *p < 0.05, ***p < 0.001, ****p < 0.0001.

BA microtissues prevented the whitening of endogenous BATs.

The endoBAT was whitened in Rag1$^{-/-}$ mice fed with HFD, as shown by an increase of adipocyte size and oil droplets (**Figure 4.7A-C**), and a reduction of the mUCP-1 protein expression (**Figure 4.7D**), blood vessel density (**Figure 4.7D, 4.7E**) and TH+ nerve density (**Figure 4.7E**). The transplanted BA microtissues almost wholly prevented the whitening of endoBAT (**Figure 4.7A-E**). HFD mice with BA microtissues had similar BA morphology, blood vessel, and nerve densities to the NCD mice.

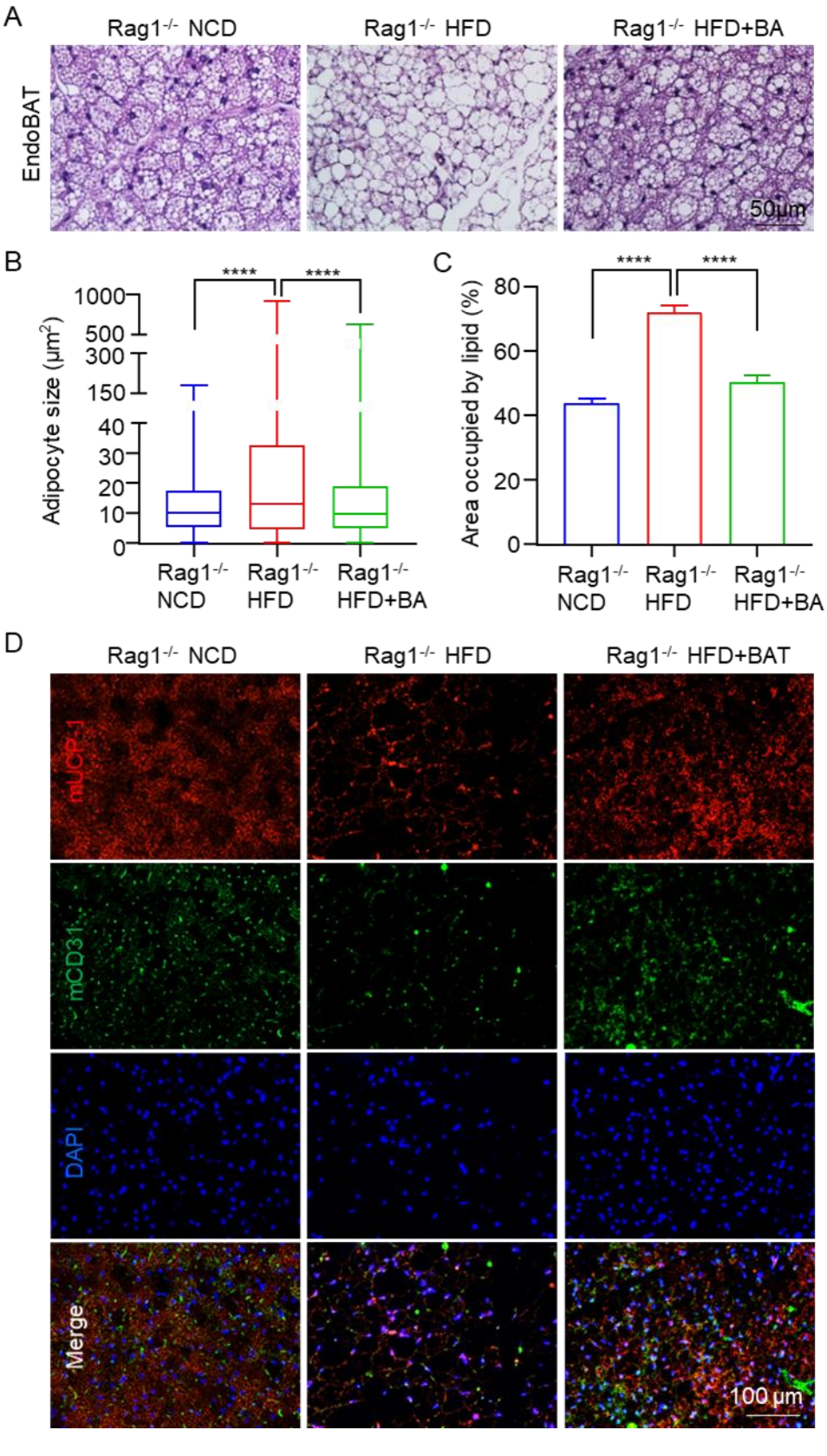
A
Rag1-/- NCD
Rag1-/- HFD
Rag1-/- HFD+BA
EndoBAT
50μm
B
Adipocyte size (μm2)
1000
500
300
150
40
30
20
10
0
****
****
Rag1-/- NCD
Rag1-/- HFD
Rag1-/- HFD+BA
C
Area occupied by lipid (%)
80
60
40
20
0
****
****
Rag1-/- NCD
Rag1-/- HFD
Rag1-/- HFD+BA
D
Rag1-/- NCD
Rag1-/- HFD
Rag1-/- HFD+BAT
mUCP-1
mCD31
DAPI
Merge
100 μm

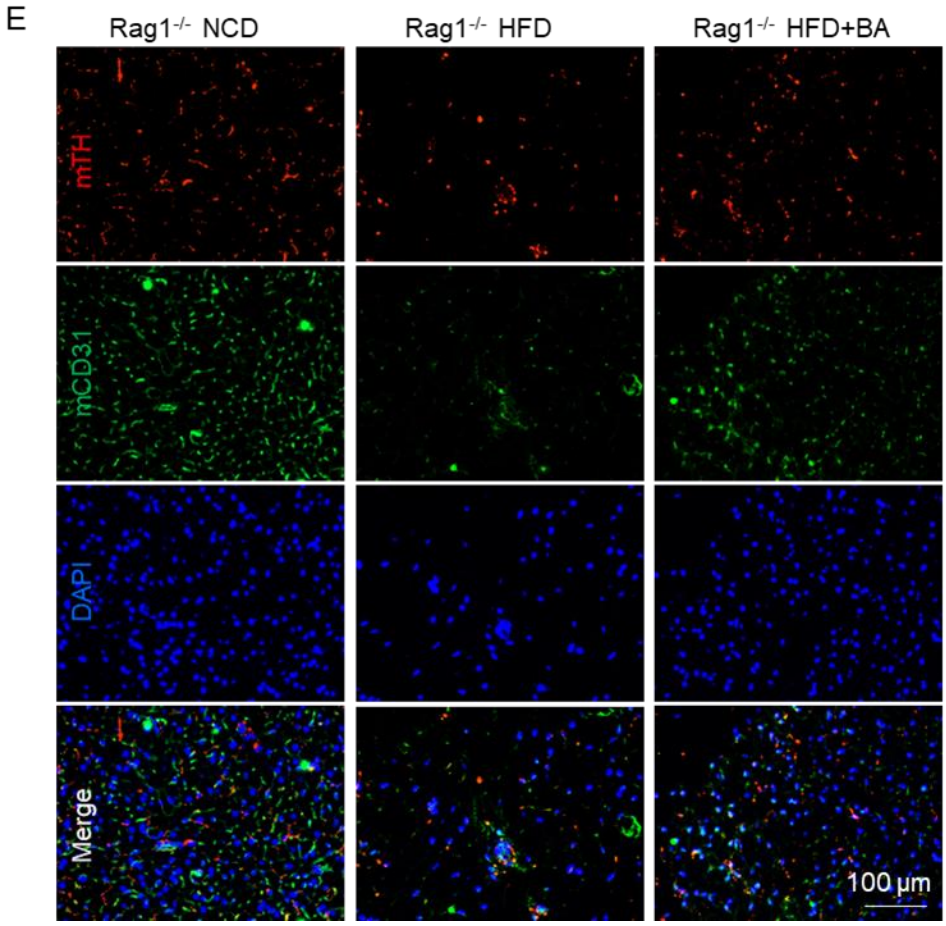

Figure 4.7. BA microtissues protected endogenous BAT (endoBAT). (A) H&E staining of endoBAT. BA size (B) and area (C) in endoBAT. (D) Mouse UCP-1 and CD31 expression in endoBAT. (E) Mouse TH and CD31 expression in endoBAT. Data are represented as mean ± SEM (n=6). ****$p < 0.0001$.

BA microtissues alleviated endogenous WAT hypertrophy and liver steatosis.

The adipocyte and oil droplet size of subcutaneous WAT (scWAT) was increased by the HFD. BA microtissues significantly reduced the adipocyte and oil droplet size (**Figure 4.8A-C**). CD31 staining showed fewer blood vessels in HFD fed mice. BA microtissues increased the blood vessel density in HFD fed mice (**Figure 4.8D**). The liver fat content was significantly increased in HFD mice but was almost normalized by BA microtissues (**Figure 4.8E**). These results showed that the transplanted microtissues had a profound effect on multiple organs.

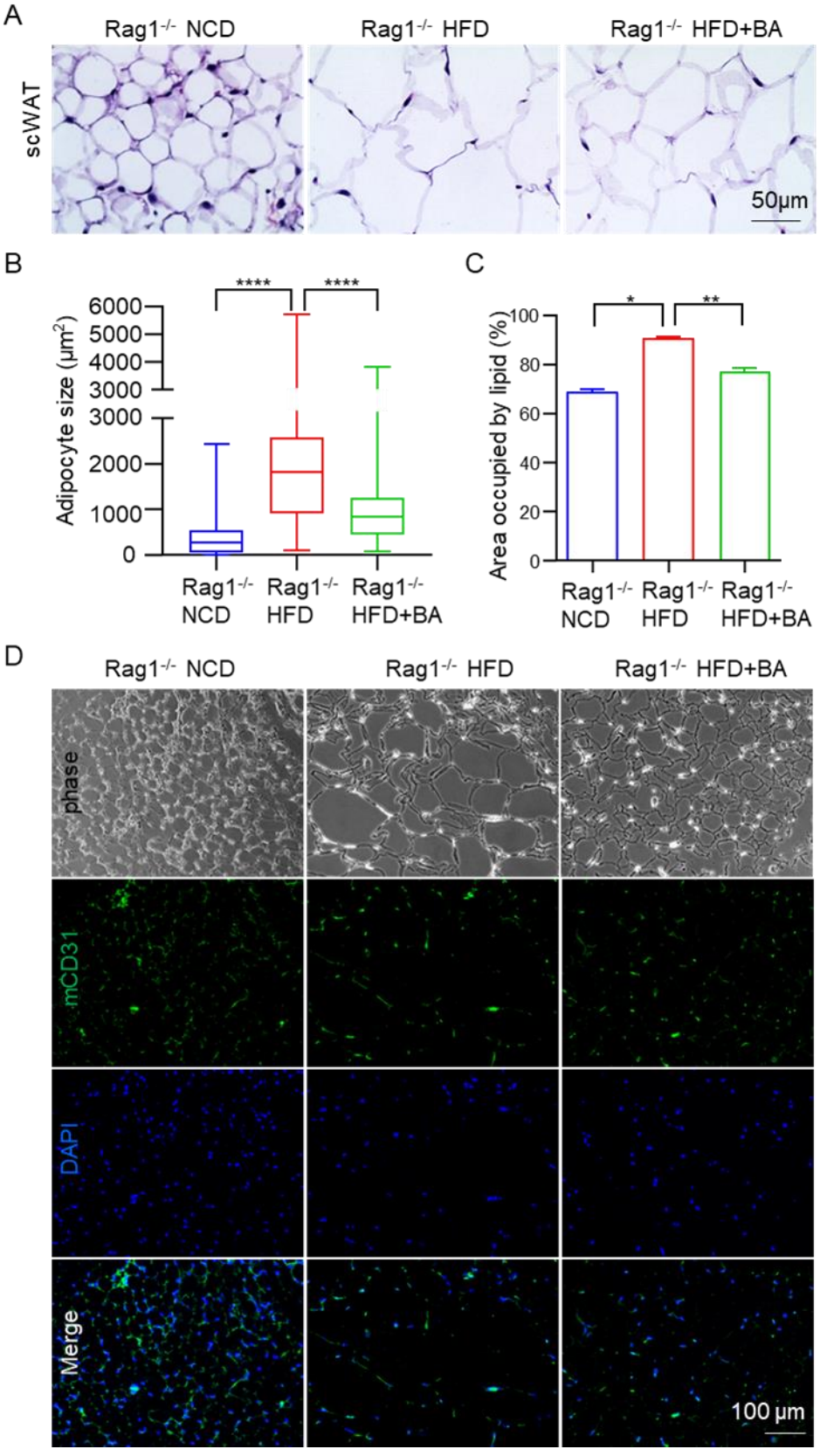
A
Rag1-/- NCD
Rag1-/- HFD
Rag1-/- HFD+BA
scWAT
50μm
B
Adipocyte size (μm2)
6000
5000
4000
3000
3000
2000
1000
0
****
****
Rag1-/- NCD
Rag1-/- HFD
Rag1-/- HFD+BA
C
Area occupied by lipid (%)
100
80
60
40
20
0
*
**
Rag1-/- NCD
Rag1-/- HFD
Rag1-/- HFD+BA
D
Rag1-/- NCD
Rag1-/- HFD
Rag1-/- HFD+BA
phase
mCD31
DAPI
Merge
100 μm

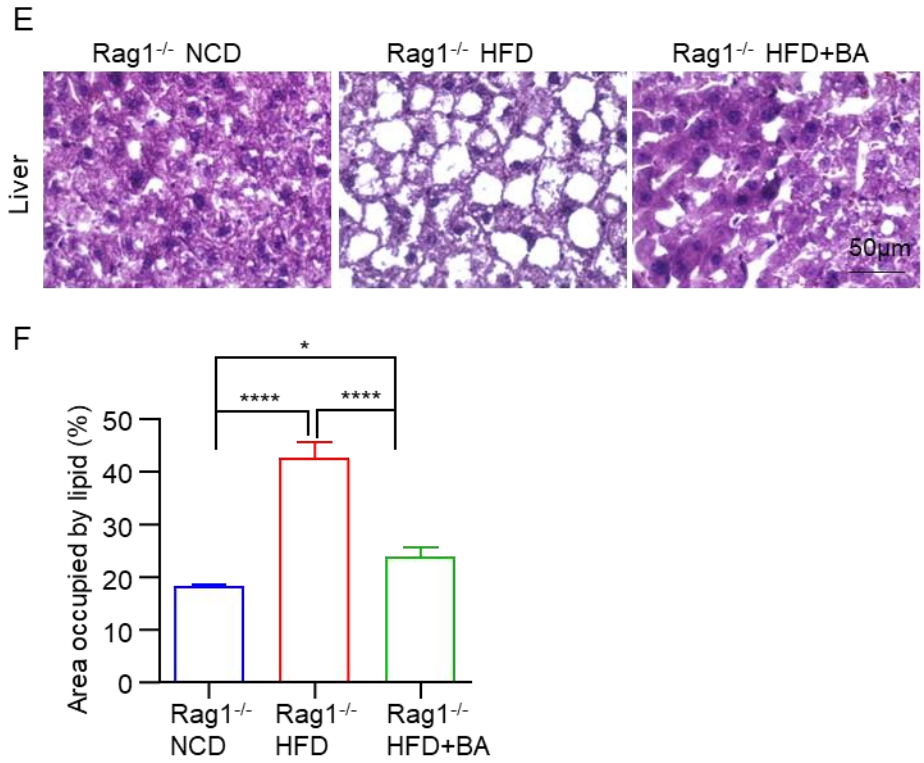

Figure 4.8. BA microtissues reduced endogenous WAT hypertrophy and liver steatosis. (A) H&E staining of mouse subcutaneous white adipose tissue (scWAT). (B, C) Adipose size and area in scWAT. (D) Mouse CD31 expression in scWAT. (E) H&E staining of mouse liver. (F) Adipose area in liver. Data are represented as mean ± SEM (n=6). *$p < 0.05$, **$p < 0.01$, ****$p < 0.0001$.

BA microtissues secreted soluble factors and modulated endogenous adipokines.

We used a Human Obesity Antibody Array to measure human protein factors in the blood. We found that the concentrations of human adiponectin, chemerin, and TGF-β1 in mice with transplants were significantly higher than background (**Figure 4.9A**), indicating the transplanted BAs were secreting soluble factors. Research has shown that adiponectin secreted by white and brown adipocytes has a protective role in obesity-associated metabolic and cardiovascular diseases. Adiponectin influences multiple tissues such as the liver, skeletal muscle, and vascular system. Adiponectin can increase insulin sensitivity[52,53], suppress inflammation, and reduce atherosclerosis[54–56]. Plasma adiponectin level is negatively correlated with obesity, and adiponectin deficiency enhances HFD induced insulin resistance[57]. Chemerin plays a positive role in the metabolic health[58,59]. TGF-β1 is a mediator of insulin resistance in metabolic disease[60,61].

We also used a Mouse Adipokine Antibody Array to measure 38 obesity-related mouse molecules. The levels of Adiponectin, ANGPT-L3, C-reactive protein, ICAM-1, IGFBP-3, IGFBP-5, IGFBP-6, Lipocalin-2, and Pentraxion2 were significantly reduced, and the IGF-1 concentration was increased by the HFD (**Figure 4.9B, 4.9C**). All of these molecules were normalized by the transplanted BA microtissues (**Figure 4.9C**). Thus, the transplanted microtissues had a significant effect on the endogenous adipokines.

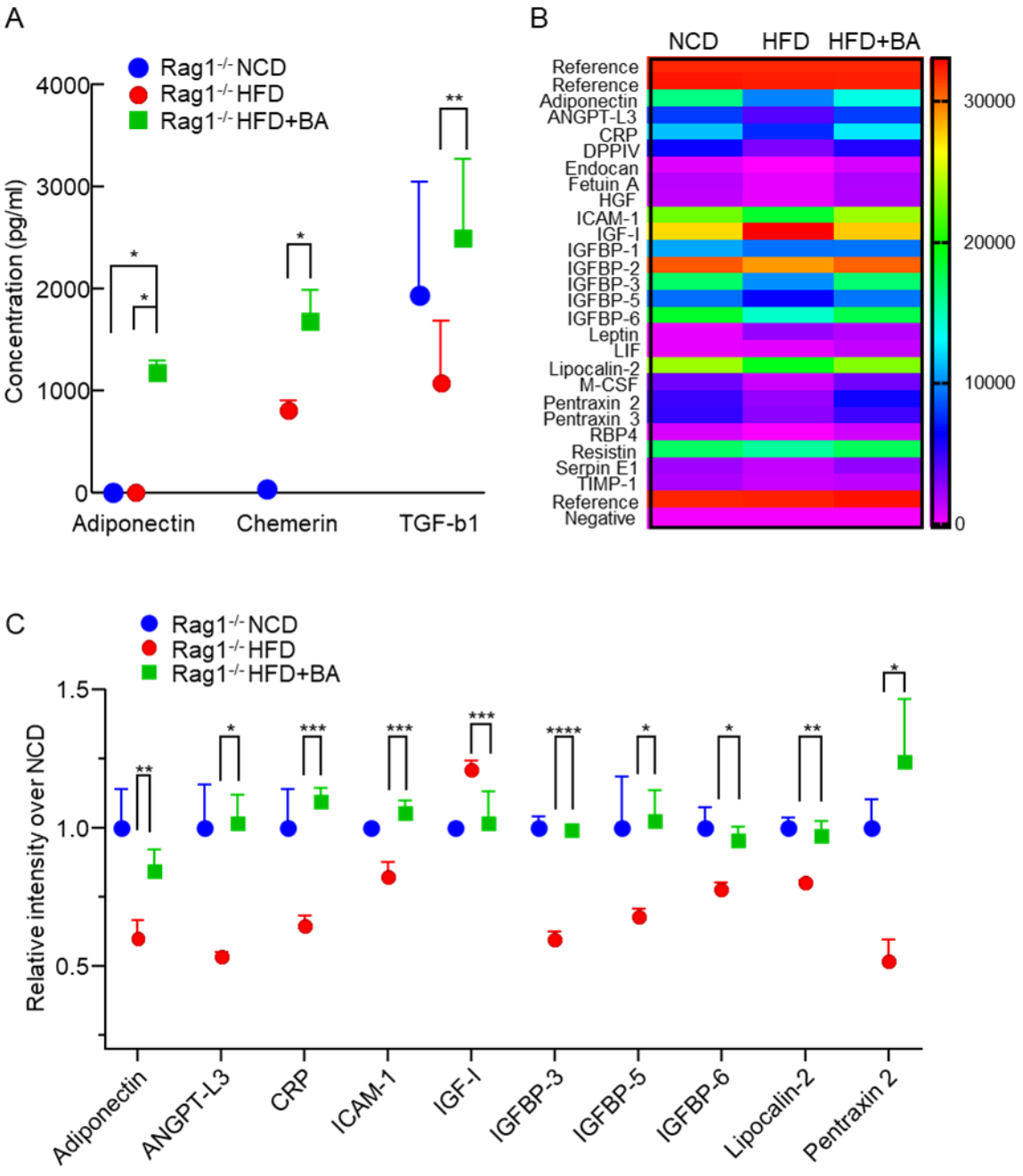

Figure 4.9. BA microtissues secreted human protein factors and modulated endogenous adipokines. (A) Protein factors in mouse plasma detected using human obesity antibody array. (B, C) Heatmap and quantification of adipokines in mouse plasma detected using mouse adipokine antibody array. Data are represented as mean ± SEM (n=3). *p < 0.05, **p < 0.01, ***p < 0.001, ****p < 0.0001.

Scale up BA microtissues production.

All the above experiments used microwells to prepare microtissues. However, microwells are unsuitable for producing microtissues at large scales, which are needed for future extensive animal studies, drug screens, and clinical applications. Previously, our lab used 3D suspension culture (e.g., shaking plates, spinning flasks, stirred tank bioreactors) to prepare human pluripotent stem cells at large scales[36–40]. We also pioneered in culturing stem cells at high density in thermoreversible PNIPAAm-PEG hydrogels[36,40–44,62]. We found that BA microtissues could be prepared in both systems (**Figure 4.10**). Large tissue aggregates formed via fusion of multiple microtissues were found in shaking flasks (**Figure 4.10A**), while microtissues in PNIPAAm-PEG hydrogels were uniform (**Figure 4.10B**). BAs from both systems expressed a high level of UCP-1 protein (**Figure 4.10C)**. Thus, both systems can be used to scale up the microtissues production.

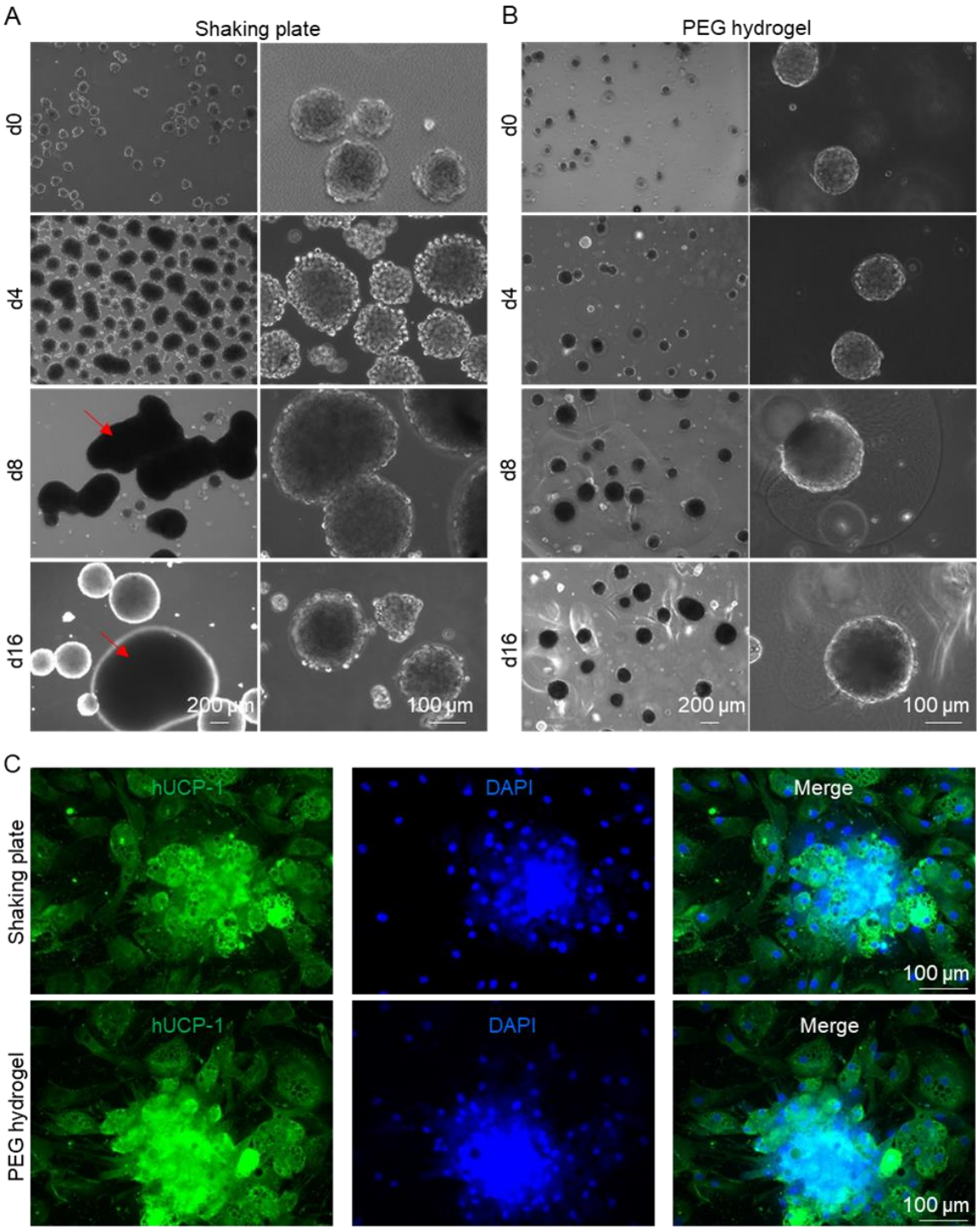

Figure 4.10. Scaling up BA microtissue production. Preparing BA microtissues in shaking plates (A) and PEG hydrogel (B). (C)Immunostaining of day 17 BA microtissues prepared in shaking plates and PEG hydrogel. Microtissues were plated on 2D surface for 6 days before staining.

Preserving BA microtissues.

Lastly, we evaluated if BA microtissues could be preserved. Microtissues preserved in cell culture medium at room temperature for 24 h (**Figure 4.11B**) had similar viability to the fresh sample (**Figure 4.11A**). Microtissues could also be cryopreserved in liquid nitrogen for the long term without significantly sacrificing cell viability (**Figure 4.11C**).

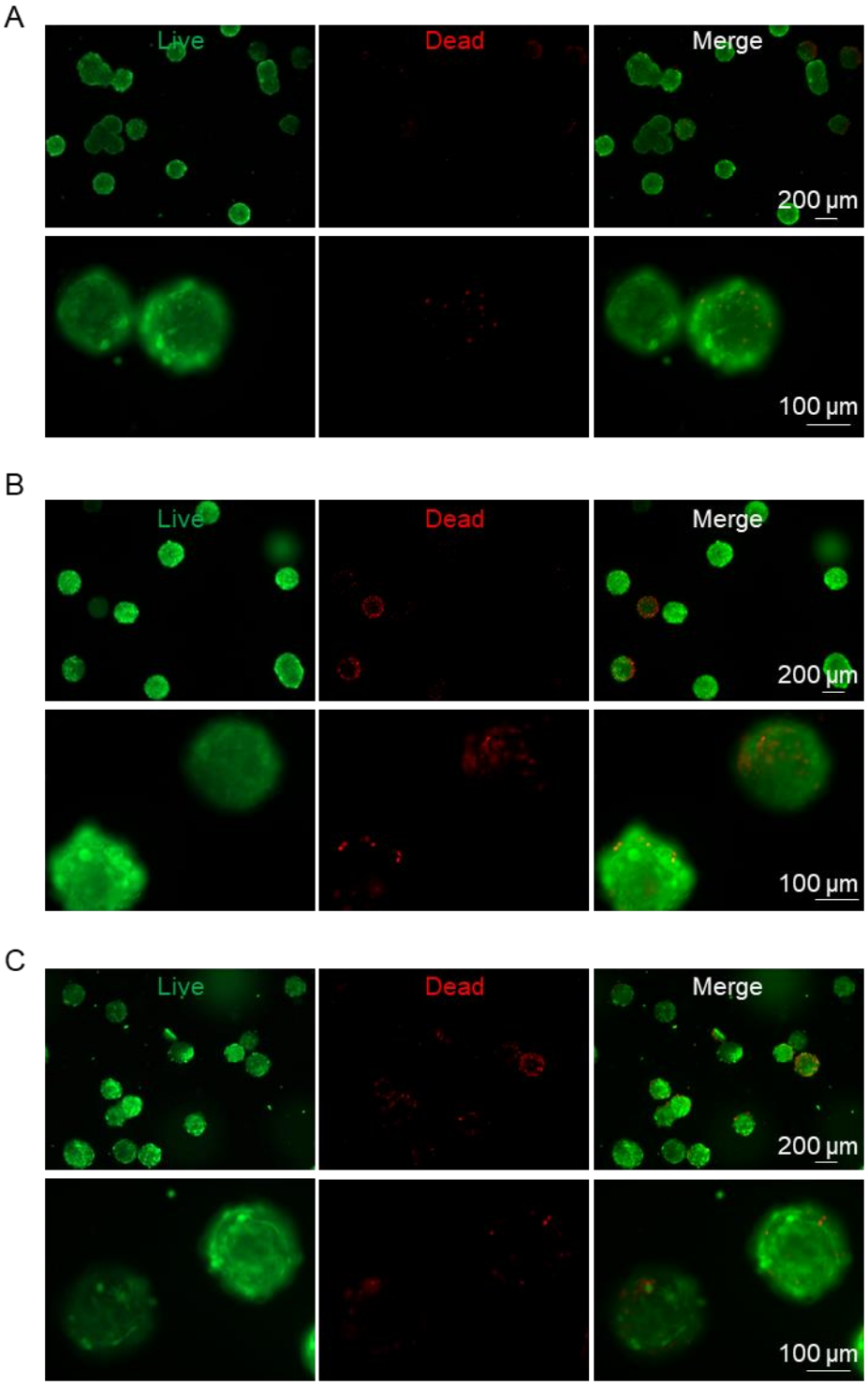

Figure 4.11. Preserving BA microtissues. Live/dead cell staining of day 27 fresh BA microtissues (A) or stored at room temperature for 24 h (B) or stored in liquid nitrogen and recovered (C).

Table 4.1, Antibodies used in chapter 4.

Antibody	Supplier	Catalog. No	Host species	Dilution
Anti-UCP1	abcam	ab155117	Rabbit	1:50
Tyrosine Hydroxylase (TH)	Fisher scientific	AB152MI	Rabbit	1:50
CD31	abcam	ab24590	Mouse	1:250
Anti-UCP1	abcam	ab23841	Rabbit	1:250
Anti-Human Nuclear Antigen antibody [235-1]	abcam	ab191181	Mouse	1:100
Secondary Antibody	Thermo Fisher	A-21202	Donkey	1:500
Secondary Antibody	Thermo Fisher	A-21207	Donkey	1:500
Secondary Antibody	Jackson Immuno Research Labs	715585150	Donkey	1:500
Secondary Antibody	Jackson Immuno Research Labs	711545152	Donkey	1:500

Table 4.2. One-way ANOVA multiple comparisons test results of mean UCP-1 intensities for day 17 BA in Figure **4.2D**. Data are represented as mean ± SEM (n=3). *p < 0.05 , ****p < 0.0001.

	Control	2D BA	100 µm	250 µm	450 µm
Control					
2D BA	****				
100 µm	****	****			
250 µm	****	****	****		
450 µm	****	****	****	*	

Table 4.3. Two-way ANOVA multiple comparisons test results of body weight gain in **Figure 4.6**.

Tukey's multiple comparisons test (weight)	WT NCD	WT HFD	Rag1$^{-/-}$NCD	Rag1$^{-/-}$HFD	Rag1$^{-/-}$HFD+BA
WT NCD					
WT HFD	****				
Rag1$^{-/-}$NCD	ns	****			
Rag1$^{-/-}$HFD	****	****	****		
Rag1$^{-/-}$HFD+BAT	****	ns	****	****	

Table 4.4. Two-way ANOVA multiple comparisons test results of body fat mass in **Figure 4.6**.

Tukey's multiple comparisons test (fat mass)	WT NCD	WT HFD	Rag1$^{-/-}$NCD	Rag1$^{-/-}$HFD	Rag1$^{-/-}$HFD+BA
WT NCD					
WT HFD	****				
Rag1$^{-/-}$NCD	ns	****			
Rag1$^{-/-}$HFD	****	****	****		
Rag1$^{-/-}$HFD+BAT	****	ns	****	****	

Table 4.5. Two-way ANOVA multiple comparisons test results of body lean mass in **Figure 4.6**.

Tukey's multiple comparisons test (lean mass)	WT NCD	WT HFD	Rag1$^{-/-}$NCD	Rag1$^{-/-}$HFD	Rag1$^{-/-}$HFD+BA
WT NCD					
WT HFD	****				
Rag1$^{-/-}$NCD	ns	****			
Rag1$^{-/-}$HFD	****	***	****		
Rag1$^{-/-}$HFD+BAT	****	ns	****	***	

Table 4.6. Two-way ANOVA multiple comparisons test results of fasting glucose in **Figure 4.6**.

Tukey's multiple comparisons test (fasting glucose)	WT NCD	WT HFD	Rag1$^{-/-}$NCD	Rag1$^{-/-}$HFD	Rag1$^{-/-}$HFD+BA
WT NCD					
WT HFD	ns				
Rag1$^{-/-}$NCD	ns	ns			
Rag1$^{-/-}$HFD	****	**	****		
Rag1$^{-/-}$HFD+BAT	**	ns	ns	*	

Table 4.7. Two-way ANOVA multiple comparisons test results of GTT in **Figure 4.6**.

Tukey's multiple comparisons test (GTT)	WT NCD	WT HFD	Rag1$^{-/-}$NCD	Rag1$^{-/-}$HFD	Rag1$^{-/-}$HFD+BA
WT NCD					
WT HFD	ns				
Rag1$^{-/-}$NCD	ns	ns			
Rag1$^{-/-}$HFD	****	****	****		
Rag1$^{-/-}$HFD+BAT	**	ns	ns	****	

Table 4.8. Two-way ANOVA multiple comparisons test results of ITT in **Figure 4.6**.

Tukey's multiple comparisons test (ITT)	WT NCD	WT HFD	Rag1$^{-/-}$NCD	Rag1$^{-/-}$HFD	Rag1$^{-/-}$HFD+BA
WT NCD					
WT HFD	ns				
Rag1$^{-/-}$NCD	ns	ns			
Rag1$^{-/-}$HFD	*	ns	***		
Rag1$^{-/-}$HFD+BAT	ns	ns	ns	*	

Table 4.9. Two-way ANOVA multiple comparisons test results of mouse adipokine antibody array in **Figure 4.9C**.

	$Rag1^{-/-}$ NCD vs. $Rag1^{-/-}$ HFD	$Rag1^{-/-}$ NCD vs. $Rag1^{-/-}$ HFD+BA	$Rag1^{-/-}$ HFD vs. $Rag1^{-/-}$ HFD+BA
Adiponectin	****	ns	**
ANGPT-L3	*	ns	*
C-Reactive Protein	*	ns	***
ICAM-1	*	ns	***
IGF-I	***	ns	***
IGFBP-3	****	ns	****
IGFBP-5	ns	ns	*
IGFBP-6	*	ns	*
Lipocalin-2	**	ns	**
Pentraxin 2	ns	ns	*

Discussion

Our study showed that human BAPs could be differentiated into mature BAs in 3D to prepare injectable BA microtissues (**Figure 4.1, 4.2, 4.3**). The 3D culture promoted BA differentiation and UCP-1 protein expression. BA microtissues could survive in vivo for the long term with angiogenesis and innervation (**Figure 4.5**). They alleviated the body weight and fat gain and improved glucose tolerance and insulin sensitivity significantly in HFD-induced OB and diabetic mice (**Figure 4.6**). The transplanted BA microtissues impacted multiple tissues such as endogenous BAT, WAT, and liver (**Figure 4.7, 4.8**). In addition, they secreted protein factors and influenced the secretion of endogenous adipokines (**Figure 4.9**). These microtissues could be produced using the scalable 3D suspension culture or in a PEG hydrogel (**Figure 4.10**) and could be cryopreserved and shipped at room temperature (**Figure 4.11**). To our best knowledge, this is the first report on engineering human BA microtissues and showing their safety and efficacy in OB and T2DM mice. The findings that 3D culture promotes BA differentiation and the microtissue size affects the differentiation are all new.

To date, most BAT transplantation studies used mouse BATs. There is a need to study if human BAT can manage OB and its associated metabolic disorders. The Tseng group isolated and immortalized human BAPs and demonstrated that these cells could differentiate into mature BAs in vivo and reduce the HFD-induced OB and metabolic symptoms[32,33]. They transplanted proliferating BAPs instead of mature BAs that have exited the cell cycle. The possible reason is that BAPs have a better survival rate in vivo. A recent study showed that about 12.1% of immortalized mouse BAPs survived in SCID

mice 7 days after transplantation with Matrigel, while only 2.7% of mature BA (differentiated from BAPs in vitro) were live after 7 days using the same transplantation procedure[18]. Consequently, only BAPs showed an efficacy in vivo[18]. However, there are potential problems with using BAPs. First, the differentiation efficiency in vivo is typically low[18]. Second, proliferating cells have a higher tumorigenic risk, especially for immortalized cells. Transplanting fully differentiated BAs has advantages in that they can be prepared in vitro at high purity (e.g., ~93% in this study) (**Figure 4.2**). They are less likely to have uncontrolled growth in vivo. However, approaches must be developed to improve their survival rate in vivo and avoid cell death during the harvest in vitro, as found in our preliminary studies.

Prior studies showed transplanting mouse BATs prevented/reversed OB and its associated metabolic disorders. It should be noted that only transplanting intact 3D BAT, not dissociated single BAs, achieved long-term survival and function[17–20], indicating that 3D BAT, not single BAs, should be used as therapeutics in the future. Researchers typically inject cultured BAPs with Matrigel to mimic a 3D tissue. Matrigel can both restrict the cells at the transplantation size and enhance their survival[18]. However, Matrigel is extracted from mouse tumor tissue and is not chemically defined, and not compatible with clinical applications. Our preliminary study showed that a large percentage of mature BAs died during the harvest process, suggesting that single BAs are unsuitable for transplantation. Our engineered BA microtissues are injectable, do not need extra matrix and dissociation, thus addressing all these problems.

Interestingly, we found that the microtissue size influenced the BA differentiation

efficiency significantly. The optimal diameter is about 100 μm (initial diameter). BAs have a high demand for glucose, oxygen, and nutrients to meet their high metabolic activities. BAs have a high demand for glucose, oxygen, and nutrients to meet their high metabolic activities[18,63–67]. Nutrients are transported in these microtissues mainly through diffusion. Therefore, cells at the center of large microtissues may not have a sufficient supply of nutrients, negatively affecting the differentiation process. A second possible cause is that cells secrete autocrine or/and paracrine factors are important to BA differentiation. The microtissue diameter influences the concentrations and gradients of these factors. The exact reason should be made clear in future studies.

We demonstrated that the production of BA microtissues could be scaled up using the 3D suspension culture or a 3D thermoreversible hydrogel matrix. A limitation with the 3D suspension culturing is that the microtissues are heterogeneous in size (**Figure 4.10A**). Using the thermoreversible hydrogel matrix can produce homogenous microtissues in size (**Figure 4.10B**). However, the matrix is expensive. Our group recently developed a novel microbioreactor termed AlgTubes, in which cells are cultured in alginate hydrogel microtubes[37,38,68–73]. AlgTubes are scalable and have low cost. The cell aggregate size can be precisely controlled by the hydrogel tubes. AlgTubes can produce up to $5x10^8$ cells per mL of culture volume, about 200 times more than the 3D suspension culture. Future studies can apply AlgTubes to produce fibrous BA microtissues with uniform and precise size at high density.

BAT is among the most vascularized tissues in the body, averaging ~1.2 capillaries per BA (versus only ~0.4 capillaries per white adipocyte) [63–67]. A substantial blood supply

is required to provide glucose, fatty acids, nutrients, and oxygen to fuel thermogenesis and rapidly distribute heat throughout the body [74]. Vascular cells also produce soluble and insoluble factors critical for BA functions and homeostasis; conversely, BAs produce a range of growth factors and cytokines that collectively modulate vascular growth, survival, remodeling, regression, and blood perfusion [65,67,75]. In obese mice, the capillary density in BAT decreases significantly (i.e., ~0.5 capillaries per BA) (**Figure 4.7**), resulting in hypoxia and BAT degeneration[66]. Our results showed that transplanted BA microtissues prevented the whitening of endogenous BAT (**Figure 4.7**), which may contribute to the improvement of glucose and insulin homeostasis. In addition, we showed transplanted BAs secreted human adipokines (**Figure 4.9A**) and altered the expression levels of many endogenous adipokines (**Fig 4.9B, 4.9C**). Thus, the transplanted microtissues function at least partially via the endocrine mechanism.

We found that the transplanted microtissues gradually became white adipocyte-like in morphology (**Figure 4.5B**), although UCP-1 proteins are still expressed at a high level (**Figure 4.5C**). A reason for this whitening is the insufficient vascularization in the transplant. This agrees well with literature findings that the transplants had fewer blood vessels than endogenous BAT [18,32]. Consequently, BAs gradually decreased UCP-1 expression and became WAT-like features (i.e., whitening). There are two potential ways to address this problem. First, as shown in a published study[18], supplementing vascular endothelial growth factor (VEGF) to the transplant can significantly improve its engraftment, angiogenesis, and function. Second, endothelial cells can be included in the BA microtissues. As stated in the above paragraph, endothelial cells or vasculature are

indispensable for BAT in vivo.

We used immortalized BAPs to prepare mature BA microtissues. No tumor or abnormal tissue growth was observed (**Figure 4.5**), indicating fully differentiated BAs are safe in vivo. Thus, it is applicable to isolate and immortalize BAPs from a patient and expand them to prepare BA microtissues for personalized BA augmentation therapy. An alternative approach is to prepare induced pluripotent stem cells (hiPSCs) for a patient. hiPSCs can be generated by reprogramming somatic cells[76–78]. They have unlimited proliferation capability and can be differentiated into all types of somatic cells. Additionally, the transplant's immune rejection can be avoided by preparing BAT from personalized hiPSCs[79,80]. Recent clinical studies showed autologous hiPSCs-derived dopaminergic neurons, and retinal cells were safe and effective in treating Parkinson's[81] and macular degeneration[80], respectively, indicating the coming of the hiPSCs-based personalized medicine era. Alternatively, universal hiPSCs can be engineered, for instance, via inactivating major histocompatibility complex (MHC) class I and II genes and overexpressing CD47 or/and PD-L1[81–84]. The derivatives of universal hiPSCs are hypoimmunogenic and can be prepared at large scales as "off-the-shelf" allogeneic products. hiPSCs have been successfully differentiated into BAs that are metabolically active *in vitro* and in mice models[35,85–90]. Therefore, future studies can explore using hiPSCs to prepare personalized BA microtissues.

Conclusion

In summary, our study showed that 3D BA microtissues could be fabricated at large

scales, cryopreserved for the long term, and delivered via injection. BAs in the microtissues had higher purity, and higher UCP-1 protein expression than BAs prepared via 2D culture. In addition, 3D BA microtissues had good in vivo survival and tissue integration and had no uncontrolled tissue overgrowth. Furthermore, they showed good efficacy in preventing OB and T2DM with a very low dosage compared to literature studies. Thus, our results show engineered 3D BA microtissues are promising anti-OB/T2DM therapeutics. They have considerable advantages over dissociated BAs or BAPs for future clinical applications in terms of product scalability, storage, purity, quality, and in vivo safety, dosage, survival, integration, and efficacy.

References

1. Chan, M. Obesity and diabetes: the slow-motion disaster. Keynote address at the 47th meeting of the National Academy of Medicine. *World Health Organization* 1–7 (2016).

2. Leitner, D. R. *et al.* Obesity and type 2 diabetes: Two diseases with a need for combined treatment strategies - EASO can lead the way. *Obes. Facts* **10**, 483–492 (2017).

3. Vijgen, G. H. E. J. *et al.* Brown adipose tissue in morbidly obese subjects. *PLoS One* **6**, 2–7 (2011).

4. Saito, M. *et al.* High incidence of metabolically active brown adipose tissue in healthy adult humans: Effects of cold exposure and adiposity. *Diabetes* **58**, 1526–1531 (2009).

5. Becher, T. *et al.* Brown adipose tissue is associated with cardiometabolic health. *Nat. Med.* **27**, 58–65 (2021).

6. O'Mara, A. E. *et al.* Chronic mirabegron treatment increases human brown fat, HDL cholesterol, and insulin sensitivity. *J. Clin. Invest.* **130**, 2209–2219 (2020).

7. Ramage, L. E. *et al.* Glucocorticoids Acutely Increase Brown Adipose Tissue Activity in Humans, Revealing Species-Specific Differences in UCP-1 Regulation. *Cell Metab.* **24**, 130–141 (2016).

8. Yan, C. *et al.* Peripheral-specific Y1 receptor antagonism increases thermogenesis and protects against diet-induced obesity. *Nat. Commun.* **12**, 1–20 (2021).

9. Chondronikola, M. *et al.* Brown adipose tissue improves whole-body glucose homeostasis and insulin sensitivity in humans. *Diabetes* **63**, 4089–4099 (2014).

10. Van Der Lans, A. A. J. J. *et al.* Cold acclimation recruits human brown fat and increases nonshivering thermogenesis. *J. Clin. Invest.* **123**, 3395–3403 (2013).

11. Lee, P. *et al.* Temperature-acclimated brown adipose tissue modulates insulin sensitivity in humans. *Diabetes* **63**, 3686–3698 (2014).

12. Hanssen, M. J. W. *et al.* Short-term cold acclimation improves insulin sensitivity in patients with type 2 diabetes mellitus. *Nat. Med.* **21**, 863–865 (2015).

13. Villarroya, F. & Giralt, M. The beneficial effects of brown fat transplantation: Further evidence of an endocrine role of brown adipose tissue. *Endocrinology* **156**, 2368–2370 (2015).

14. Payab, M. *et al.* Brown adipose tissue transplantation as a novel alternative to obesity treatment: a systematic review. *Int. J. Obes.* **45**, 109–121 (2021).

15. Betz, M. J. & Enerbäck, S. Therapeutic prospects of metabolically active brown adipose tissue in humans. *Front. Endocrinol. (Lausanne).* **2**, 86 (2011).

16. Kuryłowicz, A. & Puzianowska-Kuźnicka, M. Induction of adipose tissue browning as a strategy to combat obesity. *Int. J. Mol. Sci.* **21**, 1–28 (2020).

17. Liu, X. *et al.* Brown adipose tissue transplantation improves whole-body energy metabolism. *Cell Research* vol. 23 851–854 (2013).

18. Liu, Y., Fu, W., Seese, K., Yin, A. & Yin, H. Ectopic brown adipose tissue formation within skeletal muscle after brown adipose progenitor cell transplant augments energy expenditure. *FASEB J.* **33**, 8822–8835 (2019).

19. Liu, X. *et al.* Brown adipose tissue transplantation reverses obesity in Ob/Ob mice. *Endocrinology* **156**, 2461–2469 (2015).

20. Stanford, K. I. *et al.* Brown adipose tissue regulates glucose homeostasis and insulin sensitivity. *J. Clin. Invest.* **123**, 215–223 (2013).

21. Gunawardana, S. C. & Piston, D. W. Insulin-independent reversal of type 1 diabetes in nonobese diabetic mice with brown adipose tissue transplant. *Am. J. Physiol. - Endocrinol. Metab.* **308**, E1043–E1055 (2015).

22. Shankar, K. *et al.* Role of brown adipose tissue in modulating adipose tissue inflammation and insulin resistance in high-fat diet fed mice. *Eur. J. Pharmacol.* **854**, 354–364 (2019).

23. Cheng, L. *et al.* Brown and beige adipose tissue: a novel therapeutic strategy for obesity and type 2 diabetes mellitus. *Adipocyte* **10**, 48–65 (2021).

24. Zhou, X. *et al.* Brown adipose tissue-derived exosomes mitigate the metabolic syndrome in high fat diet mice. *Theranostics* **10**, 8197–8210 (2020).

25. Villarroya, F., Cereijo, R., Villarroya, J. & Giralt, M. Brown adipose tissue as a secretory organ. *Nat. Rev. Endocrinol.* **13**, 26–35 (2017).

26. Lee, M. W., Lee, M. & Oh, K. J. Adipose tissue-derived signatures for obesity and type 2 diabetes: Adipokines, batokines and microRNAs. *J. Clin. Med.* **8**, 854 (2019).

27. White, J. D., Dewal, R. S. & Stanford, K. I. The beneficial effects of brown adipose tissue transplantation. *Mol. Aspects Med.* **68**, 74–81 (2019).

28. Gunawardana, S. C. & Piston, D. W. Reversal of type 1 diabetes in mice by brown adipose tissue transplant. *Diabetes* **61**, 674–682 (2012).

29. Liu, X., Cervantes, C. & Liu, F. Common and distinct regulation of human and mouse brown and beige adipose tissues: a promising therapeutic target for obesity. *Protein and Cell* vol. 8 446–454 (2017).

30. Loh, R. K. C., Kingwell, B. A. & Carey, A. L. Human brown adipose tissue as a target for obesity management; beyond cold-induced thermogenesis. *Obes. Rev.* **18**, 1227–1242 (2017).

31. Wang, C. H. *et al.* CRISPR-engineered human brown-like adipocytes prevent diet-induced obesity and ameliorate metabolic syndrome in mice. *Sci. Transl. Med.* **12**, (2020).

32. Wang, C. H. *et al.* CRISPR-engineered human brown-like adipocytes prevent diet-induced obesity and ameliorate metabolic syndrome in mice. *Sci. Transl. Med.* **12**,

(2020).

33. Xue, R. *et al.* Clonal analyses and gene profiling identify genetic biomarkers of the thermogenic potential of human brown and white preadipocytes. *Nat. Med.* **21**, 760–768 (2015).

34. Kuss, M. *et al.* Effects of tunable, 3D-bioprinted hydrogels on human brown adipocyte behavior and metabolic function. *Acta Biomater.* **71**, 486–495 (2018).

35. Hafner, A. L. *et al.* Brown-like adipose progenitors derived from human induced pluripotent stem cells: Identification of critical pathways governing their adipogenic capacity. *Sci. Rep.* **6**, 32490 (2016).

36. Lei, Y. & Schaffer, D. V. A fully defined and scalable 3D culture system for human pluripotent stem cell expansion and differentiation. *Proc. Natl. Acad. Sci. U. S. A.* **110**, E5039-48 (2013).

37. Li, Q. *et al.* Scalable and physiologically relevant microenvironments for human pluripotent stem cell expansion and differentiation. *Biofabrication* **10**, 025006 (2018).

38. Lin, H. *et al.* Automated Expansion of Primary Human T Cells in Scalable and Cell-Friendly Hydrogel Microtubes for Adoptive Immunotherapy. *Adv. Healthc. Mater.* **7**, 1701297 (2018).

39. Lei, Y., Jeong, D., Xiao, J. & Schaffer, D. V. Developing Defined and Scalable 3D Culture Systems for Culturing Human Pluripotent Stem Cells at High Densities.

Cell Mol Bioeng **7**, 172–183 (2014).

40. Li, Q. *et al.* A simple and scalable hydrogel-based system for culturing protein-producing cells. *PLoS One* **13**, e0190364 (2018).

41. Lin, H., Li, Q. & Lei, Y. Three-dimensional tissues using human pluripotent stem cell spheroids as biofabrication building blocks. *Biofabrication* **9**, 025007 (2017).

42. Li, Q. *et al.* Scalable Production of Glioblastoma Tumor-initiating Cells in 3 Dimension Thermoreversible Hydrogels. *Sci. Rep.* **6**, 31951 (2016).

43. Lin, H. *et al.* A Scalable and Efficient Bioprocess for Manufacturing Human Pluripotent Stem Cell-Derived Endothelial Cells. *Stem Cell Reports* **11**, 454–469 (2018).

44. Lin, H., Li, Q. & Lei, Y. An Integrated Miniature Bioprocessing for Personalized Human Induced Pluripotent Stem Cell Expansion and Differentiation into Neural Stem Cells. *Sci. Rep.* **7**, 40191 (2017).

45. Jofra, T. *et al.* Murine Pancreatic Islets Transplantation under the Kidney Capsule. *Bio-Protocol* **8**, e2743–e2743 (2018).

46. Szot, G. L., Koudria, P. & Bluestone, J. A. Transplantation of pancreatic islets into the kidney capsule of diabetic mice. *J. Vis. Exp.* (2007) doi:10.3791/404.

47. Nishimura, T., Katsumura, T., Motoi, M., Oota, H. & Watanuki, S. Experimental evidence reveals the UCP1 genotype changes the oxygen consumption attributed

to non-shivering thermogenesis in humans. *Sci. Rep.* **7**, 5570 (2017).

48. Ricquier, D. Uncoupling protein 1 of brown adipocytes, the only uncoupler: A historical perspective. *Front. Endocrinol. (Lausanne).* **2**, 85 (2011).

49. Winer, S. *et al.* Normalization of obesity-associated insulin resistance through immunotherapy. *Nat. Publ. Gr.* **15**, 921–930 (2009).

50. Lee, Y. S. *et al.* Inflammation is necessary for long-term but not short-term high-fat diet-induced insulin resistance. *Diabetes* **60**, 2474–2483 (2011).

51. Gamble, A. *et al.* Improved islet recovery and efficacy through co-culture and co-transplantation of islets with human adipose-derived mesenchymal stem cells. *PLoS One* **13**, e0206449 (2018).

52. Pajvani, U. B. & Scherer, P. E. Adiponectin: Systemic contributor to insulin sensitivity. *Curr. Diab. Rep.* **3**, 207–213 (2003).

53. Maeda, N. *et al.* Diet-induced insulin resistance in mice lacking adiponectin/ACRP30. *Nat. Med.* **8**, 731–737 (2002).

54. Matsuda, M. *et al.* Role of adiponectin in preventing vascular stenosis. The missing link of adipo-vascular axis. *J. Biol. Chem.* **277**, 37487–37491 (2002).

55. Galic, S., Oakhill, J. S. & Steinberg, G. R. Adipose tissue as an endocrine organ. *Mol. Cell. Endocrinol.* **316**, 129–139 (2010).

56. Fantuzzi, G. Adipose tissue, adipokines, and inflammation. *J. Allergy Clin.*

Immunol. **115**, 911–919 (2005).

57. Wang, G. X., Zhao, X. Y. & Lin, J. D. The brown fat secretome: Metabolic functions beyond thermogenesis. *Trends Endocrinol. Metab.* **26**, 231–237 (2015).

58. Bozaoglu, K. *et al.* Chemerin is a novel adipokine associated with obesity and metabolic syndrome. *Endocrinology* **148**, 4687–4694 (2007).

59. Buechler, C., Feder, S., Haberl, E. M. & Aslanidis, C. Chemerin isoforms and activity in obesity. *Int. J. Mol. Sci.* **20**, 1128 (2019).

60. Yadav, H. & Rane, S. G. TGF-β/Smad3 signaling regulates brown adipocyte induction in white adipose tissue. *Front. Endocrinol. (Lausanne).* **3**, 35 (2012).

61. Yadav, H. *et al.* Protection from obesity and diabetes by blockade of TGF-β/Smad3 signaling. *Cell Metab.* **14**, 67–79 (2011).

62. Lin, H., Li, Q. & Lei, Y. An Integrated Miniature Bioprocessing for Personalized Human Induced Pluripotent Stem Cell Expansion and Differentiation into Neural Stem Cells. *Sci. Rep.* **7**, 40191 (2017).

63. Honek, J. *et al.* Brown adipose tissue, thermogenesis, angiogenesis: Pathophysiological aspects. *Horm. Mol. Biol. Clin. Investig.* **19**, 5–11 (2014).

64. Cao, Y. Angiogenesis and vascular functions in modulation of obesity, adipose metabolism, and insulin sensitivity. *Cell Metab.* **18**, 478–489 (2013).

65. Bagchi, M. *et al.* Vascular endothelial growth factor is important for brown

adipose tissue development and maintenance. *FASEB J.* **27**, 3257–3271 (2013).

66. Shimizu, I. *et al.* Vascular rarefaction mediates whitening of brown fat in obesity. *J. Clin. Invest.* **124**, 2099–2112 (2014).

67. Mahdaviani, K., Chess, D., Wu, Y., Shirihai, O. & Aprahamian, T. R. Autocrine effect of vascular endothelial growth factor-A is essential for mitochondrial function in brown adipocytes. *Metabolism.* **65**, 26–35 (2016).

68. Lin, H. *et al.* Integrated generation of induced pluripotent stem cells in a low-cost device. *Biomaterials* **189**, 23–36 (2019).

69. Li, Q. *et al.* Scalable Culturing of Primary Human Glioblastoma Tumor-Initiating Cells with a Cell-Friendly Culture System. *Sci. Rep.* **8**, 3531 (2018).

70. Lin, H. *et al.* Hydrogel-Based Bioprocess for Scalable Manufacturing of Human Pluripotent Stem Cell-Derived Neural Stem Cells. *ACS Appl. Mater. Interfaces* **10**, 29238–29250 (2018).

71. Lin, H. *et al.* Manufacturing human pluripotent stem cell derived endothelial cells in scalable and cell-friendly microenvironments. *Biomater. Sci.* **7**, 373–388 (2019).

72. Lin, H. *et al.* Engineered Microenvironment for Manufacturing Human Pluripotent Stem Cell-Derived Vascular Smooth Muscle Cells. *Stem Cell Reports* **12**, 84–97 (2019).

73. Wang, O. & Lei, Y. Creating a cell-friendly microenvironment to enhance cell

culture efficiency. *Cell Gene Ther. Insights* **5**, 341–350 (2019).

74. Trayhurn, P. & Alomar, S. Y. Oxygen deprivation and the cellular response to hypoxia in adipocytes - Perspectives on white and brown adipose tissues in obesity. *Front. Endocrinol. (Lausanne).* **6**, 19 (2015).

75. Sun, K. *et al.* Brown adipose tissue derived VEGF-A modulates cold tolerance and energy expenditure. *Mol. Metab.* **3**, 474–483 (2014).

76. Shi, Y., Inoue, H., Wu, J. C. & Yamanaka, S. Induced pluripotent stem cell technology: A decade of progress. *Nat. Rev. Drug Discov.* **16**, 115–130 (2017).

77. Takahashi, K. *et al.* Induction of Pluripotent Stem Cells from Adult Human Fibroblasts by Defined Factors. *Cell* **131**, 861–872 (2007).

78. Okita, K. *et al.* A more efficient method to generate integration-free human iPS cells. *Nat. Methods* **8**, 409–412 (2011).

79. Araki, R. *et al.* Negligible immunogenicity of terminally differentiated cells derived from induced pluripotent or embryonic stem cells. *Nature* **494**, 100–104 (2013).

80. Mandai, M. *et al.* Autologous Induced Stem-Cell–Derived Retinal Cells for Macular Degeneration. *N. Engl. J. Med.* **376**, 1038–1046 (2017).

81. Zhao, W. *et al.* Strategies for Genetically Engineering Hypoimmunogenic Universal Pluripotent Stem Cells. *iScience* **23**, 101162 (2020).

82. Han, X. *et al.* Generation of hypoimmunogenic human pluripotent stem cells. *Proc. Natl. Acad. Sci. U. S. A.* **116**, 10441–10446 (2019).

83. Deuse, T. *et al.* Hypoimmunogenic derivatives of induced pluripotent stem cells evade immune rejection in fully immunocompetent allogeneic recipients. *Nat. Biotechnol.* **37**, 252–258 (2019).

84. Frederiksen, H. R., Doehn, U., Tveden-Nyborg, P. & Freude, K. K. Non-immunogenic Induced Pluripotent Stem Cells, a Promising Way Forward for Allogenic Transplantations for Neurological Disorders. *Front. Genome Ed.* **2**, (2021).

85. Brown, A. C. Brown adipocytes from induced pluripotent stem cells—how far have we come? *Ann. N. Y. Acad. Sci.* **1463**, 9–22 (2020).

86. Oka, Kobayashi, Matsumura, Nishio & Saeki. Exogenous Cytokine-Free Differentiation of Human Pluripotent Stem Cells into Classical Brown Adipocytes. *Cells* **8**, 373 (2019).

87. Hafner, A.-L. Human induced pluripotent stem cells: A new source for brown and white adipocytes. *World J. Stem Cells* **6**, 467 (2014).

88. Saeki, K. *et al.* Production of functional classical brown adipocytes from human pluripotent stem cells using specific hemopoietin cocktail without gene transfer. *Cell Metab.* **16**, 394–406 (2012).

89. Ahfeldt, T. *et al.* Programming human pluripotent stem cells into white and brown

adipocytes. *Nat. Cell Biol.* **14**, 209–219 (2012).

90. Nishio, M. & Saeki, K. Differentiation of human pluripotent stem cells into highly functional classical brown adipocytes. *Methods in Enzymology* vol. 537 177–197 (2014).

CHAPTER 5. SCALABLE CULTURE OF MYOCYTES IN ALGINATE HYDROGEL MICROTUBES

Introduction

Based on the Food and Agriculture Organization (FAO) data, the global population is expected to reach 9 billion by 2050. Accordingly, 70% more food will be needed to feed this population. Meat is a significant part of human food[1]. Currently, meat is obtained from natural animals or livestock raised through traditional farms or modern factories[2–4]. The natural supply is clearly limited. Livestock farming requires large amounts of water and land and will reach a limitation. Additionally, farming causes significant environmental and animal welfare issues[5,6]. Therefore, alternative approaches that can produce meat in an efficient and environmentally friendly way are highly wanted.

One option is to produce meat via cell culture[7–9]. Briefly, animal cells are expanded to generate large numbers and differentiated into myocytes that are assembled into muscle tissues. This approach is currently at the proof-of-concept stage. A few significant technological challenges must be addressed for its further advance. One of these challenges is to produce cells at large scales in a cost-effective way. Tons of cell mass will be needed per day for meat production. None of the current cell culture technologies, e.g., 2-dimensional (2D) flasks and stirred tank bioreactors (STRs), can achieve this scale and price. For instance, STRs can only produce ~$2x10^6$ cells/mL. This cell mass occupies ~0.4% of the culture volume. Growing>10^{11} cells/batch with STRs is still difficult.

Previously, our lab developed a new cell culture system termed AlgTubes[10–17]. With

this method, cells are cultured in hollow, microscale alginate hydrogel tubes. AlgTubes provide a cell-friendly microenvironment, resulting in paradigm-shifting improvements in cell viability, growth rate, yield, culture consistency, scalability. When culturing human stem cells and adult cells, we have achieved up to $5x10^8$ cells/mL volumetric yield, which is ~250 times the current-state-of-the-art. AlgTubes make large-scale cell production feasible. For instance, to produce 10^{12} cells from $1x10^7$ cell seeds, our modeling shows that AlgTubes (vs. the current stirred tank bioreactors) reduce the culture volume from 1365 to 4.0 litters, culture time from 40 to 20 days, and passaging operations from 9 to 1, collectively reducing the production cost and increasing the production capability in a significant manner. Thus AlgTubes have huge potential for culturing animal cells for meat production. In this work, we systematically re-engineered the AlgTubes and studied culturing animal myoblasts to produce meat.

Materials and Methods

Cell lines and Materials

Mouse bone marrow mesenchymal stem cell line (D1, CRL-12424), mouse myoblast cell line (C2C12, CRL-1772), quail myoblast cell line (QM7, CRL-1962), mouse beige adipocyte cell line (X9, CRL-3282), mouse fibroblast cell line (3T3, CRL-1658) were purchased from ATCC and maintained as instructed by ATCC. Briefly, C2C12, D1, and 3T3 were cultured in DMEM supplemented with 10% FBS. QM7 were cultured in medium 199 supplemented with 10% TPB and 10% FBS. X9 were cultured in DMEM/F12 supplemented with 15% FBS and 2.36 mM L-glutamine. All cell culture medium was

refreshed every 2-3 days. To induce C2C12 and QM7 myotube formation, the culture medium was supplemented with 10% horse serum instead of fetal bovine serum.

Additionally, the following chemicals and reagents were also used for the project: sodium alginate (cat # 194-13321, 80~120cp, Wako Chemicals), sodium hyaluronate: (cat # HA 700K-5, Lifecore Biomedical), tryptose phosphate broth (TPB, cat # 18050039, Life Technologies), Dulbecco's Modified Eagle's Medium (DMEM, cat # 30-2002, ATCC), Medium 199 with Earle's BSS (cat # 12119F, Lonza), DMEM/F12 (cat # 30-2006, ATCC), Fetal Bovine Serum (FBS, cat # 10437028, Gibco), L-Glutamine (cat # 25030081, Gibco), propidium iodide (cat # 195458, MP Biomedicals, LLC), Vybrant multi-color cell-labeling kit (cat # V22889, Molecular Probes), MF20 antibody (cat # MAB4470, R&D systems), RGD peptide (Genscript), Alginate Lyase (cat # A1603, Sigma).

Modifying Alginates with RGD peptides

2% alginate was dissolved in 0.1N NaOH and reacted with DVS (1:3 molar ratio between OH group and DVS) for 14 minutes. 20% to 30% of the OH groups in alginate polymers were modified with DVS. Dialysis was done to remove excessive DVS. The RGD peptide containing cysteine was used to react with alginate-vs under the alkaline condition to make alginate-RGD. 10% of the modified OH groups were reacted with RGD peptides. Alginate-RGD were mixed with unmodified alginate to make a 2% alginate solution with 1 mM RGD concentration.

Processing alginate-RGD hydrogel tubes (AlgTubes)

A custom-made micro-extruder was used to process AlgTubes. A hyaluronic acid (HA) solution containing single cells and an alginate-RGD solution are pumped into the central and side channel of the micro-extruder, respectively, to form coaxial core-shell flows that are extruded into a $CaCl_2$ buffer (100mM) to make AlgTubes. Subsequently, $CaCl_2$ buffer was replaced by cell culture medium. Detailed methods of culturing cells in alginate hydrogel tubes can be found in our previous publications[10–16].

Culturing cells in AlgTubes

For typical cell culture, 20 µL of cell solution in AlgTubes were suspended in 3 mL medium in a 6-well plate. Cells were seeded at the density of 1-2x10^6 cells/mL hydrogel tube space. 2% alginate modified with 1 mM RGD peptide was used. The hydrogel tube diameter was 200 – 300 µm with shell thickness around 30-70 µm. To passage cells, the medium was removed, and alginate hydrogels were dissolved with 0.5mM EDTA and 100 µg/ mL alginate lyase for 10 min at 37 ºC. Cell mass was collected by centrifuging at 100 g for 5 min and treated with 0.25% trypsin-EDTA at 37 ºC for 10 min and dissociated into single cells. Digestion was neutralized by complete cell culture medium.

Immunocytochemistry

Cells cultured on 2D were fixed with 4% paraformaldehyde (PFA) at room temperature for 15 min, permeabilized with 0.25% Triton X-100 for 10 min, and blocked with 5% donkey serum for 1 h before incubating with primary antibodies in DPBS + 0.25% Triton X-100 + 5% donkey serum at 4 ℃ overnight. After washing, secondary antibodies

were added and incubated at room temperature for 2 h followed by incubating with 10 mM 4',6-Diamidino-2-Phenylindole, Dihydrochloride (DAPI) for 10 min. Cells were washed with DPBS three times before imaging with a Fluorescent Microscopy. For 3D fibrous cell mass immunostaining, cell mass was fixed with 4% PFA at 4 °C overnight. 40 μm thick tissue sections were obtained via cryosection. The sections were washed with DPBS three times and stained as the 2D cell cultures. Alternatively, the cell mass was directly incubated with primary antibody at 4 ºC for 48 h after fixed and wash. After extensive wash, secondary antibody was added and incubated at 4 ºC for 24 h followed by incubating with 10 mM DAPI for 10 min and imaged with a Fluorescent Microscopy.

Statistical analysis

The data are presented as the mean ± SEM. We used one-way ANOVA to compare all groups. $P < 0.05$ was considered statistically significant.

Results

The engineered Alginate-RGD culture system (AlgTubes)

We modified our alginate hydrogel tubes (AlgTubes) with RGD peptides so that anchor-dependent myoblasts could be cultured in AlgTubes. Briefly, the sodium alginate was dissolved in 0.1 N NaOH and reacted with DVS through “click” chemistry to generate VS groups on the alginate polymers[18]. The RGD peptides with free -SH groups then reacted with these VS groups via Michael addition reaction. Alginate-RGD was mixed with unmodified alginate to produce a 2% alginate solution with 1 mM RGD concentration,

used to process AlgTubes. A cell solution and the 2% alginate-RGD solution were pumped into the central and side channel of a custom-made micro-extruder, respectively, to form a coaxial core-shell flow extruded through a nozzle and into a $CaCl_2$ buffer (100 mM) (**Figure 5.1A and 5.1B**). The shell alginate flow was crosslinked by Ca^{2+} ions in seconds to form an alginate hydrogel tube. Subsequently, cells were grown in the tubes suspended in the cell culture medium in a 6-well plate.

The AlgTubes system is designed to provide cells with a friendly microenvironment (**Figure 5.1C**). First, RGD peptides allow cells to attach to a substrate and proliferate. Second, oxygen, nutrients, and macromolecules (with Mw up to 700 kDa) can freely and quickly diffuse through the hydrogel shell. Third, the hydrogel tubes direct cell expansion axially while confining the radial diameter of cell masses within the diffusion limit (~400 μm) to ensure efficient mass transport during the whole culture period. As shown in our previous research, the diffusion limit in 3D human cell culture is typically less than 500 μm[10–17]. Forth, the hydrogel tubes also isolate hydrodynamic stresses from cells. Lastly, the tubes provide free and uniform 3D microspaces that allow cells to interact with each other and grow (**Figure 5.1C**).

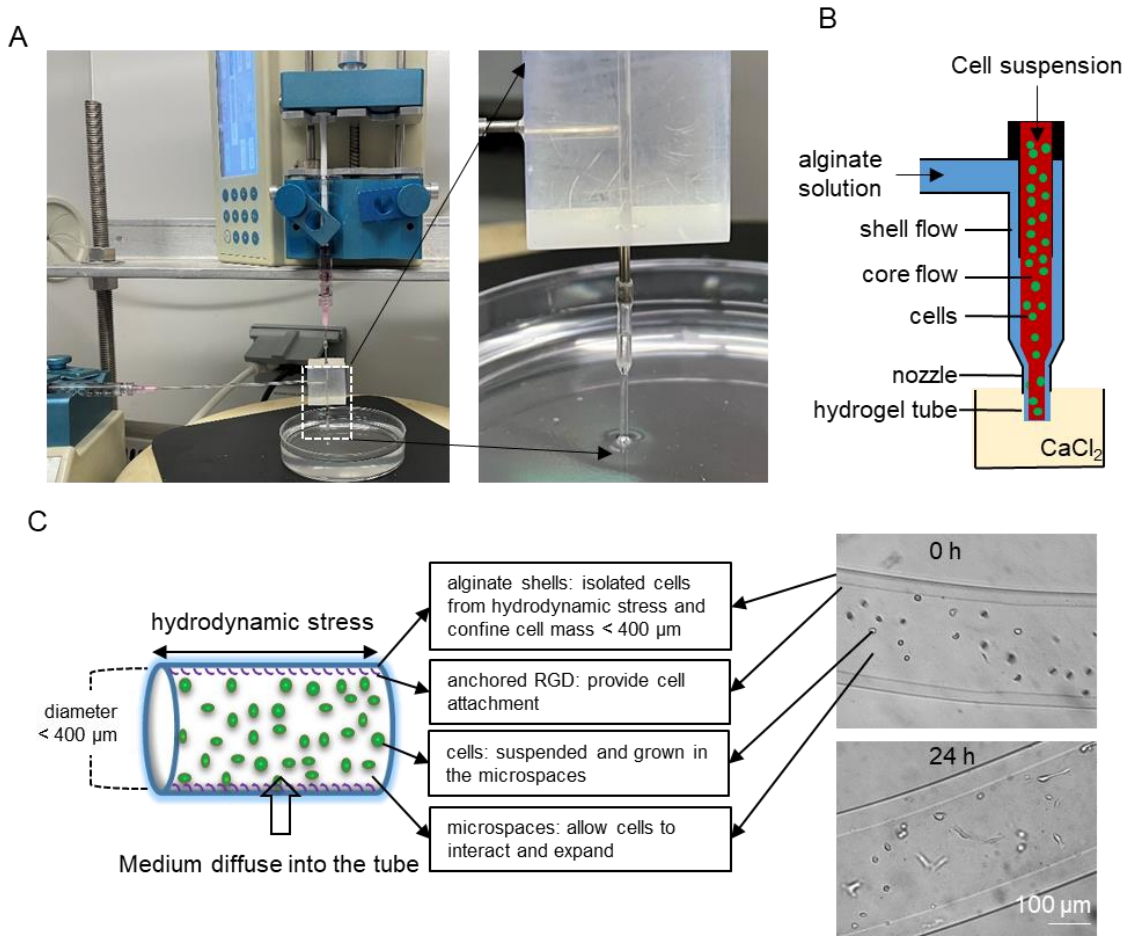

Figure 5.1. Overview of culturing cells in alginate hydrogel tubes (AlgTubes). (A, B) Process AlgTubes. A cell suspension and an alginate solution is pumped into the central channel and side channel of the microextruder, respectively, to form a coaxial coreshell flow that is extruded through the nozzle into the $CaCl_2$ buffer. The shell alginate flow is crosslinked by Ca^{2+} ions to form an alginate hydrogel tube within seconds. (C) Illustration of cell microenvironment of AlgTubes.

C2C12 expansion in AlgTubes

We cultured C2C12 in AlgTubes for 19 days (**Figure 5.2**). Day 0 image showed our seeding density was very low ($1x10^6$ cells/mL hydrogel tube spaces). Only a few cells could be found in the amplified image on day 0. A low cell seeding density allows a large expansion fold per passage and is wanted for industrial cell production. After 24 hours, almost all cells attached to the hydrogel tube inner surface with no or minor cell death. On day 4, cells expanded significantly and formed a confluent monolayer. On day 7, multilayer cell masses were seen (green arrows). The dark-field image on day 7 showed white cell mass (orange arrows), indicating 3D multilayer cell masses. After 14 days, the dark-field images show extensive 3D white cell masses (yellow arrows), and myotubes could be found in phase images (blue arrows). We found that some locations of the tubes were bent (**Figure 5.2A,** red arrows) after 14 days, indicating the myotube contraction force was more significant than the hydrogel elasticity. AlgTubes with stronger Young's modulus can overcome this problem to further enhance the cell culture outcome in the future. The modulus can be increased by increasing the alginate concentration or using high molecular weight alginate or thicker shells.

Live/Dead cell staining of the cell fibers on day 19 showed most cells were live cells, and a few dead cells were detected, indicating high viability of C2C12 cultured in AlgTubes after 19 days (**Figure 5.3A**). We counted the cells using Countless II cell counter. The cell quantification shows that C2C12 cells reached ~$6.4x10^7$ and ~$1.1x10^8$ cells/mL hydrogel tubes space on day 10 and day 19, respectively (**Figure 5.3B**). The released day 19 cells had healthy morphology. There were some large cell aggregates (**Figure 5.3C**,

green arrows), which might be the contracted myotubes. Immunostaining on myofiber (MF20) confirmed the existence of myotubes (**Figure 5.3C**). Our results agree with the literature findings that C1C12 cells spontaneously differentiate to form myotubes at high density even in the expansion medium.

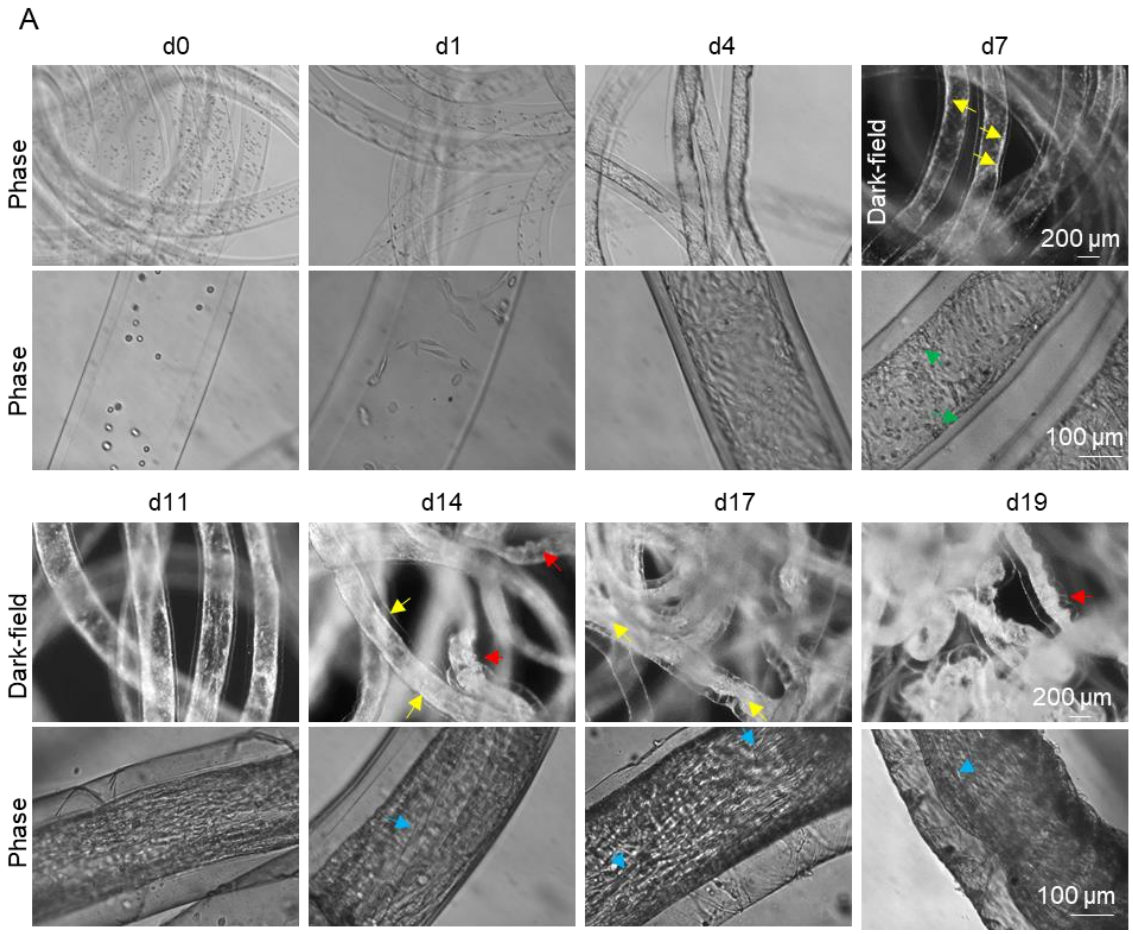

Figure 5.2. C2C12 expansion in AlgTubes. (A) Phase or dark-field pictures of C2C12 cells in AlgTubes on different days. Green arrows: multilayer cell masses; yellow arrows: 3D white cells mass; blue arrows: myotubes; red arrows: bent tubes.

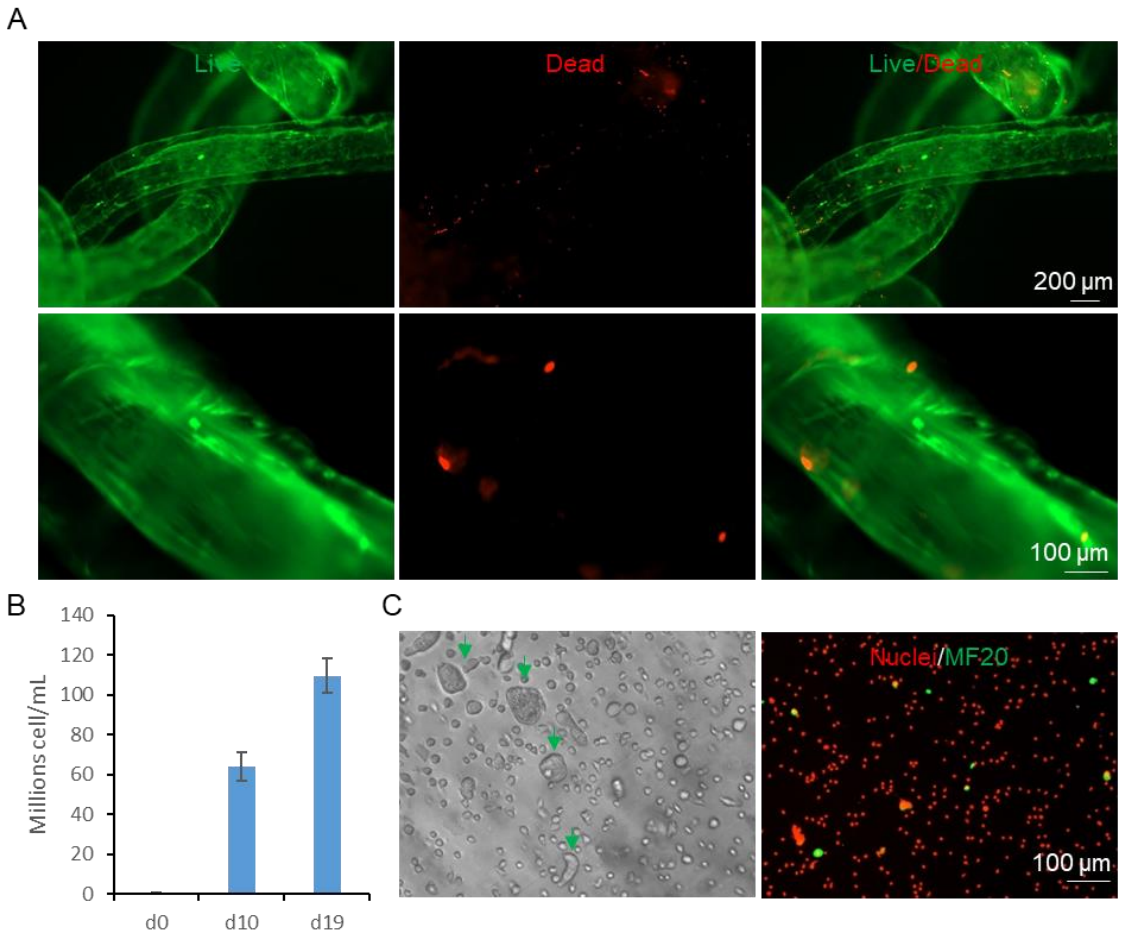

Figure 5.3. Viability and quantification of C2C12 expansion in AlgTubes. (A) Live/Dead cell staining of C2C12 in AlgTubes on day 19. (B) C2C12 quantification on day 0, day 10 and day 19. (C) Single C2C12 cells released from Alg-RGD-Tubes on day 19 and stained with MF20 and PI. Green arrows: myotubes.

C2C12 differentiation in AlgTubes

C2C12 cells were expanded for 7 days in AlgTubes before initiating differentiation (**Figure 5.4**). Cells formed 3D cell masses with the differentiation protocol, indicating that cells maintained proliferation during the differentiation process. Myotubes could be seen after six days of differentiation (**Figure 5.4A,** blue arrows). Most cells were live based on the Live/Dead cell staining assay (**Figure 5.4B**). After differentiation for 12 days, the volumetric yield reached ~$1.2x10^8$/mL (**Figure 5.7C**). We used immunostaining to evaluate the formed myotubes (**Figure 5.5**). The staining confirmed the 3D cell masses in the hydrogel tubes. There was still some space at the tube core (**Figure 5.5B and 5.5D**). Smaller tubes can be used in the future. A large percentage of cells were MF20 positive (**Figure 5.5A and 5.5B**). The myotubes were large and aligned along the hydrogel tubes. Most cells expressed MyoD and PAX7, indicating the cell renewal was repressed, and muscle differentiation was promoted (**Figure 5.5C and 5.5D**).

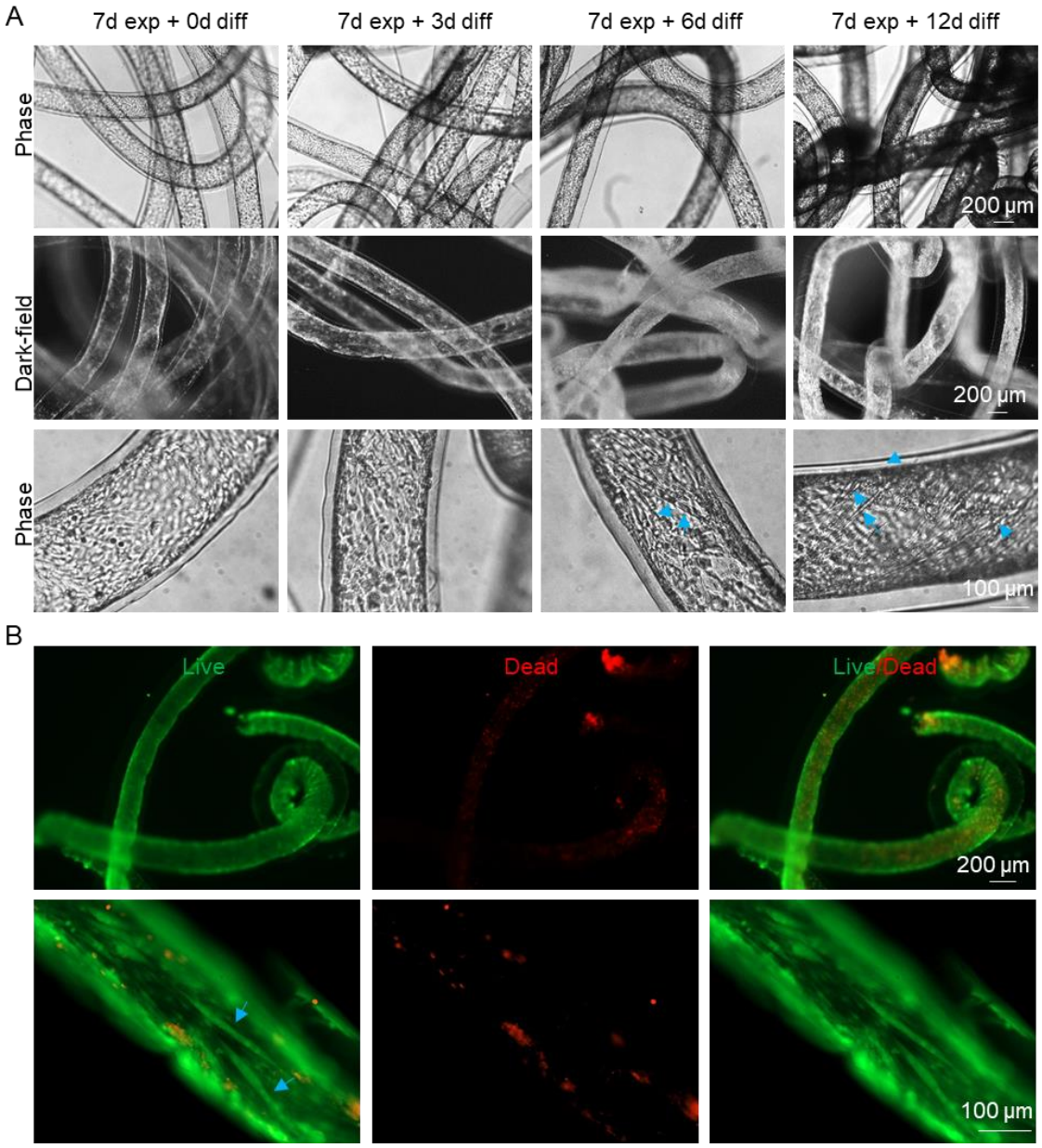

Figure 5.4. C2C12 differentiation in AlgTubes. C2C12 were cultured for 7 days in alginate tube before differentiation. (A) Phase or dark-field pictures of C2C12 differentiation in AlgTubes on different days. (B) Live/Dead cell staining on day 19. Blue arrows: Myotubes

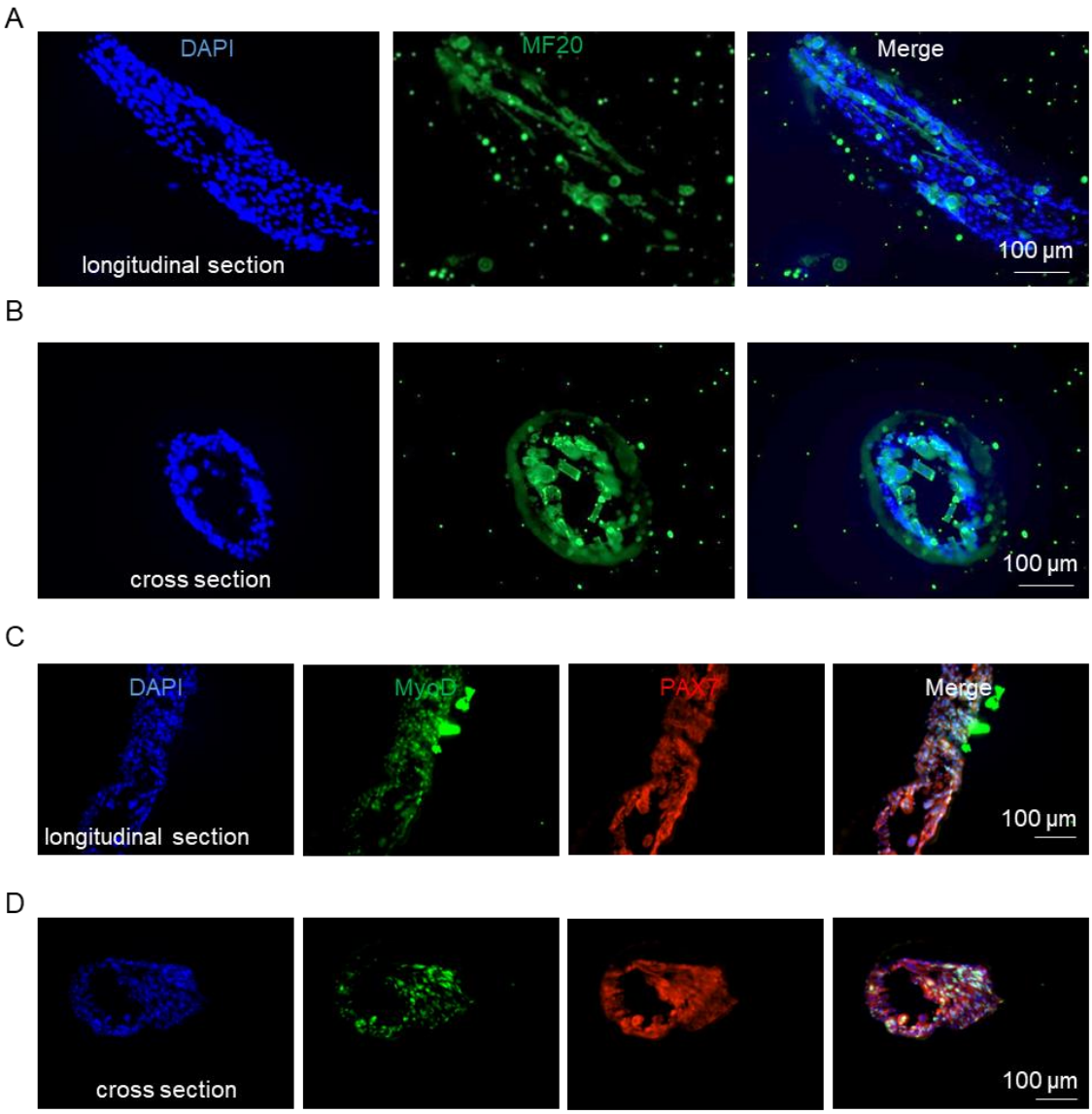

Figure 5.5. Immunostaining of C2C12 expanded for 7 days and differentiated for 12 days in AlgTubes. Cell fibers were fixed, cryosection and stained with myofiber (MF20) and DPAI (A, B), and stained with MyoD and PAX7 (C, D).

C2C12 and D1 co-culture and differentiation

Our previous research found that mesenchymal stem cells (MSCs) or fibroblasts could significantly improve cell viability in high density cell culture. We thus did a co-culture experiment to evaluate if mouse MSCs (D1 cells) could boost the growth rate and yield of C2C12 in AlgTubes (**Figure 5.6**). D1 cells were pre-stained with vibrant cell-labeling DIO (green color). C2C12 cells were seeded at $1x10^6$ cells/mL with $1x10^5$ D1 cells/mL hydrogel tube spaces. Initially, few cells could be observed in the amplified image. After 24 hours, most of the cells showed round and spread morphology, suggesting almost all cells attached to the hydrogel tubes. On day 4, a confluent cell monolayer was formed on the inner surface of alginate tubes. Cells proliferate rapidly and generate a confluent monolayer. On day 7, The cells kept expanding, multilayer cell masses were seen (**Figure 5.6A**, green arrows on d7). The white cell mass in the dark-field image (**Figure 5.6A,** yellow arrows on d7) indicated 3D multilayer cell masses were formed. After the cells were cultured for 14 days, the more extensive 3D white cell masses were constructed in the hydrogel tubes (yellow arrows), and myotubes could be found (blue arrows). Alginate hydrogel tubes were bent by the strong cell contractile force after 14 days (red arrows), indicating the hydrogel elasticity is not enough for the myotube contraction (**Figure 5.6A**). Only 10% of D1 cells were applied to avoid taking over the culture. Fluorescent images on day 0 to day 7 suggested D1 cells did not have a growth advantage over C2C12 cells (**Figure 5.6B**). Cells exhibited healthy morphologies when they were harvested and digested into single cells (**Figure 5.6C**). Immunostaining on myofiber (MF20) showed the existence of myotubes, indicating D1 cells did not inhibit the spontaneous C2C12 cell

differentiation (**Figure 5.6C**).

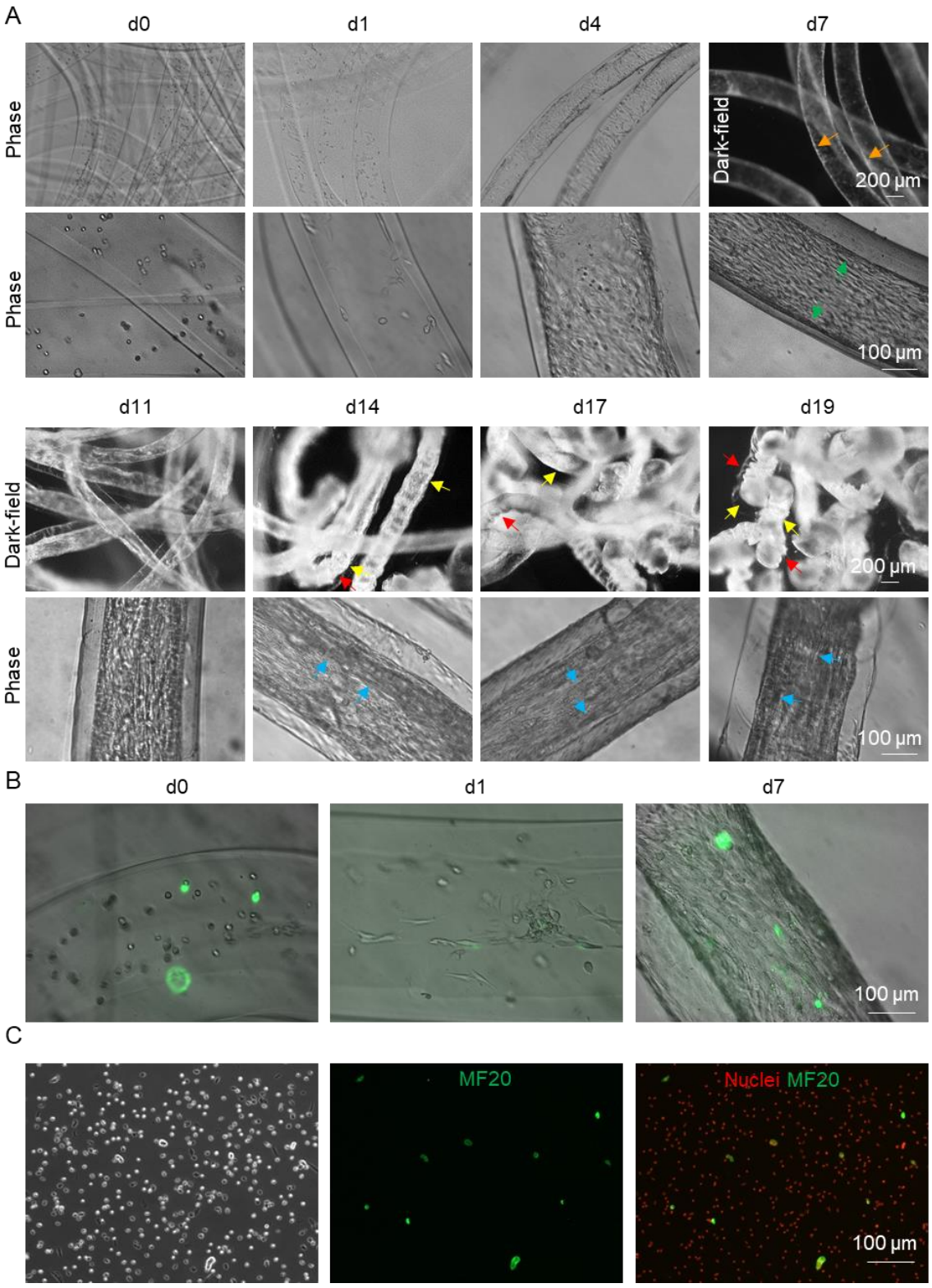

Figure 5.6. C2C12 and D1 cells co-culture in AlgTubes. (A) Phase or dark-field pictures of cells in AlgTubes on different days. (B) Phase and fluorescent images of cells in AlgTubes. Green: D1 cells. (C) Cells were released from the tubes on day 19 and stained with MF20 and PI. Green arrows: multilayer cell masses; yellow arrows: 3D white cells mass; blue arrows: myotubes; red arrows: bent tubes.

We evaluated if C2C12 cells could be differentiated when D1 cells were presented. After co-cultured for 6 days, the medium was changed to a differentiation medium. The differentiation was similar to monoculture (**Figure 5.7**). Cells maintained proliferation to form 3D cell masses, and myotubes could be seen after six days of differentiation (**Figure 5.7A,** blue arrows). The immunostaining shows that most cells were MF20 positive, indicating D1 cells did not inhibit C2C12 differentiation (**Figure 5.7B**). Based on images, D1 cells did not significantly change the cell culture. However, cell counting showed that co-culture improved the volumetric yield, especially under differentiation conditions (**Figure 5.8**). In expansion medium, C2C12 cells reached ~$6.4x10^{7,}$ and ~$1.1x10^{8}$ cells/mL hydrogel tubes tube space on day 10 and 19, respectively (**Figure 5.3B**). D1 co-culturing improved the yield to ~$1.3x10^{8}$ cells/ml hydrogel tubes. In the differentiation medium, ~$1.2x10^{8}$ cells/ml hydrogel tubes were achieved on day 19. D1 co-culturing increased the yield to ~$1.6x10^{8}$ cells/ml hydrogel tubes (**Figure 5.8**). The Countless II cell counter was applied in this counting process. The actual yields should be higher than the numbers listed above since the cell counter excluded the large cell aggregates, which were commonly observed on day 19.

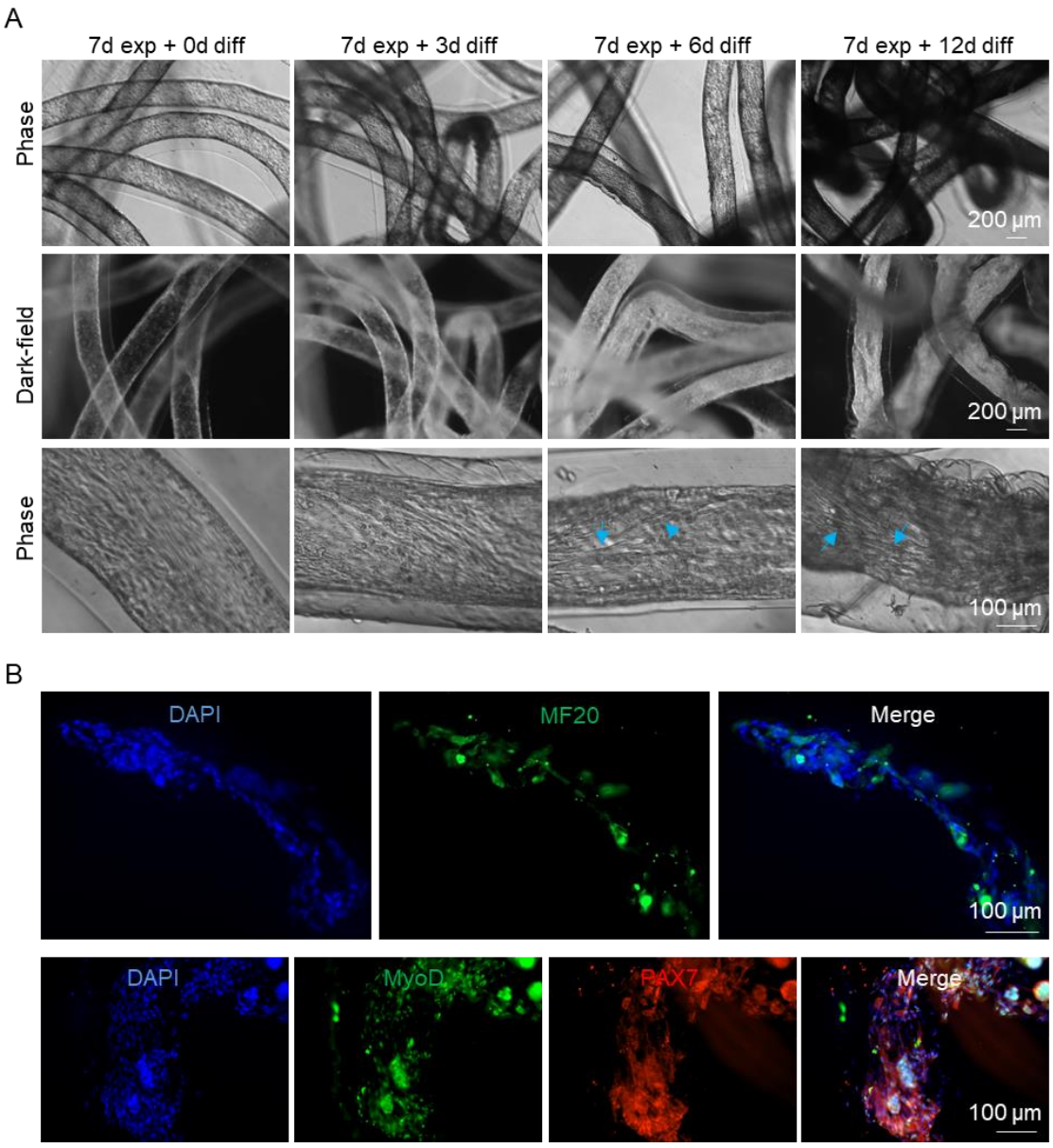

Figure 5.7. C2C12 and co-culture and differentiation in AlgTubes. C2C12 and D1 cells were cultured for 7 days in alginate tube before differentiation. (A) Phase or dark-field pictures of C2C12 differentiation in AlgTubes on different days. (B) cell fiber cryosections were immunostained with MF20, MyoD and PAX7. Blue arrows: Myotubes.

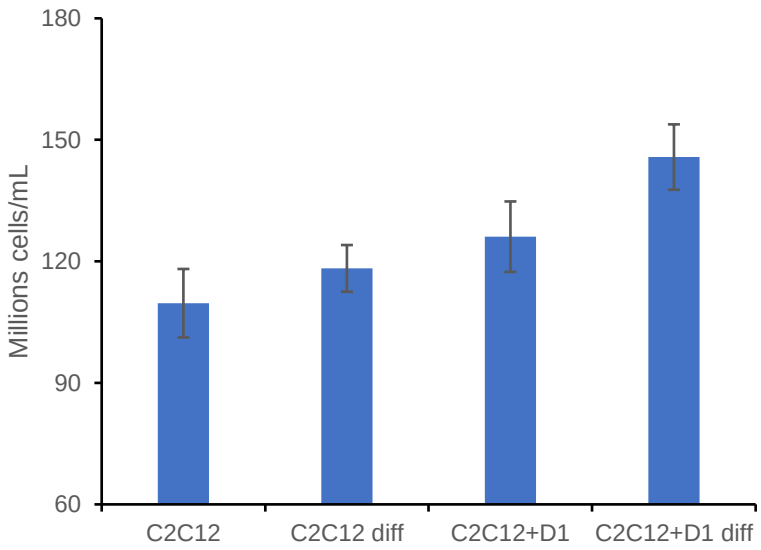

Figure 5.8. Quantifications of C2C12 cultured under different conditions in AlgTubes on day 19.

QM7 expansion in AlgTubes

We then cultured myoblasts from a second species quail (QM7) in AlgTubes for 18 days (**Figure 5.9**). After 24 hours, most cells attached to the hydrogel tube wall and exhibited fibroblast-like morphology. The day 3 images showed cells expanded significantly. However, a confluent monolayer had yet formed. On day 6, multilayer cell masses were seen (**Figure 5.9A**, green arrows). The dark-field image also had white cell mass (**Figure 5.9A**, yellow arrows), indicating 3D multilayer cell masses. However, some hydrogel inner surfaces were still not covered with cells (**Figure 5.9A**, blue arrow). This was different from C2C12 cells (**Figure 5.2A**), which formed a confluent monolayer before forming 3D cell masses. This data indicated quail cells might have stronger cell-to-cell interactions and weaker cell-to-hydrogel matrix interactions than the C2C12 cells. Most likely, quail cells express fewer integrins for the RGD ligands than C2C12 cells. We expect

that increasing the RGD concentration or increasing the hydrogel tube modulus will enhance cell adhesion and enhance cell culture outcomes. After 9 days, the dark-field images showed extensive 3D white cell masses (**Figure 5.9A**, yellow arrows). However, the cells started to form dense aggregates around 12 days and became more evident on day 15 and day 18 (**Figure 5.9A**, red arrows).

The cell quantification showed that the yields of QM7 cells cultured for 11 days and 18 days were both ~1.2 x 10^8 cell/mL (**Figure 5.9B**). The released day 11 cells had healthy morphologies. Live/dead cell staining showed that most cells were alive on day 11 with a few dead cells found (**Figure 5.10A**). The Live/Dead cell staining for the whole cell fiber indicates that the dead cells were mainly inside the multilayers, especially the dense area (**Figure 5.10A**, red arrows). The released day 18 cells showed more cell death by Live/Dead cell staining (**Figure 5.10B**). There were more and larger aggregates in the tubes, and the dead cells were mainly inside the aggregates (**Figure 5.10B**, red arrows). Because cell death significantly increased from day 11 to day 18, the yields were very similar even cells continued to grow from day 11 to day 18 (**Figure 5.9B**).

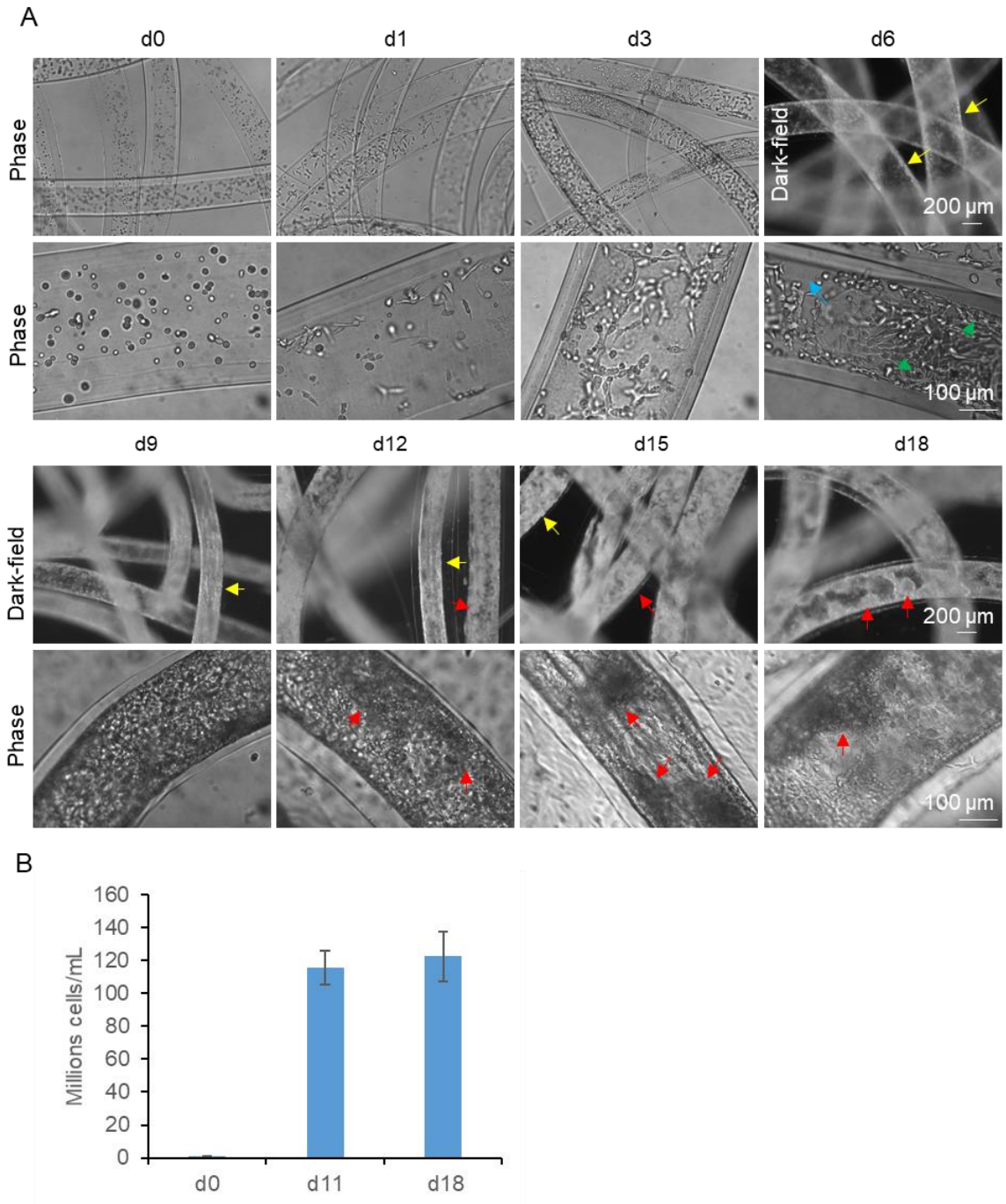

Figure 5.9. QM7 expansion in AlgTubes. (A) Phase or dark-field pictures of QM7 cells in AlgTubes on different days. (B) QM7 quantification on day 0, day 11 and day 18. Green arrows: multilayer cell masses; yellow arrows: 3D white cells mass; red arrows: dense aggregates.

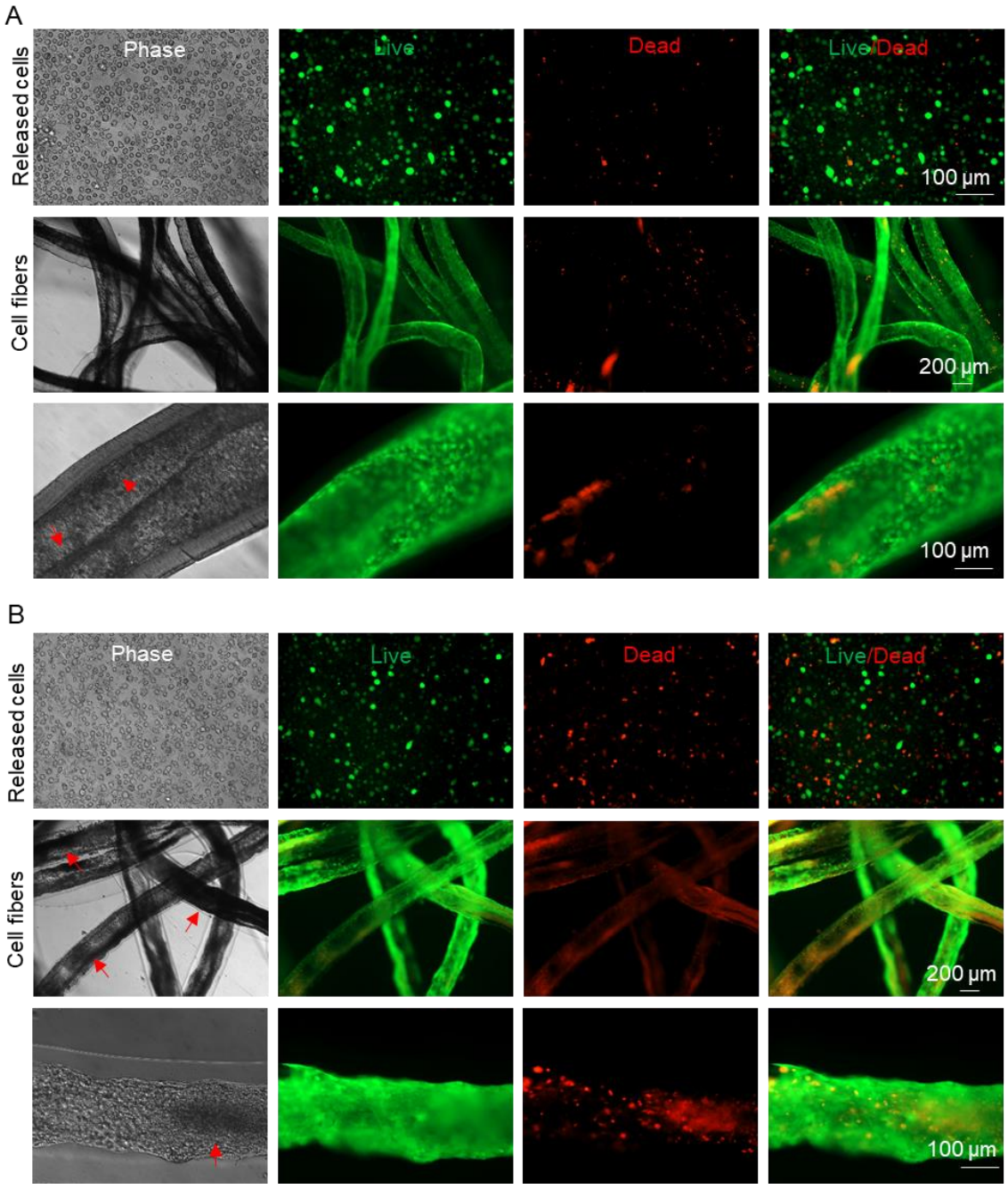

Figure 5.10. Live/Dead cell staining of QM7 cultured in AlgTubes on day 11 (A) and day 18 (B).

Quail cell differentiation in AlgTubes

Before initiating differentiation, quail cells were first expanded for 6 days and reached 80-90% confluence in AlgTubes (**Figure 5.11**). Cells continued to proliferate and formed 3D cell masses in the differentiation process. Myotubes could be seen after 3 days of differentiation (**Figure 5.11A**, blue arrows). Live/Dead cell staining indicates a slight decrease of dead cells than QM7 expansion only, but still significant dead cells. The dead cells were also mainly inside the large and dark aggregates (**Figure 5.11B**, red arrows). Immunostaining confirmed the formation of myotubes, which were aligned along the hydrogel tubes. The myotubes also expressed MyoD and PAX7, indicating the muscle differentiation of QM7 cells was promoted (**Figure 5.11C**). Compared to C2C12 cells, QM7 had more dead cells on day 18 both in expansion and differentiation. This could be due to the less adhesion to the hydrogel tubes and QM7 cells formed aggregates after being cultured for 11 days. Results in Figure 5.1 and Figure 5.8 show C2C12 and QM7 cells behaved differently in AlgTubes. C2C12 cells formed a confluent monolayer before forming 3D structures, while quail cells tended to form 3D cell aggregated. We asked if the AlgTubes caused the difference or it was the cells' intrinsic difference. We cultured and differentiated C2C12 and QM7 using the traditional 2D cell culture dishes (**Figure 5.12 and 5.13**). On day 5, both cells formed myotubes. On day 11, more myotubes were formed for C2C12 cells, while quail myotubes aggregated. The results show that AlgTubes did not alter cells' intrinsic programs.

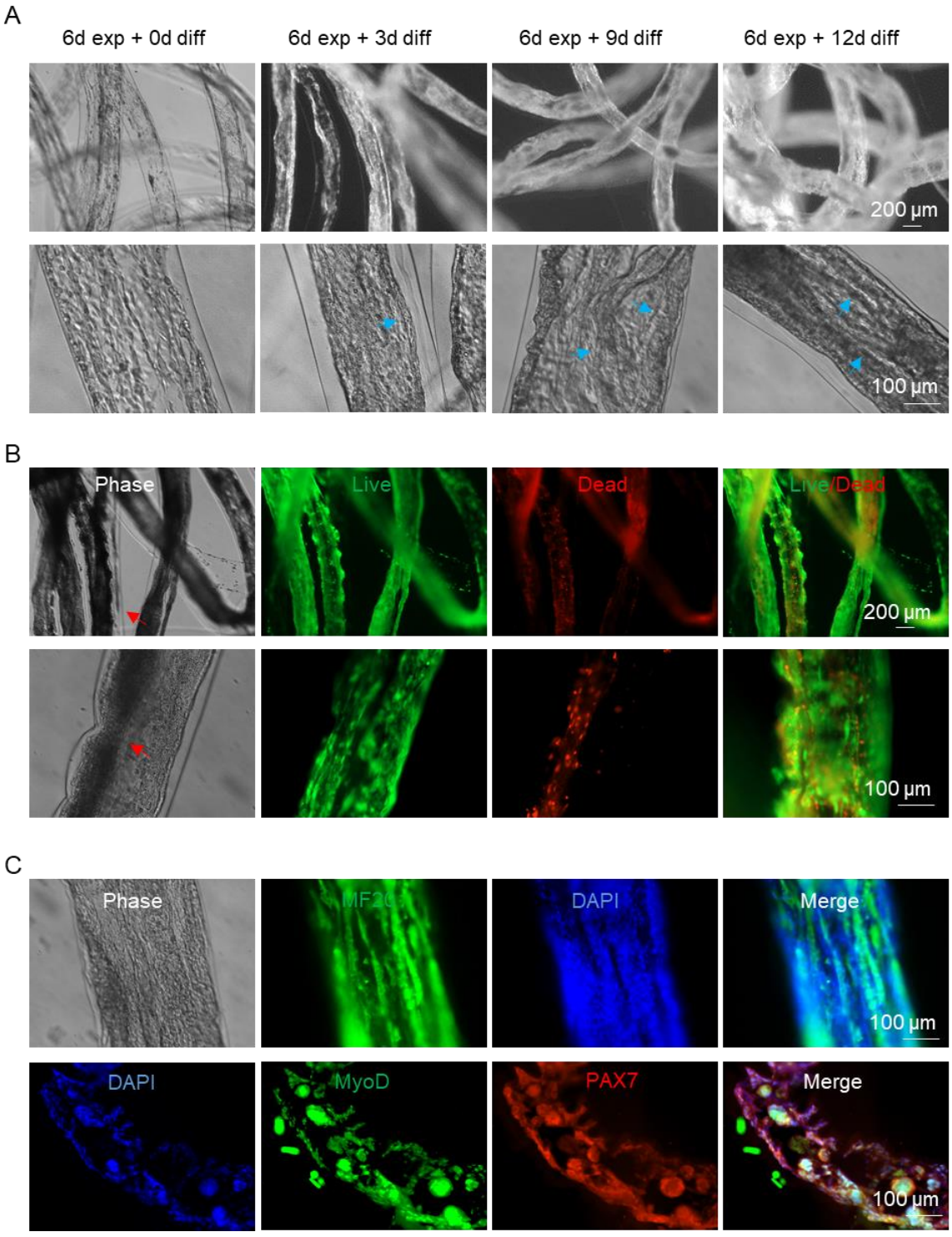

Figure 5.11. QM7 differentiation in AlgTubes. QM7 were first expanded for 6 days in AlgTubes before initiating differentiation. (A) Phase or dark-field pictures of QM7 differentiation in AlgTubes on different days. Day 18 cells were harvested for live/dead staining (B) and fixed for MF20, MyoD and PAX7 immunostaining (C). Blue arrows: Myotubes; red arrows: dead cells in aggregates.

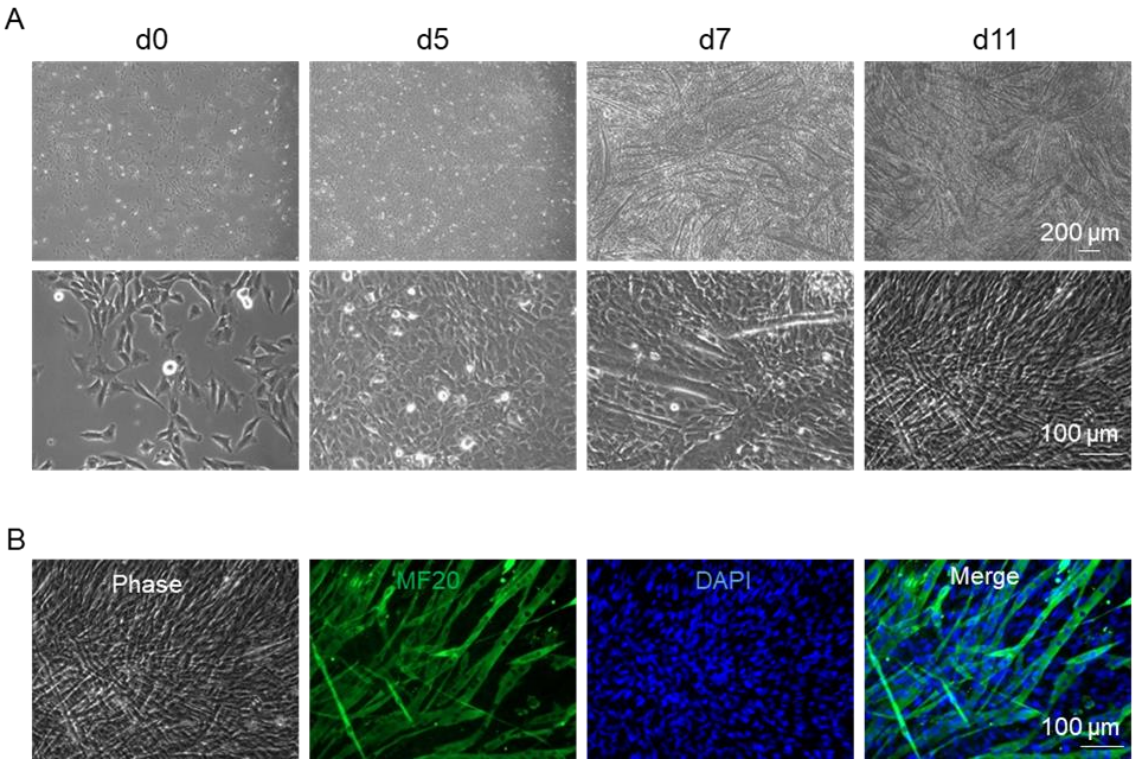

Figure 5.12. C2C12 differentiation in 2D culture. Differentiation started on day 2. (A) Phase images of 2D culture. (B) Immunostaining of MF20.

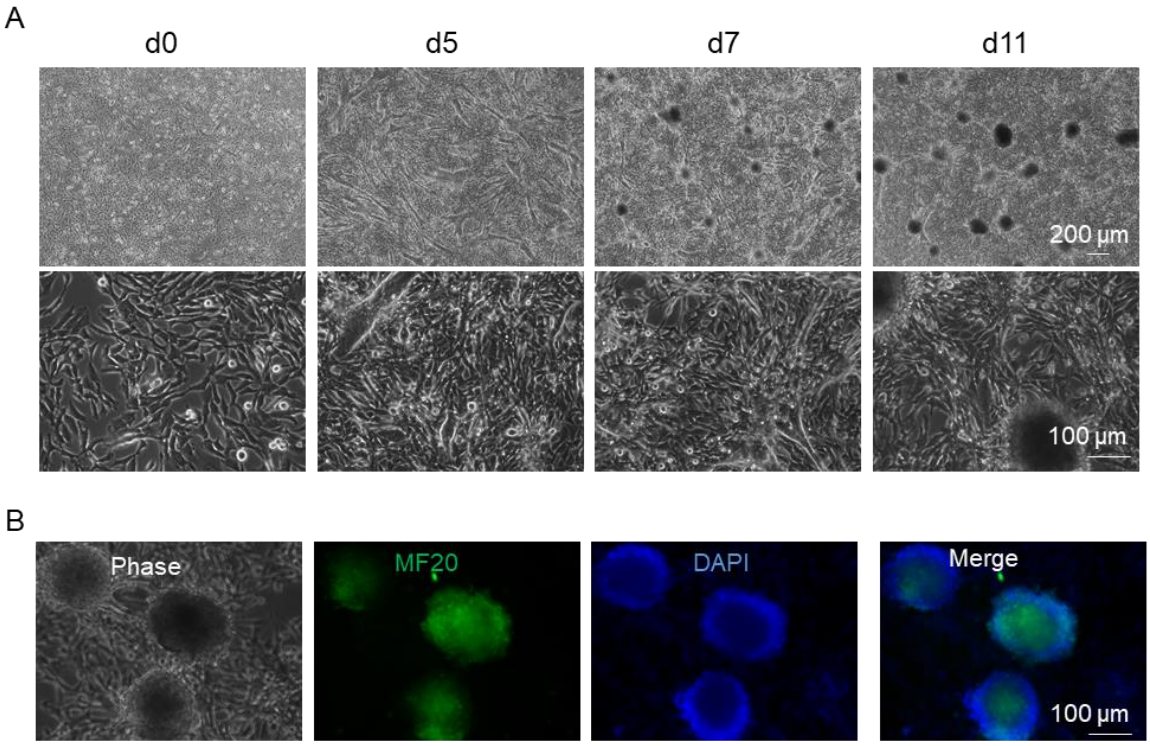

Figure 5.13. QM7 differentiation in 2D culture. Differentiation started on day 3. (A) Phase images of 2D culture. (B) Immunostaining of MF20.

QM7 and D1 cell co-culture

Similar to C2C12, we did the QM7 l and D1 cell co-culture. D1 cells did not alter the cell culture outcome significantly. For expansion, cells attached the inner surface of the hydrogel tubes after 24 hours without apparent cell death. Cells did not reach a confluent monolayer until multilayer cell masses were observed on day 6 **(Figure 5.14A**, green arrows). The dark-field images showed 3D multilayer cell masses from day 6 (**Figure 5.14A**, yellow arrows),). Cells started to form dense aggregates around 12 days and became more obvious on day 15 and day 18 (**Figure 5.14A**, red arrows). Live/dead staining still showed significant cell death on day 18 (**Figure 5.14B**). Like QM7 single culture, dead cells were mainly in the large and dense dark aggregates (**Figure 5.14B**, red arrows). Thus, D1 co-culture did not cause significant changes on QM7 and did not increase QM7 survival in the expansion medium.

We also evaluated if the D1 cells would increase the QM7 yield or differentiation in AlgTubes in the differentiation medium. QM7 and D1 cells were first expanded for 6 days in AlgTubes before initiating differentiation. QM7 cells continued to proliferate and formed white cell masses. Myotubes were formed after 6 days of differentiation (**Figure 5.15A**). However, significantly less cell death than the monoculture and co-culture in expansion medium was detected on day 18 (**Figure 5.15B**). The MF20 immunostaining confirmed the formation of myotubes. Most cells were MF20 positive(**Figure 5.15C**). Thus, D1 co-culture significantly increased QM7 survival in the differentiation medium.

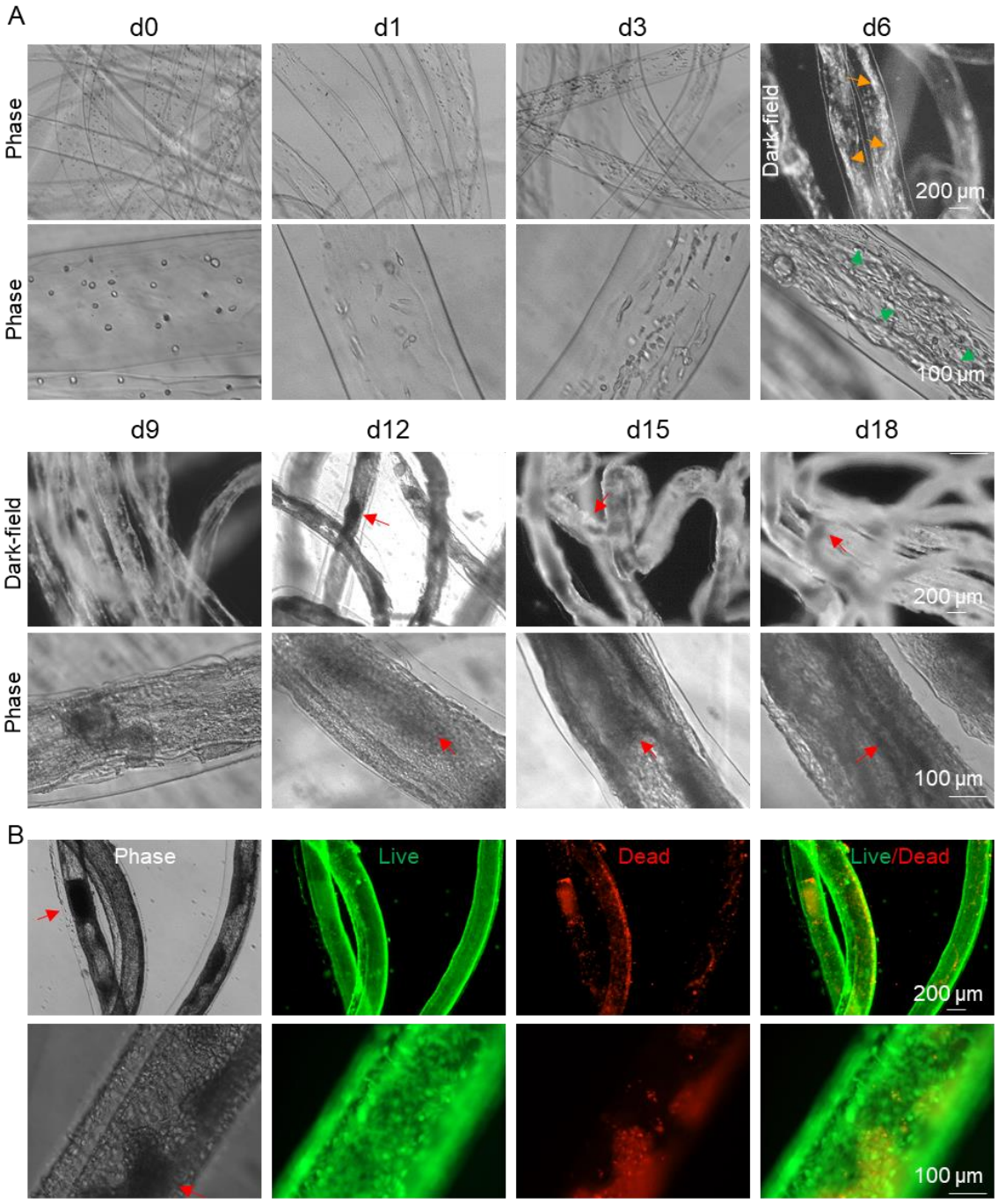

Figure 5.14. QM7 and D1 cells expansion in AlgTubes. (A) Phase or dark-field pictures of cells in AlgTubes on different days. (B) Live dead cell staining on day 18. Green arrows: multilayer cell masses; orange arrows: 3D white cells mass; red arrows: dense aggregates.

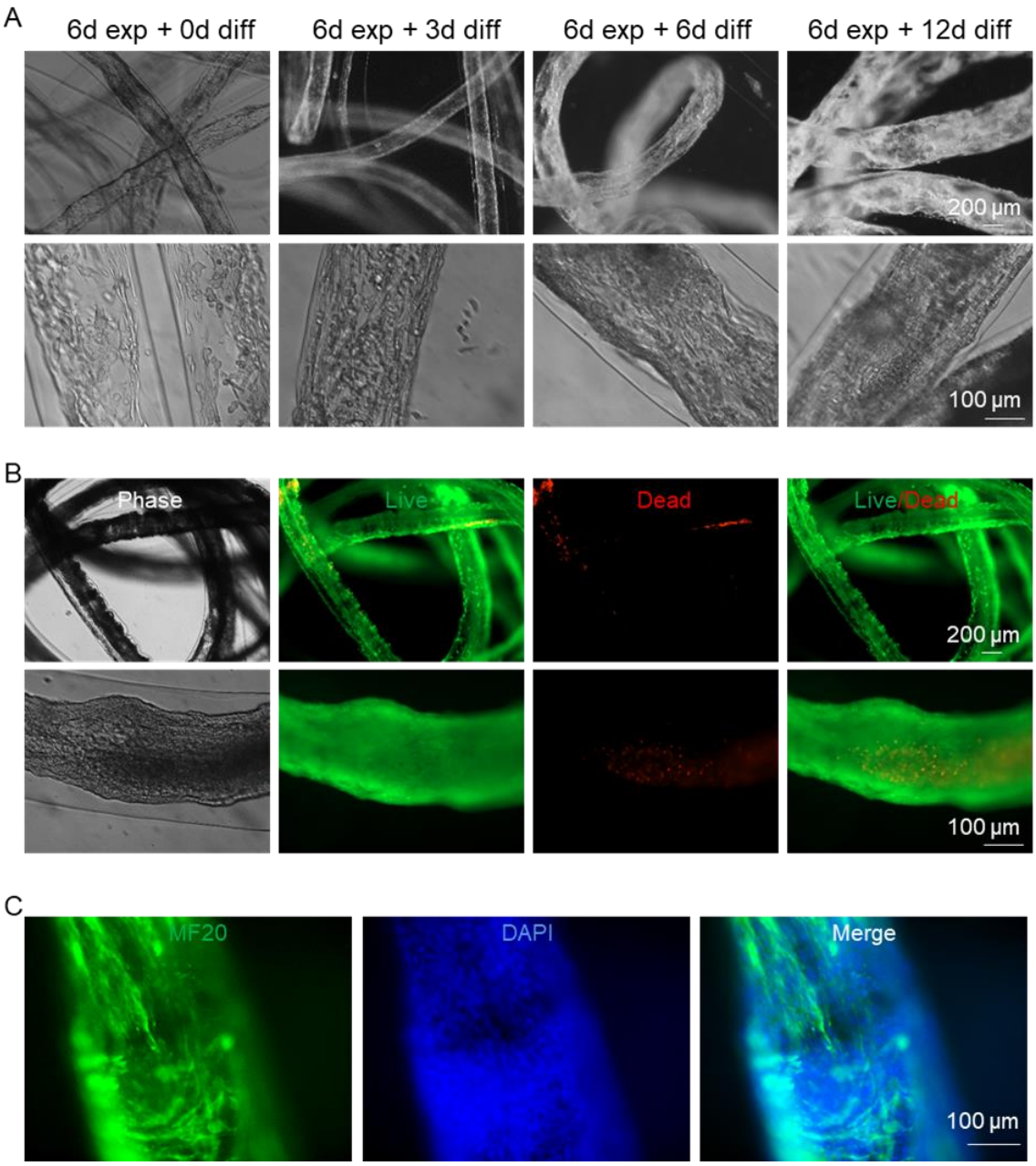

Figure 5.15. QM7 and D1 cell differentiation in AlgTubes. QM7 and D1 cells were first expanded for 6 days. (A) Phase or dark-field pictures of cells in AlgTubes on different days. Day 18 cells were harvested for live/dead staining (B) and fixed for MF20 immunostaining (C).

QM7 and 3T3 cell co-culture

Fibroblasts are another type of stromal cells that can boost the survival of other cell types. We thus did co-culture experiments to evaluate if mouse 3T3 fibroblasts could boost the growth rate and yield of QM7 in AlgTubes (**Figure 5.16**). Cells attached to the hydrogel tubes after seeded in the hydrogel tubes for 24 hours. On day 6, cells started to form multilayer cell masses before reaching a confluent monolayer (**Figure 5.16A**). Dense aggregates were formed after being cultured for 12 days and continued to increase (**Figure 5.16A**). Live/dead staining still showed significant cell death on day 18 (**Figure 5.16B**). Similar to QM7 monoculture, the dead cells were mainly in the large and dense dark aggregates (**Figure 5.16B**).

Differentiation was initiated after QM7 and 3T3 were co-cultured for 6 days in AlgTubes. QM7 cells continued to proliferate and formed white cell masses as shown in dark-field images. Myotubes can be seen after 6 days of differentiation (**Figure 5.17A**, blue arrows), while dense and dark aggregates were formed. Significant cell death in the aggregates was still shown by Live/Dead cell staining on day 18 (**Figure 5.17B**). Cells were harvested and fixed for immunostaining. Most cells were MF20 positive, which confirmed the formation of myotubes. The myotubes are also expressed high percentages of MyoD and PAX7 (**Figure 5.17C**). Thus, 3T3 co-culture did not cause significant changes on QM7.

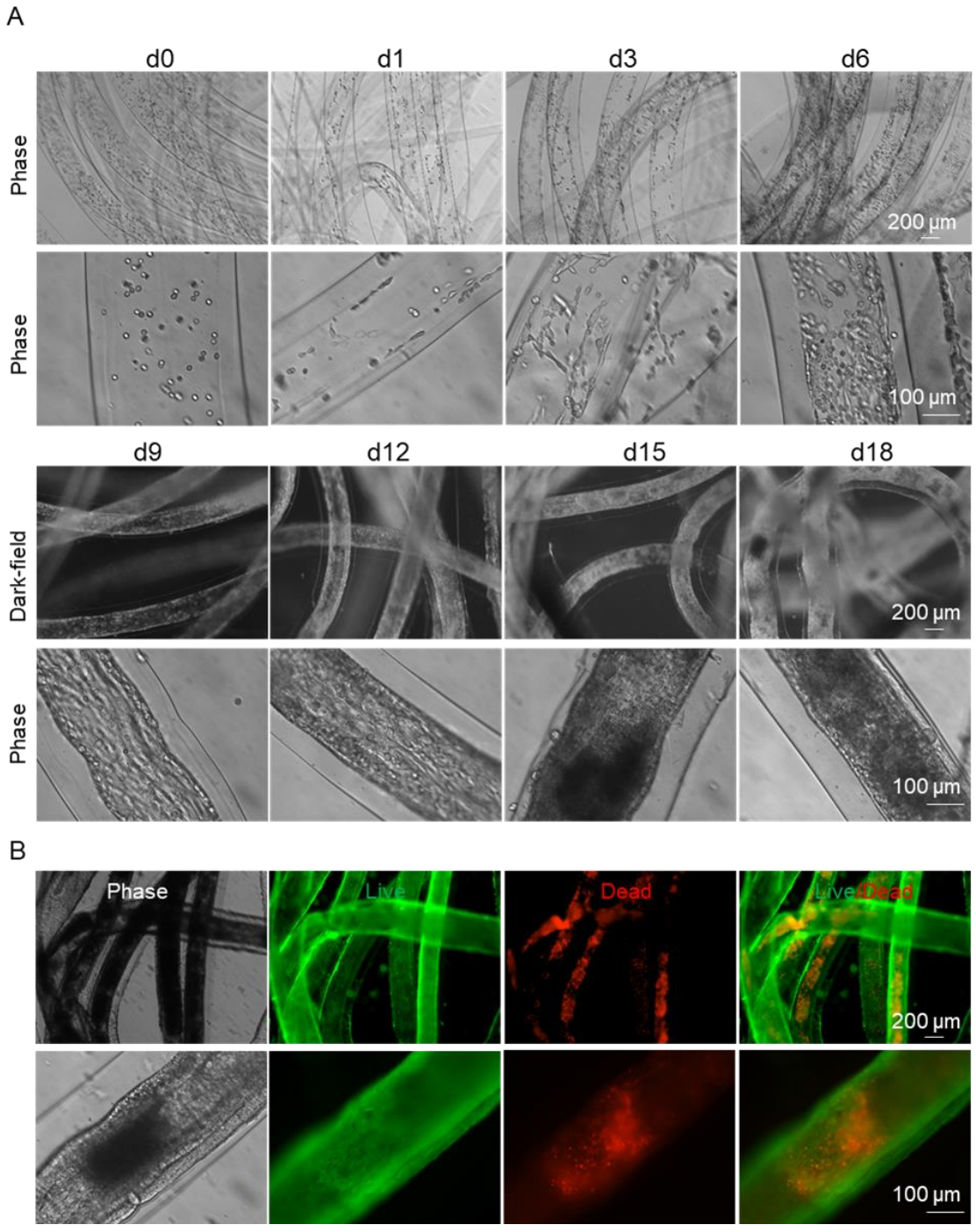

Figure 5.16. QM7 and 3T3 cells expansion in Alg-RGD-Tubes. (A) Phase or dark-field pictures of cells in AlgTubes on different days. (B) Live dead cell staining on day 18.

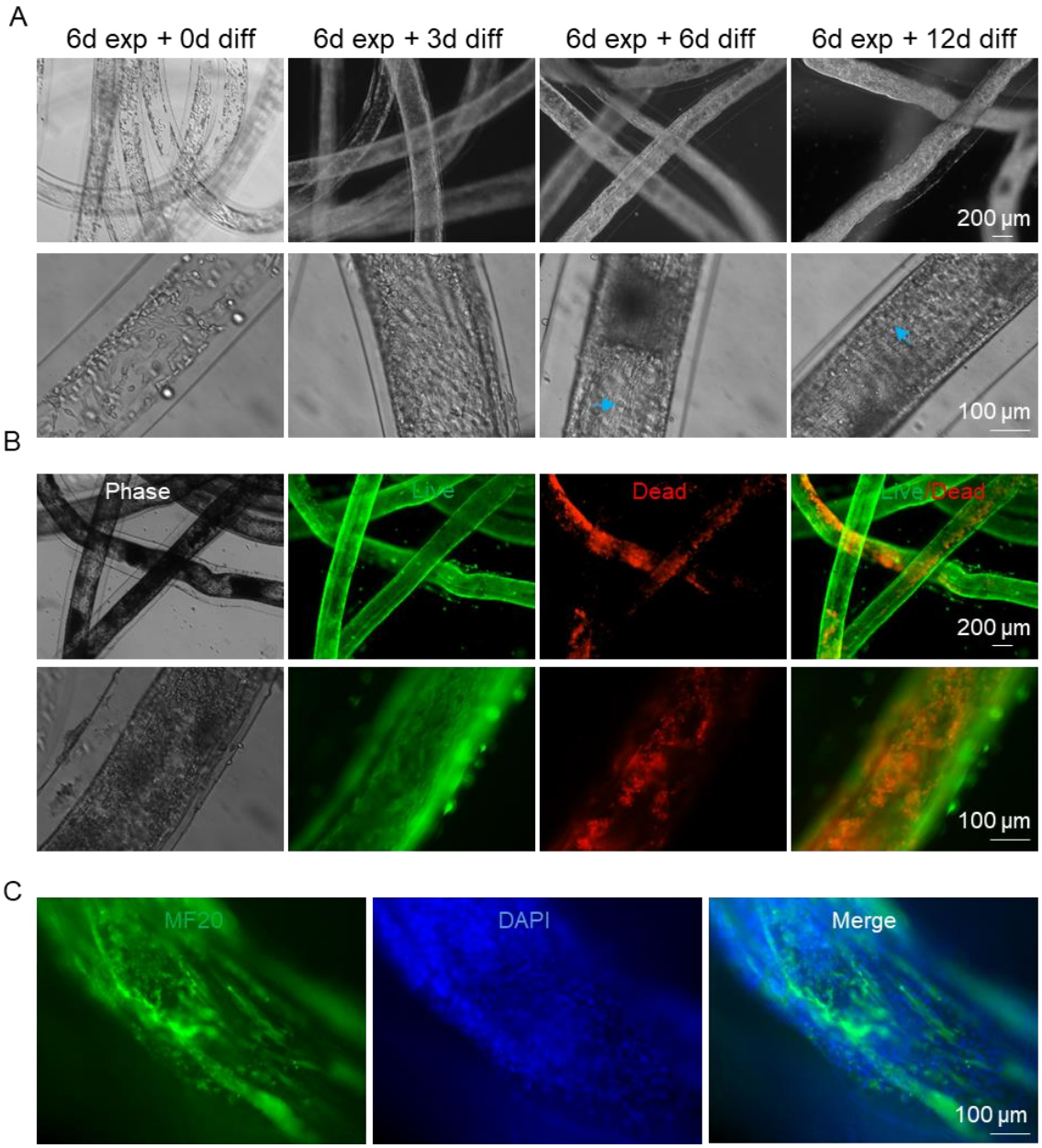

Figure 5.17. QM7 and 3T3 cells differentiation in AlgTubes. QM7 and D1 cells were first expanded for 6 days in AlgTubes before initiating differentiation. (A) Phase or dark-field pictures of cells in AlgTubes on different days. Day 18 cells were harvested for live/dead staining (B) and fixed for MF20 immunostaining (C).

Quantification of QM7 monoculture and co-culture

To quantify the QM7 growth rate further, we harvested and digested the cells in the hydrogel tubes on day 18 and then used the Countless II cell counter to count the cells (**Figure 5.18**). We achieved a final yield of about 1.2 $x10^8$ cells/mL hydrogel tubes on day 18 without differentiation and reached about 1.3$x10^8$ cells/mL hydrogel tubes on day 18 with differentiation. When co-cultured with D1 cells, the yield was similar to QM7 monoculture without differentiation, which is ~1.15 $x10^8$ cells/mL. However, D1 cell co-culture and differentiation significantly increased the yield to ~1.9 $x10^8$ cells/mL, which corresponds to the Live/Dead cell staining. When QM7 cells were co-cultured with D1 cells in the differentiation medium, significantly fewer dead cells were detected (**Figure 5.15B**). When QM7 cells were co-cultured with 3T3 cells, the expansion yield improved to ~1.45 $x10^8$ cells/mL, though there is no statistical difference. Moreover, differentiation did not change the yield, which is also ~1.1 $x10^8$ cells/mL. Overall, the QM7 cells in the AlgTubes can achieve a final yield of more than 1.1 $x10^8$ cells/mL. If we want less cell death, we can culture the QM7 cells only for 11 days per passage before large and dense aggregates are formed. If a long-term culture with a higher yield is expected, the alginate tubes could be modified with higher RGD concentration or higher stiffness.

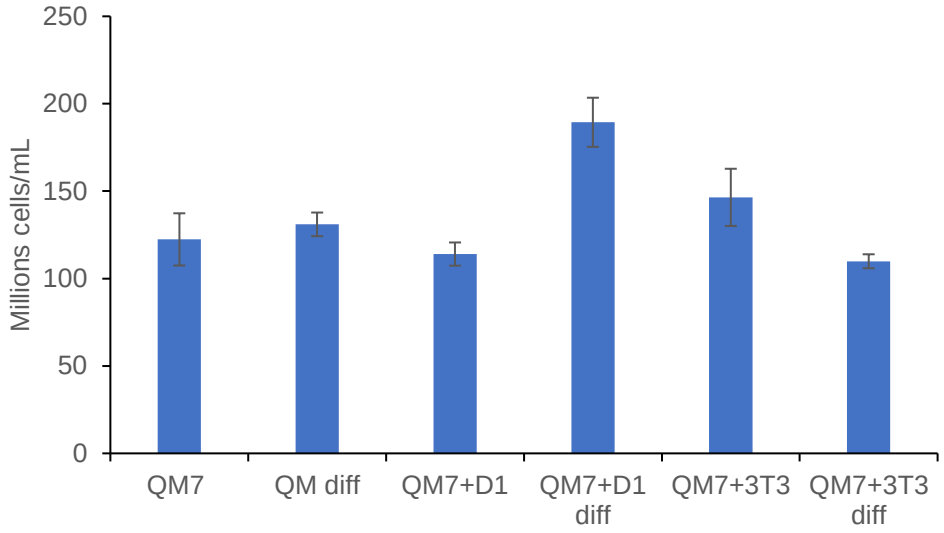

Figure 5.18. Quantifications of QM7 cultured under different conditions in AlgTubes on day 19.

X9 expansion in Alg Tubes

Adipocytes are another main type of cell in meat. Thus, we used the mouse pre-adipocyte X9 to examine if our system could produce a large number of pre-adipocytes or adipocytes (**Figure 5.19)**. X9 cells were seeded with a low density (1 x10^6 cells/mL). After 24 hours, most cells were attached to the hydrogel tube wall with no cell death. Unlike C2C12 and QM7, X9 cells expanded very slowly. The cell numbers in day 3 images were very similar to day 1. A confluent monolayer had yet formed even after 10 days. After 13 days, most areas were confluent, and few multilayer cell masses were seen (**Figure 5.19A**, green arrows). However, even after 19 days of culture, most hydrogel tubes' inner surface areas were still a single layer of X9 cells, and no large cell mass was seen (**Figure 5.19A**). The yield of X9 cells was 3.5 x10^6 cells/mL on day 19(**Figure 5.19B**). The Live/Dead cell staining on day 19 showed most cells were live cells with few dead cells were detected

(**Figure 5.19C**). Although X9 cells expanded slowly in AlgTubes, the cells did grow in the hydrogel tubes and without significant cell death.

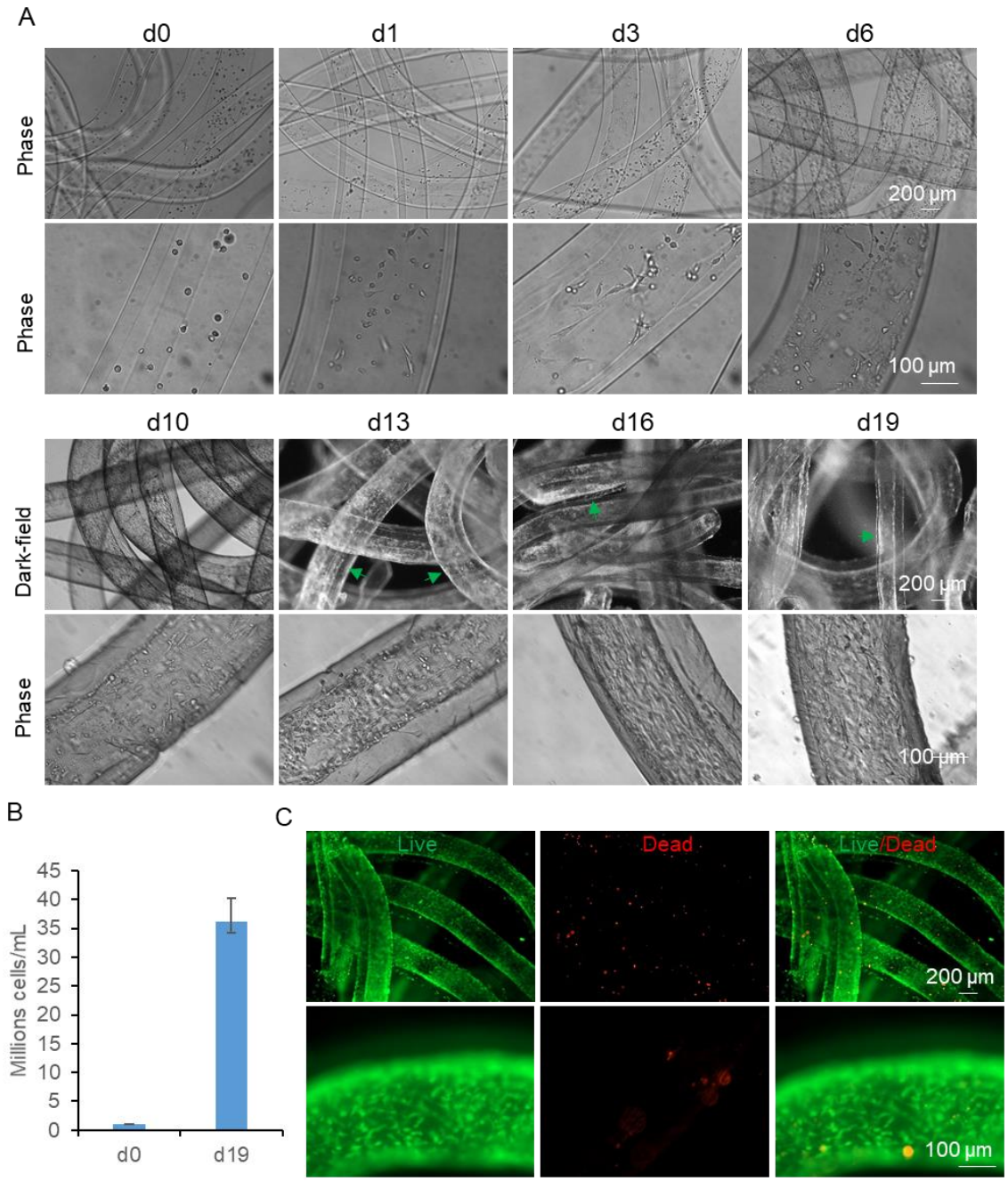

Figure 5.19. X9 cells expansion in AlgTubes. (A) Phase or dark-field pictures of X9 cells on different days. (B) Cell quantification in alginate tubes on day 0 and day 19. (C) Live/Dead cell staining on day 19.

Discussion and Conclusion

Large numbers of cells are needed for meat production. Additionally, the cost of cell production should be low so the final meat can be commercially viable. Current cell culture methods cannot meet this need. Due to its enormous success in culturing Chinese hamster ovary cells for producing protein therapeutics, 3D suspension culturing (e.g., a stirred-tank bioreactor), which suspends and cultures cells in an agitated medium, are being studied to scale up mammalian cell production[19,20]. However, several critical problems limit its success[21–25]. First, most mammalian cells have strong cell-cell interactions[26,27], making them aggregate to form large cell agglomerates (i.e., agglomeration)[28–30]. The mass transport to cells located at the center of large agglomerates (e.g., >400 μm diameter, the diffusion limit in tissue) becomes insufficient, leading to slow cell growth, apoptosis, and uncontrolled differentiation[30,31]. Second, the agitation generates hydrodynamic conditions (e.g., the medium flow direction, velocity, shear force, and chemical environment) that vary spatially and temporally, resulting in locations with critical shear stress (e.g., near the vessel wall) that induce large cell death[28–30]. We[24,25] and others[21–23] show cells typically expand less than 10-fold per passage to yield less than $5x10^6$ cells/mL in 3D suspension culturing. These cells occupy <1% of the culture volume[25].

Third, the hydrodynamic conditions are highly variable and sensitive to many factors, including bioreactor design (e.g., impeller geometry, size, and position; vessel geometry and size; positions of probes for pH, temperature, and oxygen), medium viscosity, and agitation rate[30,32]. They are currently not well understood and are hard to control[28–30,32]. Additionally, different cell types respond to hydrodynamic conditions differently[28–30].

These result in significant culture variations between batches and cell lines and difficulty in scaling up. For instance, in recent studies to make hPSC-CMs from two hPSC lines in suspension culturing, the yield varied from 40 million to 125 million cells. The product purity varied from 28% to 88% in different batches (100 mL culture volume)[33,34]. When the culture was scaled from ~100 mL to ~1,000 mL, the yield and differentiation efficiency was significantly altered, and re-optimization was required[33,34]. These indicate the challenge of further scaling up (e.g., hundreds of liters) since optimizing multiple factors in a large volume is costly.

We and others have cultured cells in hydrogels with the intention of using hydrogels as physical barriers to eliminate cell agglomeration and shear stress[35–38], but cells have slow growth in most hydrogels. We speculate it is due to several factors: (1) the hydrogels hinder the initial cellular interactions required for their survival after cell passaging, and (2) cells must degrade or deform the scaffold to create spaces for the new cells. Significantly, we found a very soft thermoreversible hydrogel that enabled high yield (~2.0×10^7 cells/mL)[24,25,39–41]. However, this hydrogel is unsuitable for large-scale cell production because the material is expensive and highly variable between batches.

In this study, we showed that our AlgTubes could support both expansion and differentiation of mouse and quail myoblasts. The yield reached ~1.5×10^8 cells/mL. To our best knowledge, this is the first time to achieve a volumetric yield above 100 million per ml culture volume. More importantly, the AlgTubes system is scalable. We believe this system is appropriate for meat production and will significantly impact this emerging field.

Reference

1. Fernández-Ruiz, I. Stem cells: Cell therapy improves outcomes in heart failure. *Nature Reviews Cardiology* vol. 13 (2016).

2. Aiking, H. Protein production: Planet, profit, plus people? *Am. J. Clin. Nutr.* **100**, 483–489 (2014).

3. Ryschawy, J. *et al.* Review: An integrated graphical tool for analysing impacts and services provided by livestock farming. *Animal* **13**, 1760–1772 (2019).

4. Willett, W. *et al.* Food in the Anthropocene: the EAT–Lancet Commission on healthy diets from sustainable food systems. *Lancet* **393**, 447–492 (2019).

5. Gerber, P. J., Mottet, A., Opio, C. I., Falcucci, A. & Teillard, F. Environmental impacts of beef production: Review of challenges and perspectives for durability. *Meat Sci.* **109**, 2–12 (2015).

6. Aleksandrowicz, L., Green, R., Joy, E. J. M., Smith, P. & Haines, A. The impacts of dietary change on greenhouse gas emissions, land use, water use, and health: A systematic review. *PLoS One* **11**, 1–16 (2016).

7. Treich, N. Cultured Meat: Promises and Challenges. *Environ. Resour. Econ.* **79**, 33–61 (2021).

8. Bryant, C. J. Culture, meat, and cultured meat. *J. Anim. Sci.* **98**, 1–7 (2020).

9. Hong, T. K., Shin, D. M., Choi, J., Do, J. T. & Han, S. G. Current issues and

technical advances in cultured meat production: A review. *Food Sci. Anim. Resour.* **41**, 335–372 (2021).

10. Lin, H. *et al.* Automated Expansion of Primary Human T Cells in Scalable and Cell-Friendly Hydrogel Microtubes for Adoptive Immunotherapy. *Adv. Healthc. Mater.* **7**, 1701297 (2018).

11. Lin, H. *et al.* Engineered Microenvironment for Manufacturing Human Pluripotent Stem Cell-Derived Vascular Smooth Muscle Cells. *Stem Cell Reports* **12**, 84–97 (2019).

12. Lin, H. *et al.* Integrated generation of induced pluripotent stem cells in a low-cost device. *Biomaterials* **189**, 23–36 (2019).

13. Lin, H. *et al.* Hydrogel-Based Bioprocess for Scalable Manufacturing of Human Pluripotent Stem Cell-Derived Neural Stem Cells. *ACS Appl. Mater. Interfaces* **10**, 29238–29250 (2018).

14. Li, Q. *et al.* Scalable and physiologically relevant microenvironments for human pluripotent stem cell expansion and differentiation. *Biofabrication* **10**, 025006 (2018).

15. Lin, H. *et al.* Manufacturing human pluripotent stem cell derived endothelial cells in scalable and cell-friendly microenvironments. *Biomater. Sci.* **7**, 373–388 (2019).

16. Li, Q. *et al.* Scalable Culturing of Primary Human Glioblastoma Tumor-Initiating Cells with a Cell-Friendly Culture System. *Sci. Rep.* **8**, 3531 (2018).

17. Wang, O. & Lei, Y. Creating a cell-friendly microenvironment to enhance cell culture efficiency. *Cell Gene Ther. Insights* **5**, 341–350 (2019).

18. Yu, Y. & Chau, Y. One-step 'click' method for generating vinyl sulfone groups on hydroxyl-containing water-soluble polymers. *Biomacromolecules* **13**, 937–942 (2012).

19. Polak, J. M. & Mantalaris, S. Stem cells bioprocessing: An important milestone to move regenerative medicine research into the clinical arena. *Pediatric Research* vol. 63 (2008).

20. Serra, M., Brito, C., Correia, C. & Alves, P. M. Process engineering of human pluripotent stem cells for clinical application. *Trends Biotechnol.* **30**, 350–358 (2012).

21. Denning, C. *et al.* Cardiomyocytes from human pluripotent stem cells: From laboratory curiosity to industrial biomedical platform. *Biochim. Biophys. Acta - Mol. Cell Res.* **1863**, 1728–1748 (2016).

22. Kempf, H., Andree, B. & Zweigerdt, R. Large-scale production of human pluripotent stem cell derived cardiomyocytes. *Adv. Drug Deliv. Rev.* **96**, 18–30 (2016).

23. Hartman, M. E., Dai, D. & La, M. A. Human pluripotent stem cells: prospects and challenges as a source of cardiomyocytes for in vitro modeling and cell-based cardiac repair. *Adv. Drug Deliv. Rev.* **96**, 3–17 (2016).

24. Lei, Y., Jeong, D., Xiao, J. & Schaffer, D. V. Developing Defined and Scalable 3D Culture Systems for Culturing Human Pluripotent Stem Cells at High Densities. *Cell Mol Bioeng* **7**, 172–183 (2014).

25. Lei, Y. & Schaffer, D. V. A fully defined and scalable 3D culture system for human pluripotent stem cell expansion and differentiation. *Proc. Natl. Acad. Sci. U. S. A.* **110**, E5039-48 (2013).

26. Chen, K. G. *et al.* Developmental insights from early mammalian embryos and core signaling pathways that influence human pluripotent cell growth and differentiation. *Stem Cell Res.* **12**, 610–621 (2014).

27. Chen, K. G., Mallon, B. S., McKay, R. D. G. & Robey, P. G. Human pluripotent stem cell culture: considerations for maintenance, expansion, and therapeutics. *Cell Stem Cell* **14**, 13–26 (2014).

28. Kinney, M. A., Sargent, C. Y. & Mcdevitt, T. C. The multiparametric effects of hydrodynamic environments on stem cell culture. *Tissue Eng. Part B* **17**, 249–262 (2011).

29. Fridley, K. M., Kinney, M. A. & McDevitt, T. C. Hydrodynamic modulation of pluripotent stem cells. *Stem Cell Res. Ther.* **3**, 45 (2012).

30. Kropp, C., Massai, D. & Zweigerdt, R. Progress and challenges in large-scale expansion of human pluripotent stem cells. *Process Biochem.* **59**, 244–254 (2017).

31. Hajdu, Z. *et al.* Tissue spheroid fusion-based in vitro screening assays for analysis

of tissue maturation. *J. Tissue Eng. Regen. Med.* **4**, 659–664 (2010).

32. Ismadi, M., Gupta, P., Fouras, A., Verma, P. & Jadhav, S. Flow characterization of a spinner flask for induced pluripotent stem cell culture application. *PLoS One* **9**, e106493 (2014).

33. Jara-avaca, M. *et al.* Controlling expansion and cardiomyogenic differentiation of human pluripotent stem cells in scalable suspension culture. *Stem cell reports* **3**, 1132–1146 (2014).

34. Chen, V. C. *et al.* Development of a scalable suspension culture for cardiac differentiation from human pluripotent stem cells. *Stem Cell Res.* **15**, 365–375 (2015).

35. Serra, M. *et al.* Microencapsulation technology: a powerful tool for integrating expansion and cryopreservation of human embryonic stem cells. *PLoS One* **6**, e23212 (2011).

36. Chayosumrit, M., Tuch, B. & Sidhu, K. Alginate microcapsule for propagation and directed differentiation of hESCs to definitive endoderm. *Biomaterials* **31**, 505–514 (2010).

37. Stenberg, J. *et al.* Sustained embryoid body formation and culture in a non-laborious three dimensional culture system for human embryonic stem cells. *Cytotechnology* **63**, 227–237 (2011).

38. Gerecht, S. *et al.* Hyaluronic acid hydrogel for controlled self-renewal and

differentiation of human embryonic stem cells. *Proc. Natl. Acad. Sci. U. S. A.* **104**, 11298–11303 (2007).

39. Lin, H., Li, Q. & Lei, Y. Three-dimensional tissues using human pluripotent stem cell spheroids as biofabrication building blocks. *Biofabrication* **9**, 025007 (2017).

40. Lin, H., Li, Q. & Lei, Y. An Integrated Miniature Bioprocessing for Personalized Human Induced Pluripotent Stem Cell Expansion and Differentiation into Neural Stem Cells. *Sci. Rep.* **7**, 40191 (2017).

41. Li, Q. *et al.* Scalable production of glioblastoma tumor-initiating cells in 3 dimension thermoreversible hydrogels. *Sci. Rep.* **6**, 31915 (2016).

CHAPTER 6. CREATING A CELL-FRIENDLY MICROENVIRONMENT TO ENHANCE THE CELL CULTURE EFFICIENCY

The need for more efficient cell culture technologies

A number of cellular therapeutics have been approved and hundreds of clinical trials are on-going. Cells will be a major type of medicine in the future. Human cells are also needed in large amounts for disease modeling, drug discovery and tissue engineering. To achieve the full potential of cellular therapeutics, we must be able to cost-effectively and reproducibly manufacture cells at large scales and with high quality[1]. Cells can be prepared and used as off-the-shelf products (i.e. allogenic cells). Allogenic cells have relatively low production cost, high quality control, and are available when patients need them. The commercial success of allogenic cellular therapeutics relies on a technology that can culture massive numbers of cells per batch (e.g. 10^{12} to 10^{13} cells per batch)[2–4]. Alternatively, autologous cells can be prepared for personalized treatment. Autologous cells have minimal immune rejection but their production cost is high and the production variation between patients is significant[5–10]. The commercial success of autologous cells requires a technology that can consistently culture cells for thousands of patients in parallel with affordable cost[11]. Currently, robust and cost-effective culture of high-quality allogenic or autologous cells in large scales is still very challenging[1,12,13]. Significant problems associated with the large-scale cell culture including the low cell yield, low scalability, high cost, large culture variation, and significant genetic and phenotypic changes. A healthy growth of cell therapy industry needs innovations and breakthroughs on cell culture technologies. This article will use human pluripotent stem cells (hPSCs) as examples to

show the critical need of creating a cell-friendly microenvironment during large-scale cell culture. Though different cell types require different microenvironments, the principles and technologies discussed in this article are suitable for other cell types.

Current cell culture technologies cannot provide a cell-friendly microenvironment

In vivo, most of our cells reside in a 3D microenvironment with abundant cell-to-cell, cell-to-matrix interactions, local growth factors, autocrine and paracrine signaling, which collectively regulate the cell survival, growth, differentiation and functions (**Figure 6.1**). In most of human tissues, the cellular microenvironment is soft and elastic. There are dense blood vessels to efficiently transport oxygen, nutrients, growth factors and metabolic wastes. The diffusion limit in human tissue is typically less than a few hundreds of micrometers. In most of human tissues, cells experience minimal hydrodynamic stresses. The cellular microenvironments of current cell culture methods are very different from this in vivo 3D microenvironment:

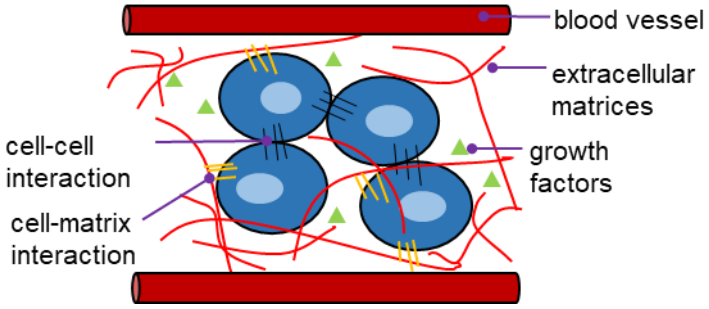

Figure 6.1. The 3D cellular microenvironment in vivo.

The two-dimensional (2D) cell culture method

Culturing cells on 2D surfaces is widely practiced. However, a 2D environment is very different from cells' *in vivo* 3D environment (**Figure 6.2**). In 2D culture, cells are polarized and the cell-to-cell and cell-to-matrix interactions and local growth factors are considerably reduced. The apical surfaces of cells are free while the bottom surfaces are attached to a substrate, which is typically very stiff. To adapt to this physiologically-irrelevant microenvironment, cells change their genetics and phenotypes[14–17]. Cells that adapt well proliferate and gradually take over the culture. For instance, research shows 34% hPSC lines that have been cultured in 2D culture for long-term have large chromosomal abnormalities[14–19]. Additionally, 2D culturing has low yield and is labor-, space-, and reagent-consuming. 2D culturing is generally considered suitable for preparing low-scale cells[20].

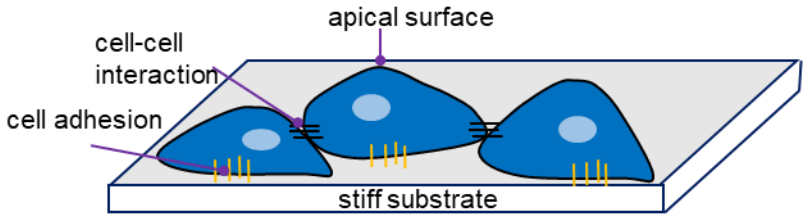

Figure 6.2. The two-dimensional (2D) cell culture method

The three-dimensional (3D) suspension culture method

Due to its enormous success for culturing protein-producing cells (e.g. Chinese hamster ovary or CHO cells), 3D suspension culturing (e.g., in a stirred-tank bioreactor), which suspends and cultures cells in an agitated medium, has been extensively studied to scale up the cell cutlure[21,22]. However, there are still several critical problems with the cellular microenvironment of this system (**Figure 6.3**)[2–4,23,24]. **First**, most human cells have strong cell-cell interactions[25,26] that make them aggregate to form large agglomerates[27–29]. The mass transport to cells located at the center of agglomerates larger than the diffusion limit becomes insufficient, leading to slow cell growth, apoptosis, and uncontrolled differentiation[29,30]. **Second**, the agitation generates hydrodynamic conditions (e.g., the medium flow direction, velocity, shear force, and chemical environment) that vary spatially and temporally, resulting in locations with critical hydrodynamic stresses (e.g., near the vessel wall) that induce large cell death. These factors lead to low cell expansion per passage and low volumetric yield[27–29]. For instance, hPSCs typically expand less than 10 folds every passage (about 4 to 10 days) to yield ~2.0x to $5x10^6$ cells/mL in 3D suspension culturing[2–4,23,24] These cells occupy <1% of the culture volume[24]. **Third**, the hydrodynamic conditions are highly variable and sensitive to many factors, including the bioreactor design (e.g., the impeller geometry, size, and position; vessel geometry and size; positions of probes for pH, temperature, and oxygen), medium viscosity, and agitation rate[29,31]. Reproducibly and precisely controlling the hydrodynamic conditions is challenging. Additionally, different cell types respond to hydrodynamic conditions differently[27–29]. These contribute to the large culture variations between batches and cell lines. For instance,

in recent studies to make cardiomyocytes from hPSCs in suspension culturing, the yield varied from 40 million to 125 million cells and the product purity varied from 28% to 88% in different batches (100 mL culture volume)[32,33]. When the culture was scaled from ~100 mL to ~1,000 mL, the yield and differentiation efficiency were significantly altered, requiring re-optimization[32,33]. These indicate the challenge of further scaling up (e.g., hundreds of liters), since optimizing multiple factors in a large volume is costly. Additionally, the shear stress and hydrodynamic variations become more severe at large scales, leading to more cell death and production variations[27–29,31]. Moreover, aeration (i.e., bubbling the medium with oxygen), which is required to meet the oxygen supply needs of large cultures, also causes significant cell death[34].

Cells can also be cultured on microcarriers suspended in a bioreactor[35]. This method also has the cell aggregation, shear-force induced cell death, hydrodynamic variation and scale up problems. The volumetric yield is also low. Using microcarriers also has some of the problems associated with 2D culture, such as the cell polarity and the stiff substrate-induced cell changes. During the harvest, detaching cells from microcarriers using enzymes and mechanical force, and separating the dissociated cells from microcarriers at large scale re both very challenging.

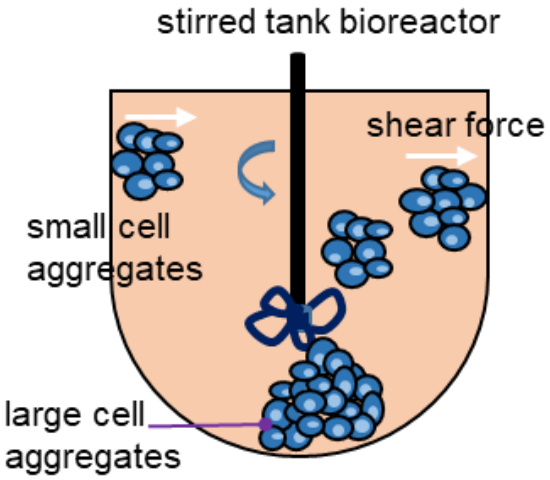

Figure 6.3. The three-dimensional (3D) suspension culture method

The hollow fiber cell culture method

Polymer hollow fibers have been used for culturing cells[36–38]. This method mimics the in vivo circulation and can generate high volumetric yield. However, it also has some critical problems with the microenvironment. The dense cells consume oxygen and nutrients at a fast rate, thus the composition of culture medium along the hollow fibers (e.g. at the entrance and exit of hollow fibers) are expected to be different. Consequently, cells at different locations face very different microenvironment. Additionally, cells adhere to the fibers, and harvesting cells typically takes tens of minutes enzymatic treatment to detach cells from the fibers. This treatment can lead to large cell death.

Culture cells in hydrogels

Scientists have cultured cells in hydrogels with the intention of using hydrogel scaffolds to eliminate cell agglomeration and hydrodynamic stresses[39–42]. However, cells typically have moderate growth rate and volumetric yield in hydrogels[23,24,43–45]. First, the scaffolds prevent the initial cellular interactions required for the survival of some cell types after cell passaging. Second, the scaffolds constrain cells. Cells have to degrade or deform the scaffolds to create spaces for the new born cells. In summary, current cell culture methods have not been designed to provide cells a well-controlled and friendly microenvironment, and consequently, the cell culture efficiency is not satisfactory.

Creating a cell-friendly microenvironment can significantly improve the culture outcome

Recently, researchers developed scalable and dissolvable micro-bioreactors that can create a cell-friendly and 3D microenvironment for cell cutlure[46–52]. Specifically, cells are cultured in microscale hollow tubes made with alginate hydrogel (i.e., AlgTubes)[46–52]. To process hydrogel tubes, a cell solution and an alginate solution are pumped into the central channel and side channel of a micro-extruder, respectively, to form coaxial core-shell flows that are extruded into a $CaCl_2$ buffer. The shell alginate flow is instantly crosslinked by Ca^{2+} ions to generate a hydrogel tube, and cells are grown in the tube. The tube's diameter and shell thickness can be precisely controlled by adjusting the nozzle diameter and the ratio of the shell and core flows. Typically, a shell thickness <40 μm and tube diameter <400 μm can ensure efficient mass transport and are appropriate for culturing cells. The tubes can be dissolved with the cell-compatible ethylenediaminetetraacetic acid solution (EDTA, 0.5 mM) in five minutes at room temperature to harvest the cells for the next passage or applications.

This system is designed to provide cells a friendly microenvironment (**Figure 6.4 and 6.5**). First, oxygen, nutrients and macromolecules (with Mw up to 700 kDa) can freely and quickly diffuse through the hydrogel shell. The hydrogel tubes direct cell expansion axially, while confining the radial diameter of cell masses within the diffusion limit (~400 μm) to ensure efficient mass transport. Second, the hydrogel tubes also isolate hydrodynamic stresses from cells, and lastly, the tubes provide free and uniform 3D microspaces that allow cells to interact with each other and grow. The system is also

designed to be simple, scalable, low-cost and commercially-viable: i) Alginate hydrogels can be quickly processed in large scales with a multi-nozzle extruder[46–52]; ii) They can be quickly dissolved with the cell-compatible EDTA solution to release the product without harming cells; iii) The tubes are mechanically and chemically stable that allow culturing cells for long term (e.g. up to a few months) and at large scales; and iv) alginates are affordable and available in large quantities, and they have been used in clinics and have no cellular toxicity.

The cell-friendly microenvironment brings enormous improvements in culture efficiency including cell viability, growth rate, yield, genetic and phenotype stability, culture consistence and scalability (scale out and up)[46–52]. For instance, hPSCs expand ~1000-fold per 9 days per passage to yield ~$5.0x10^8$ cells per milliliter of hydrogel tubes. For comparison, hPSCs typically expand less than 10-fold per passage to yield less than $5x10^6$ cells/mL in 3D suspension culture. Cells in AlgTubes have less DNA damage and phenotype changes: factors that correlate with higher product safety and potency. This method has been demonstrated for hPSCs expansion, differentiation and reprograming, as well as for expanding T cells and adult stem cells, all with extremely high efficiency[46–52].

The high yield and expansion/passage make it possible to produce clinically relevant numbers of cells (e.g., $1x10^{10}$) for each patient from small amounts of starting cells (e.g., $1x10^7$) with less than 20 mL hydrogel tubes contained in a small, disposable bioreactor (e.g. a 50-mL conical tube) without passaging[48,50]. For instance, to make personalized dopaminergic (DA) neuron progenitors[48], reprogramming factors were delivered to fibroblasts through electroporation and cells were processed into the hydrogel

tubes into a conical tube. Cells were reprogrammed for 20 days, expanded for 10 days, and differentiated into DA progenitors for 11 days in the sealed conical tube. On day 41, 0.5 mM EDTA was infused to dissolve hydrogel tubes. Few cells died during production. Cells survived well and matured into TH+ DA neurons *in vivo*. This all-in-one-tube device, if fully developed and automated, can have a significant impact on scaling out the production of autologous cells for personalized cell therapy.

The high expansion/passage and yield also have high impact on scaling up the cell production[46]. For instance, mathematical modeling shows producing $1.5x10^{14}$ hPSCs (from $2x10^{8}$ hPSC seeds) with stirred-tank bioreactors requires ~104,811 liters of total bioreactor volume, 11 passaging operations, and 48 days, which is technically and economically challenging. The same production can be done with about 320 liters of AlgTubes in 20 days and 1 passaging operation. The reductions in culture volume, time, and passaging makes the production technically and economically feasible.

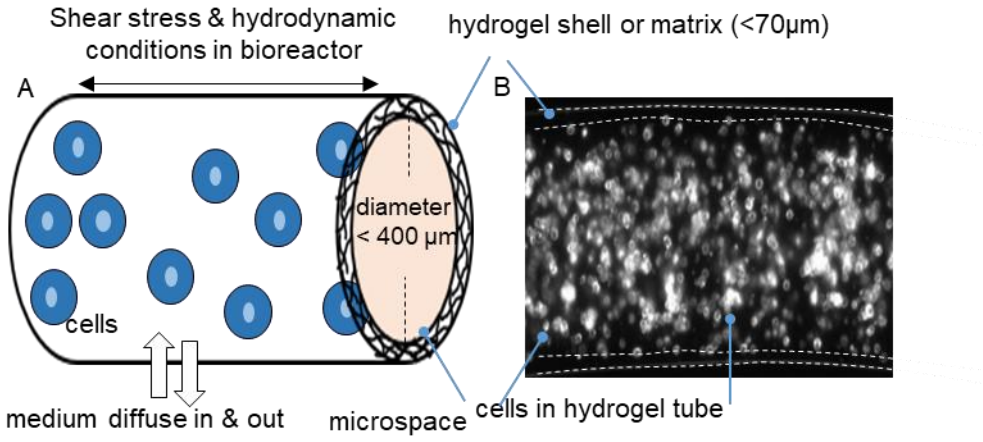

Figure 6.4. The cell-friendly microenvironment of alginate hydrogel tubes.

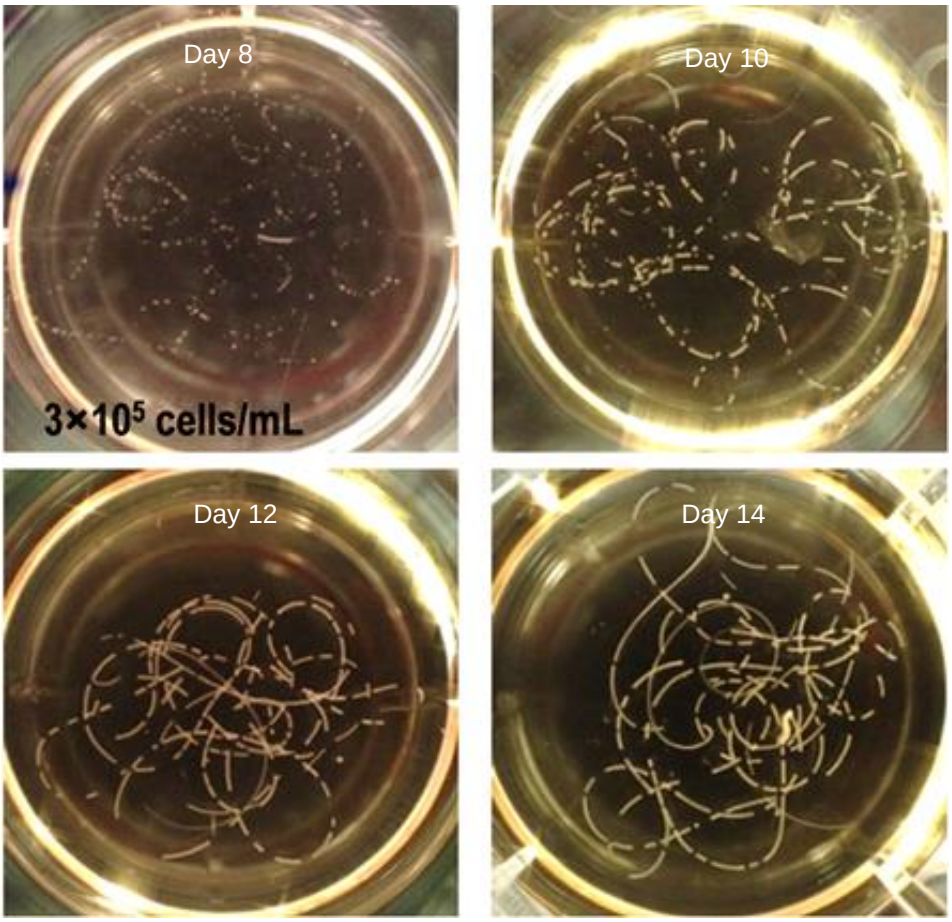

Figure 6.5. The monodispersed cell mass in one alginate hydrogel tube suspended in a 6-well plate on day 8, 10, 12 and 14. Cells were seeded as $3x10^5$ cells/mL

Summary

There is a critical need to develop efficient cell culture technologies to achieve the full potential of cellular therapeutics. Academia and industry are currently focusing on developing modular, disposable and closed bioreactors; automating the cell culture; integrating process analysis and control and artificial intelligence; and scaling out and scaling up the 3D suspension culture system[1]. These efforts are significant since they can change the current manual manufacturing to automated manufacturing. However, these efforts may not sufficient to fully address the large-scale cell culture challenge since they are not enough to create a cell-friendly microenvironment. The AlgTubes system shows improving the cellular microenvironment has enormous impact on the culture outcome. Its success indicates the academia and industry should put more efforts on creating a cell-friendly microenvironment during the cell manufacturing.

Reference

1. Achieving large-scale, cost-effective, reproducible manufacturing of high-quality cells. A Technology Roadmap to 2025. *Consortium, Natl. Cell Manuf.* (2016).

2. Denning, C. *et al.* Cardiomyocytes from human pluripotent stem cells: From laboratory curiosity to industrial biomedical platform. *Biochim. Biophys. Acta - Mol. Cell Res.* **1863,** 1728–1748 (2016).

3. Kempf, H., Andree, B. & Zweigerdt, R. Large-scale production of human pluripotent stem cell derived cardiomyocytes. *Adv. Drug Deliv. Rev.* **96,** 18–30 (2016).

4. Hartman, M. E., Dai, D. & La, M. A. Human pluripotent stem cells: prospects and challenges as a source of cardiomyocytes for in vitro modeling and cell-based cardiac repair. *Adv. Drug Deliv. Rev.* **96,** 3–17 (2016).

5. Wang, X. & Rivière, I. Clinical manufacturing of CAR T cells: Foundation of a promising therapy. *Mol. Ther. - Oncolytics* **3,** 1–7 (2016).

6. Maier, D. Challenges & opportunities for manufacturing autologous cellular therapies such as CAR-T cells. *Cell Gene Ther. Insights* **3,** 261–265 (2017).

7. Sharpe, M. & Mount, N. Genetically modified T cells in cancer therapy: opportunities and challenges. *Dis. Model. Mech.* **8,** 337–350 (2015).

8. Levine, B. Progress and challenges in the manufacturing of CAR-T cell therapy.

Cell Gene Ther. Insights **3,** 255–260 (2017).

9. Hartmann, J., Schüßler-Lenz, M., Bondanza, A. & Buchholz, C. J. Clinical development of CAR T cells—challenges and opportunities in translating innovative treatment concepts. *EMBO Mol. Med.* **9,** 1183–1197 (2017).

10. Levine, B. L., Miskin, J., Wonnacott, K. & Keir, C. Global manufacturing of CAR T cell therapy. *Mol. Ther. - Methods Clin. Dev.* **4,** 92–101 (2017).

11. Trainor, N., Pietak, A. & Smith, T. Rethinking clinical delivery of adult stem cell therapies. *Nat. Biotechnol.* **32,** 729–735 (2014).

12. Baum, E., Littman, N., Ruffin, M., Ward, S. & Aschheim, K. Key tools and technology hurdles in advancing stem-cell therapies. California Institute for Regenerative Medicine, Alliance for Regenerative Medicine Catapult, Cell Therapy. (2013).

13. National science and technology council: Advance manufacturing: a snapshot of priority technology areas across the federal government subcommittee for advanced manufacturing. (2016).

14. Lund, R. J., Närvä, E. & Lahesmaa, R. Genetic and epigenetic stability of human pluripotent stem cells. *Nat. Rev. Genet.* **13,** 732–744 (2012).

15. Peterson, S. E., Garitaonandia, I. & Loring, J. F. The tumorigenic potential of pluripotent stem cells: What can we do to minimize it? *BioEssays* **38,** S86–S95 (2016).

16. Garitaonandia, I. *et al.* Increased risk of genetic and epigenetic instability in human embryonic stem cells associated with specific culture conditions. *PLoS One* **10,** e0118307 (2015).

17. Weissbein, U., Benvenisty, N. & Ben-david, U. Genome maintenance in pluripotent stem cells. *J. Cell Biol.* **204,** 153–163 (2014).

18. Peterson, S. E. & Loring, J. F. Genomic instability in pluripotent stem cells: implications for clinical applications. *J. Biol. Chem.* **289,** 4578–4584 (2014).

19. Amps, K. *et al.* Screening ethnically diverse human embryonic stem cells identifies a chromosome 20 minimal amplicon conferring growth advantage. *Nat Biotechnol.* **29,** 1132–1144 (2011).

20. Brandwein, H., Rowley, J., Abraham, E., Campbell, A. & Oh, S. Meeting Lot-Size Challenges of Manufacturing Adherent Cells for Therapy. *Bioprocess Int.* **10,** 16–22 (2012).

21. Polak, J. M. & Mantalaris, S. Stem cells bioprocessing: an important milestone to move regenerative medicine research into the clinical arena. *Pediatr. Res.* **63,** 461–466 (2008).

22. Serra, M., Brito, C., Correia, C. & Alves, P. M. Process engineering of human pluripotent stem cells for clinical application. *Trends Biotechnol.* **30,** 350–358 (2012).

23. Lei, Y., Jeong, D., Xiao, J. & Schaffer, D. V. Developing Defined and Scalable 3D

Culture Systems for Culturing Human Pluripotent Stem Cells at High Densities. *Cell Mol Bioeng* **7,** 172–183 (2014).

24. Lei, Y. & Schaffer, D. V. A fully defined and scalable 3D culture system for human pluripotent stem cell expansion and differentiation. *Proc. Natl. Acad. Sci. U. S. A.* **110,** E5039-48 (2013).

25. Chen, K. G. *et al.* Developmental insights from early mammalian embryos and core signaling pathways that influence human pluripotent cell growth and differentiation. *Stem Cell Res.* **12,** 610–621 (2014).

26. Chen, K. G., Mallon, B. S., McKay, R. D. G. & Robey, P. G. Human pluripotent stem cell culture: considerations for maintenance, expansion, and therapeutics. *Cell Stem Cell* **14,** 13–26 (2014).

27. Kinney, M. A., Sargent, C. Y. & Mcdevitt, T. C. The multiparametric effects of hydrodynamic environments on stem cell culture. *Tissue Eng. Part B* **17,** 249–262 (2011).

28. Fridley, K. M., Kinney, M. A. & McDevitt, T. C. Hydrodynamic modulation of pluripotent stem cells. *Stem Cell Res. Ther.* **3,** 45 (2012).

29. Kropp, C., Massai, D. & Zweigerdt, R. Progress and challenges in large-scale expansion of human pluripotent stem cells. *Process Biochem.* **59,** 244–254 (2017).

30. Hajdu, Z. *et al.* Tissue spheroid fusion-based in vitro screening assays for analysis of tissue maturation. *J. Tissue Eng. Regen. Med.* **4,** 659–664 (2010).

31. Ismadi, M., Gupta, P., Fouras, A., Verma, P. & Jadhav, S. Flow characterization of a spinner flask for induced pluripotent stem cell culture application. *PLoS One* **9,** e106493 (2014).

32. Jara-avaca, M. *et al.* Controlling expansion and cardiomyogenic differentiation of human pluripotent stem cells in scalable suspension culture. *Stem cell reports* **3,** 1132–1146 (2014).

33. Chen, V. C. *et al.* Development of a scalable suspension culture for cardiac differentiation from human pluripotent stem cells. *Stem Cell Res.* **15,** 365–375 (2015).

34. Hu, W., Berdugo, C. & Chalmers, J. J. The potential of hydrodynamic damage to animal cells of industrial relevance: Current understanding. *Cytotechnology* **63,** 445–460 (2011).

35. Jossen, V., van den Bos, C., Eibl, R. & Eibl, D. Manufacturing human mesenchymal stem cells at clinical scale : process and regulatory challenges. *Appl. Microbiol. Biotechnol.* 1–14 (2018).

36. Gerlach, J. C. *et al.* Interwoven four-compartment capillary membrane technology for three-dimensional perfusion with decentralized mass exchange to scale up embryonic stem cell culture. *Cells Tissues Organs* **192,** 39–49 (2010).

37. Knöspel, F., Freyer, N., Stecklum, M., Jörg C, G. & Zeilinger, K. Periodic harvesting of embryonic stem cells from a hollow-fiber membrane based four-

compartment bioreactor. *Biotechnol. Prog.* **32,** 141–151 (2016).

38. Roberts, I. *et al.* Scale-up of human embryonic stem cell culture using a hollow fibre bioreactor. *Biotechnol. Lett.* **34,** 2307–2315 (2012).

39. Serra, M. *et al.* Microencapsulation technology: a powerful tool for integrating expansion and cryopreservation of human embryonic stem cells. *PLoS One* **6,** e23212 (2011).

40. Chayosumrit, M., Tuch, B. & Sidhu, K. Alginate microcapsule for propagation and directed differentiation of hESCs to definitive endoderm. *Biomaterials* **31,** 505–514 (2010).

41. Stenberg, J. *et al.* Sustained embryoid body formation and culture in a non-laborious three dimensional culture system for human embryonic stem cells. *Cytotechnology* **63,** 227–237 (2011).

42. Gerecht, S. *et al.* Hyaluronic acid hydrogel for controlled self-renewal and differentiation of human embryonic stem cells. *Proc. Natl. Acad. Sci. U. S. A.* **104,** 11298–11303 (2007).

43. Lin, H., Li, Q. & Lei, Y. Three-dimensional tissues using human pluripotent stem cell spheroids as biofabrication building blocks. *Biofabrication* **9,** 025007 (2017).

44. Lin, H., Li, Q. & Lei, Y. An Integrated Miniature Bioprocessing for Personalized Human Induced Pluripotent Stem Cell Expansion and Differentiation into Neural Stem Cells. *Sci. Rep.* **7,** 40191 (2017).

45. Li, Q. *et al.* Scalable production of glioblastoma tumor-initiating cells in 3 dimension thermoreversible hydrogels. *Sci. Rep.* **6,** 31915 (2016).

46. Li, Q. *et al.* Scalable and physiologically relevant microenvironments for human pluripotent stem cell expansion and differentiation. *Biofabrication* **10,** 025006 (2018).

47. Lin, H. *et al.* Hydrogel-Based Bioprocess for Scalable Manufacturing of Human Pluripotent Stem Cell-Derived Neural Stem Cells. *ACS Appl. Mater. Interfaces* **10,** 29238–29250 (2018).

48. Lin, H. *et al.* Integrated generation of induced pluripotent stem cells in a low-cost device. *Biomaterials* **189,** 23–36 (2019).

49. Li, Q. *et al.* Scalable culturing of primary human glioblastoma tumor-initiating cells with a cell-friendly culture system. *Sci. Rep.* **8,** 3531 (2018).

50. Lin, H. *et al.* Automated expansion of primary human T cells in scalable and cell-friendly hydrogel microtubes for adoptive immunotherapy. *Adv. Healthc. Mater.* e1701297 (2018).

51. Lin, H. *et al.* Manufacturing human pluripotent stem cell derived endothelial cells in scalable and cell-friendly microenvironments. *Biomater. Sci.* 373–388 (2019).

52. Lin, H. *et al.* Engineered Microenvironment for Manufacturing Human Pluripotent Stem Cell-Derived Vascular Smooth Muscle Cells. *Stem Cell Reports* **12,** (2019).